COUPLED VERTICAL AND HORIZONTAL RESISTANCE OF HULL GIRDER IN GROUNDING ACCIDENTS

by

DANIEL TROY PIPPENGER

B.S., Marine Engineering, United States Coast Guard Academy, 1986

Submitted to the Department of Ocean Engineering in Partial Fulfillment of the Requirements for the Degrees of

MASTER OF SCIENCE IN NAVAL ARCHITECTURE AND MARINE ENGINEERING

and

MASTERS OF ENGINEERING FOR THE PROGRAM IN MARINE ENVIRONMENTAL SYSTEMS

at the
Massachusetts Institute of Technology
June 1995

Signature of Author _____
Department of Ocean Engineering
May 5, 1995

Certified by _____
Tomasz Wierzbicki
Professor of Applied Mechanics, Thesis Supervisor

Accepted by _____
Professor A. Douglas Carmichael
Department Graduate Committee
Department of Ocean Engineering

[This page intentionally blank.]

COUPLED VERTICAL AND HORIZONTAL RESISTANCE OF HULL GIRDER IN GROUNDING ACCIDENTS

by

Daniel Troy Pippenger

Submitted to the Department of Ocean Engineering on May, 1995, in partial fulfillment of the requirements for the degrees of Master of Science in Naval Architecture and Marine Engineering and Masters of Engineering in the Program in Marine Environmental Systems.

Abstract

In a typical ship grounding accident, there is a resisting force developed in the hull in the longitudinal direction and a lifting (vertical) force applied to the hull. Previous studies have focused on the longitudinal cutting force associated with post-rupture deformation of plates by an obstacle (wedge) whose cutting surface is perpendicular to the plane of the ship's bottom plate. This report studies the coupling of horizontal and vertical reaction forces on a ship bottom structure during grounding accidents in the presence of a sloping grounding obstacle. In addition, the effect of longitudinal stiffeners on the cutting force is investigated.

Scale models of a longitudinally stiffened single hull were constructed and plate cutting experiments were conducted at two sloping angles. Theoretical models were developed that reformulate the contribution of friction in previously established analytical closed-form solutions of the initiation and steady-state phases of plate cutting by a wedge. The new formulation of friction and a geometric model were used to couple the horizontal and vertical reaction forces. Experimental results of the vertical to horizontal force ratio are within 4% and 7% of the theoretical model for the two different sloping angles tested.

The longitudinal cutting force in both the initiation and steady-state phase are shown to be insensitive to the wedge sloping angle at small to moderate wedge semi-angles. As the sloping angle decreases (measured from the horizontal), the contribution of friction increases. This is offset, however, by a reduction in membrane and bending energy so that the total force for an unstiffened plate remains relatively constant within the ranges of approximately 10° to 35° of wedge semi-angles in the initiation phase.

Global plate lift due to the sloping angle of the wedge influences both the cutting force and the vertical to horizontal force ratio. The cutting force decreases as the sloping angle is reduced due to the narrower projected wedge geometry. In contrast, the force ratio of vertical to longitudinal force increases under these same conditions.

Experimental results and data from earlier experiments show that the use of an equivalent thickness by a cross-sectional area "smearing" is inadequate to describe the additional resistance of the plate due to the addition of in the presence of a sloping angle. An empirical relationship relating the sloping angle with an equivalent thickness for this test geometry is presented.

Thesis Supervisor: Dr. Tomasz Wierzbicki

Title: Professor of Applied Mechanics

Acknowledgements

During the course of designing and conducting the experiments related to this thesis, Jocelyn Turgeon and Mohamed Yahiaoui provided me with both technical assistance and encouragement. Thank you for all of the time and effort in helping me with the experiments. Likewise, I wish to thank Professor T. Wierzbicki for his guidance during this investigation. Thanks are also due to Professor F. McClintock, Mr. A. Rudolph, and Mr. S. Rudolph for their assistance in developing the experimental apparatus. I also note with gratitude the assistance of Ms. Teresa Coates in numerous logistical issues throughout this research. Finally, the greatest appreciation is accorded to my family, especially my wife, Ellen, for their continuous encouragement throughout my course of study at MIT.

Table of Contents

List of Figures

List of Tables

1. Introduction

1.1 Background

Traditionally, ships have been designed to withstand the forces they encounter during their routine interaction with the sea. It has only been in the past four decades that significant research in the area of ship strength in collision and grounding accidents has been initiated. This research focused initially on ship collisions and was later extended to grounding accidents. The strength of ships in accidents has gained more importance in the past two decades with the advent of enormous tank vessels and the potential for catastrophic environmental damage associated with collision and grounding.

Large oil spills have become a more pressing problem as the size of tank vessels expanded rapidly. The largest tankers in the early 1950s have grown over 20 times this size by the mid 1970s to more than 500,000 DWT (dead weight tons). These large ships are named very large crude carriers (VLCC). This increased carrying capacity resulted in the potential for widespread environmental effects when accidents occur. Although smaller in comparison to some other oil spills, the *Exxon Valdez* grounding accident in 1989 focused public attention on the safety of tank vessels. This spill lead to increased government regulation in the United States (through passage of the Oil Pollution Act of 1990) and a self-examination by the oil transport industry, as a result of the financial liability imposed on the owners of the *Exxon Valdez*.

This investigation into the ability of tank vessels to withstand damage in collision and grounding, termed *crashworthiness*, exposed a lack of adequate methods to accurately predict the strength of hull structures in grounding accidents. Although some research had been initiated in this area, a complete solution that would allow consideration of different ship structural arrangements did not exist. To fill this gap in knowledge, the *Joint Industry-MIT Program on Tanker Safety* was started in 1992. The goal of the project is to develop analytical models to predict the extent of damage in

grounding accidents. From this prediction, oil outflow calculations may be completed and different structural designs can be compared by their ability to limit damage. The ultimate goal of the three-year program is to provide participating industry and regulatory bodies with a computer program to assess the crashworthiness of different hull structural designs.

1.2 Grounding Model

To develop computational methods to predict damage in grounding accidents, a typical tanker grounding model was developed by Wierzbicki, Peer, and Rady (1991) as part of the *Joint Industry-MIT Program on Tanker Safety*. This model was based on information contained in ship grounding reports and observed damage. This model is described below.

Initially, when the ship interacts with the grounding obstacle (in this case assumed to be a rock), there is global lifting of the ship against the force of gravity and no initial hull rupture. As the ship continues its forward progression over the rock, the lifting force decreases and the rock increases penetration into the ship hull. Eventually, rupture occurs and further damage will follow as a result of hull fracture and plastic deformation. Damage is assumed to progress from the initial point of contact longitudinally toward the stern. The grounding sequence is characterized by four distinct stages:

Outer dynamics;
Initiation of local damage;
Development of localized damage; and
Steady-state deformation.

The three initial stages are dependent on the forces associated with global ship motion and the resultant reaction forces. Steady-state deformation occurs after hull breach and consists of the fracture and plastic deformation of the hull girder. The kinetic energy

of the ship is dissipated through fracture, plastic deformation, and friction between the hull structural members and the grounding obstacle. To determine the extents of damage to the hull girder, an energy balance approach is used. The energy-absorbing mechanisms are applied to all ship structural members that are involved in the grounding process which is equilibrated with the ship's initial kinetic energy.

In this report, only the steady-state stage of the grounding process is examined with respect to a longitudinally stiffened single hull model. This steady-state hull cutting process, is preceded by the initiation phase, which occurs after hull rupture and is the initial cutting and tearing of the hull. At some length, the action will become a steady-state process in which the deformation pattern is different from the initiation phase.

1.3 Theoretical Background and Previous Research

The initial studies of ship strength in collision accidents were undertaken by Minorsky (1959) to predict the ability of ship structures to prevent penetration of nuclear reactor spaces in ship collisions. Much of the following research in both collision and grounding stems from his work. Minorsky developed an empirical energy balance formula based on collision statistics. The kinetic energy absorbed in collision is equal to

$$E_T = 414.5 R_T + 121{,}900 \, ton \, knots^2 \qquad (1.1)$$

where R_T is a resistance factor with units of ton-knots^2. The resistance factor is determined by summing the damaged volume of material from both ships involved in the collision. Minorsky showed that this approximate relationship has a good correlation at high energy levels but is suspect in low energy collisions.

Further studies on the collision strength of ships were conducted by Akita, Ando, Fujita, and Kitamura (1972). They tested several different collision scenarios but the one of interest in this report is the cutting of a ship's bow (wedge) through a deck plate. The

tests were quasi-static and used to validate a force balance model developed by the authors. The model consisted of a wedge cutting into a plate with some force, P, which was resisted by a reaction force per unit length exerted on the face of the wedge by the plate and was equal to the yield stress, σ_Y, times the thickness of the plate, t. The final expression for the force of a rigid wedge cutting through a plate was

$$P = 2\sigma_Y t l \tan\theta \qquad (1.2)$$

where θ is the wedge semi-angle and l is the penetration length. There is no consideration of the deformation of the plate outside of the area of the wedge. This formula is important because is that it is the first attempt at an analytical solution to determining the force needed to cut a steel plate.

Vaughan (1978) further extended the Minorsky method to grounding accidents. Vaughan separated the cutting work done on a plate by a wedge into two parts: work done in tearing and the work in distortion. Based on the experiments conducted in Japan by Akita et al (1972), the empirical formula he developed was

$$W_S = 352 V_S + 126 A_S \qquad (1.3)$$

in units of ton-knots^2. V_S represents the distorted volume, which is related to the distortion work, while A_S is the term representing the tearing work and is defined as the total area of fracture or tearing. V_S is defined in m^2-mm and A_S in m-mm. Vaughan noted that this relationship can be expressed in terms of the resistance factor determined by Minorsky by assuming that $R_T = 2\ V_S$. Vaughan (1980) further developed his solution by conducting experiments to determine the work done by a rigid wedge penetrating a plate. Elastic energy was assumed to be negligible and the total energy was separated into cutting and bending energy. The empirical formula he developed was based on drop-hammer experiments of a wedge onto the edge of a steel plate. From the experiments, Vaughan proposed that the total work, W, is equal to

$$W = 5500 l t^{1.5} + 4400 t^2 A \qquad (1.4)$$

In equation (1.4), t is the thickness of the plate (in units of mm), l is the penetration distance (in m) by the wedge and A is the area of the deformed plate which is found through the wedge geometry. The deformed plate area is restricted to the surface area of the wedge that has indented the plate. The equation is in units of N-m with the first term on the right-hand side representing the cutting work and the second term, the bending work.

Woisin (1982) criticized Vaughan's omission of friction work and the curling deformation of the cut plate flaps due to wedge penetration. He cautioned against a replacement of parts of Minorsky's formula because of the assumption by Minorsky that two ships of equal strength were involved in the collision. In Vaughan's case, he was modeling a rigid wedge on a plate which is in contrast to Minorsky's earlier assumption. Woisin also conducted drop hammer tests of wedges into plates as well as a series of 13 tests where the plate and wedge were of the same material. Based on these tests, he proposed as an expression for the cutting work as

$$W = 4.8 l t^2 \quad for \;\; 2 \le t \le 10 mm \qquad (1.5)$$

where 4.8 is N/mm^2, and l and t are in units of mm. This formula is not that different from the first term on the right-hand side of equation (1.4), which is Vaughan's formula for the cutting work.

Jones and Jouri (1987) took this approach of decomposing the work into distinct elements a step further. They broke the energy required in the cutting of steel plates by a rigid wedge into four components as

$$W = W_{Cutting} + W_{Distortion} + W_{Elastic} + W_{Friction} \qquad (1.6)$$

which is identical to the approach of Vaughan (equation (1.4)) except for the addition of the work of friction. The elastic energy was assumed negligible. The cutting work was determined from drop hammer experimental observations, the bending work (which includes shear and membrane effects as well) was analytically calculated based on the after-test plate-flap curling deformation patterns observed, and the friction work was calculated by a force balance equation relating the wedge geometry, penetration length, coefficient of friction, and empirical parameters related to the cutting work. Thus, the solution was a mixture of an analytical and empirical approach. In addition to the drop hammer tests with a sharp wedge, several tests were conducted with a radius tip on the wedge. Test results indicate that although the initial force at contact was higher, the force level was similar to that of a sharp edge wedge as the penetration length increased. Jones and Jouri also stated that the distortion energy was small compared to the cutting energy and that therefore, strain rate sensitivity was not a significant concern in the calculation of total work. Finally, the investigators found that simple geometric scaling ratios of small scale tests did not extrapolate the results accurately to larger-size tests.

Up to this point, plate-cutting experiments had been conducted primarily as drop hammer type experiments with the exception being the tests conducted by Akita et al (1972). A departure from this dynamic test condition was made by Lu and Calladine (1990) who conducted wedge penetration tests on a universal machine at a constant displacement speed. Using the quasi-static condition imposed by the experimental set-up, they developed an empirical relationship for the energy absorbed as a wedge cut mild steel plate. The equation

$$W = C_{1.3}\,\sigma_Y\, l^{1.3}\, t^{1.7} \quad for \quad 5 < l/t < 150 \qquad (1.7)$$

depends on the yield stress, σ_Y, the thickness of the plate, t, the penetration length, l, and a numerical constant, $C_{1.3}$, that depends on angular parameters such as the wedge sloping

angle, α, and the wedge semi-angle, θ. The tests were conducted with narrow wedge semi-angles and small changes in the wedge sloping angle from the vertical (20° maximum). A fracture parameter did not enter the solution since no cracking was observed ahead of the wedge tip. Lu and Calladine found the total force insensitive to the wedge semi-angle within the tested range ($10° \leq \theta \leq 20°$) and dependent on the wedge sloping angle although this was not fully developed. They concluded that the cutting force increases with the penetration length because the cut plate flaps are forced to continue curling as the wedge continues to advance. Use of quasi-static testing conditions reduced the impact of secondary effects such as inertia, strain-rates, and differences between the dynamic and static coefficients of friction on the experimental measurements.

Larger scale experiments were conducted by Kuroiwa, Kawamoto, and Yuhara (1992), who studied bottom raking damage in grounding accidents. They conducted 1:3 scale model experiments of a single hull and double hull VLCC. The experimental results were compared to finite element studies of the same models and to an empirical formula. The investigators modified a Minorsky style expression for the force,

$$F = \alpha \left(\sum_i \left(\sigma_Y^i A^i \right) \right) \tag{1.8}$$

where α is an empirically determined coefficient. The yield stress and cross sectional area of each structural member is multiplied and summed over the total number of members within the breadth of the wedge. Their modified equation separated the hull plating and longitudinal stiffeners into two parts as

$$F = \alpha_P \left(\sum_i \left(\sigma_Y^i A^i \right)_P \right) + \alpha_S \left(\sum_j \left(\sigma_Y^i A^i \right)_S \right) \tag{1.9}$$

where the subscripts P and S are for the plate and stiffener. Fitting this to experimental results, the coefficients (α_P, α_S) in equation (1.9) were 0.8 and 0.3 respectively. This

represents the first attempt to separate ship structural components into individually contributing components in grounding accidents.

A fully analytic approach to solving the wedge cutting force through a steel plate was developed by Wierzbicki and Thomas (1993). Based on a kinematic model, the total work was developed from three distinct contributions: membrane, bending, and friction energy. The authors asserted that the global and local plate deformation mechanisms were linked by the bending radius of the plate flaps. The membrane and bending contributions were developed from kinematically admissible velocity and displacement fields which satisfied the boundary conditions of the problem. The combination of these two contributions was termed the plastic force and was optimized with respect to the unknown plate flap bending radius which was then removed from the solution. The contribution of friction was then developed from a two-dimensional model of the wedge and plate and added to the solution. The expression became

$$F = 1.67\sigma_o \left(\bar{\delta}_t\right)^{0.2} l^{0.4} t^{1.6} g(\theta) \tag{1.10}$$

where the function of the wedge semi-angle was

$$g(\theta) = (\cos\theta)^{-0.8}\left[(\tan\theta)^{0.4} + \frac{\mu}{(\tan\theta)^{0.6}}\right] \tag{1.11}$$

The parameters are as previously defined with the addition of $\bar{\delta}_t$, which is the dimensionless crack opening displacement (COD) parameter, σ_o, which is the flow stress of the material and the coefficient of friction, μ. They found that the solution had a weak dependence on both the COD parameter and on the magnitude of the wedge semi-angle. The analytical solution compared well with the experiments by Lu and Calladine (1990) as well as subsequent tests by Maxwell (1993). The relative proportion of work dissipated by the three mechanisms could be shown for fixed $\bar{\delta}_t$, μ, and θ as

Bending - 24 %

Membrane - 36 %

Friction - 40 %

This solution is valid in the initiation phase when plate tearing or cutting is occurring at the wedge tip and plate bending occurs along inclined moving hinge lines. The rolling radius of the flaps is not necessarily constant.

An analytical solution to the steady-state cutting phase was developed by Zheng and Wierzbicki (1995). In the steady-state cutting, there is significant membrane tension and compression in the area near the wedge shoulder, which was defined as a transition region. In contrast to the initiation phase, the cut plate-flaps do not continue to roll after the wedge shoulder has passed. The rolled flaps are realigned from a position parallel to the wedge face to one that is in line with the direction of wedge motion. In this case, the non-dimensional longitudinal cutting force is

$$\frac{F}{2Bt\sigma_o} = \frac{t}{4\sqrt{6}B}\left[2\frac{B+R}{R} + 1.27\frac{R}{t} + 1.28\theta^2\left(\frac{\cos\frac{\theta}{2}}{\cos\theta}\right)\frac{(R+B)^2}{Rt}\right](1+\mu\cot\theta) \quad (1.12)$$

where R, the flap rolling radius, has been minimized analytically and its solution is known as a function of the wedge geometry and plate thickness.

Paik (1994) conducted experiments to test the formulas of Lu and Calladine and Wierzbicki and Thomas in the presence of longitudinal stiffeners. The tests were conducted on a universal test machine with a sharp tip wedge and varying wedge geometric parameters. From these experiments, Paik suggested the formula

$$F = 1.5 C_{1.5} \sigma_o t_{eq}^{1.5} l^{0.5} / \cos\alpha . \qquad (1.13)$$

where α is the aspect angle of the plate to the vertical and $C_{1.5}$ is a variable dependent on the wedge semi-angle. The thickness, t_{eq}, is obtained by smearing the areas of the stiffened structure into an equivalent plate thickness. Paik observed that the wedge shoulder width and stiffener spacing influence the expected forces and that the equivalent thickness method provides a reasonable solution to account for the increased resistance to cutting that a stiffened section provides.

Some comments are necessary on this research regarding how to determine the energy dissipated in grounding accidents. The previous research has focused primarily on a wedge-cutting a plate or stiffened plate. The cutting edge of the wedge was at or close to right angles to the plane of the plate. This is not representative of actual grounding scenarios. When a ship hits an underwater rock, it is plausible to assume that the rock has some sloping angle to it. The effects of this sloping angle have not been fully considered. The only consideration has been by Lu and Calladine in their experimental observations and by Paik, who divided the force equations by the cosine of that angle to modify the magnitude of cutting force to account for the effect of the sloping angle.

Coupled with this lack of information about the effect of a wedge-sloping angle is the inattention to a reaction force orthogonal to the plane of the plate. When a ship grounds, there is a reaction force in the vertical direction that tends to lift the ship. Although this force could be small in comparison to the dead weight of the vessel, it could produce a significant lift of a ship. This vertical motion is thus coupled with the longitudinal force to form the total resistance of the hull girder in grounding accidents.

Finally, to account for the increased stiffness of a plate-stiffener section, the area of the stiffener has been spread out over the plate width to model a uniform thickness plate. This has been relatively acceptable for wedges with no sloping angle. The effectiveness of this technique has not been validated for varying wedge sloping angles.

1.4 Goal of Present Research

As part of the *Joint Industry-MIT Program on Tanker Safety*, this research continues the investigation and development of analytical solutions to grounding accident damage predictions. The focus of this research is on longitudinally stiffened single hull models interacting with an obstacle with a sloping angle. To investigate this effect, experiments were designed and conducted. Theoretical results were also developed and compared to the experimental results in an effort to:

(1) determine the relationship between longitudinal and vertical reaction force components experienced by the hull girder;

(2) quantify the effect of the sloping angle on existing theoretical solutions and provide a method of introducing this effect into the solutions;

(3) investigate various techniques for quantifying the added resistance of a plate in the grounding scenario when longitudinal stiffeners are added and the sloping angle of the obstacle is varied.

Chapter 2 contains the design and geometry of the experimental models and test apparatus. Experimental results are presented in Chapter 3. In Chapter 4, theoretical models are developed with respect to the three goals listed above. At the conclusion of the chapter, the theoretical models are compared to the experimental results. Conclusions and recommendations for future research are contained in Chapter 5.

2. Experimental Models and Testing Apparatus

This chapter describes the considerations, design, and fabrication of the experiment specimens and testing apparatus. Although previous experiments of a similar nature have been conducted at MIT as part of the *Joint MIT-Industry Program on Tanker Safety*, the attempt to measure out-of-plane forces imposed new design requirements. The nomenclature and model scaling used in earlier tests was followed as closely as possible for continuity and comparison. Only single hull specimens were considered for the new experiments for simplicity and because of the load capacity of the equipment. The ability of the Instron universal testing machine to withstand the magnitude of the in-plane forces if double hull models were used was questionable. Additionally, use of two double hull models (for symmetry) would have required design and construction of a new test frame.

2.1 Scale Model Development

Scale model geometry was determined from experiments performed by Yahiaoui et al (1994). As in that report, the constraints of the test apparatus influenced the principal dimensions of the specimens.

Specimen Design The single hull model was based on a midship section of a 140,000 DWT VLCC (very large crude carrier) provided to Yahiaoui et al (1994) by a visiting Professor, F. Fernandez-Gonzalez, to MIT in 1993. This base ship had a length between perpendiculars (LBP) of 269.0 m and a 43.2 m beam. A detailed discussion of the scaling considerations and specimen dimensions is provided by Yahiaoui et al (1994). The only additional structural members modeled in this investigation were longitudinal T-stiffeners. The bottom boundary conditions imposed by the test frame is assumed to act as transverse member. The side clamping simulates the larger longitudinal members of the ship and its resistance to global deformation due to the overall strength and size. Initially, scaling was attempted by obtaining similar moments of inertia for the plate and

stiffener combination. Different geometric arrangements, however, may have the same moment of inertia. Various geometric arrangements influence the rigidity of the plate in different manners. In light of this, physical dimension ratios of the flange, web, and plate from the base ship were used instead. Figure 2.1 provides a schematic of a T-stiffener and plate section geometry as a guide to nomenclature. The principal model VLCC parameters considered are outlined in Table 2.1.

Table 2.1 VLCC Prototype Stiffener and Plate Dimensions

Plate:	t_p = 18 mm (0.71")
	b = 850 mm (33.46")
Web:	t_w = 11 mm (0.43")
	b_w = 525 mm (20.67")
Flange:	t_f = 30 mm (1.18")
	b_f = 180 mm (7.09")

Using available plates at the laboratory, the scaling ratios of the stiffener flange-to-web thickness, plate-to-web thickness, and plate-to-flange thickness were fit as closely as possible. The scaling ratio and their relative error to the base model (the 140,000 DWT VLCC) are provided in Table 2.2.

Table 2.2 Geometric Ratios for VLCC and Model Stiffener and Plate Dimensions

VLCC Prototype	Scale Model	Relative Error
t_f/t_w = 2.73	t_f/t_w = 2.44	10.6 %
t_p/t_w = 1.64	t_p/t_w = 1.51	7.9 %
t_p/t_f = 0.6	t_p/t_f = 0.62	3.3 %

Using these ratios, the single-hull longitudinally-stiffened model geometry is provided in Table 2.3.

Table 2.3 Scale Model Stiffener and Plate Dimensions

Plate:	t_p = 1.130 mm (0.044")
	b = 53.36 mm (2.1")
Web:	t_w = 0.749 mm (0.030")
	b_w = 35.75 mm (1.41")
Flange:	t_f = 1.829 mm (0.072")
	b_f = 10.97 mm (0.442")

The specimens were constructed with four longitudinal stiffeners placed symmetrically about the centerline of the plate. The length of the stiffeners was set to ensure contact with the lower edge of the test frame. Drawings of the specimens are provided as Figure 2.2.

Specimen Fabrication Joining the such small steel members by conventional welding would be difficult and result in larger than scale welds and significant distortion to the specimen. Yahiaoui et al (1994) suggested the use of electron beam welding (EBW) for the specimens. Electron beam welding allowed small weld lines and minimal distortion to the models. However, due to its high strength, it is not representative of a scale weld. Use of EBW precludes consideration of weld strength as a parameter in the deformation of the models. Since the weld behavior was not of interest in this study, EBW was used to join the parts of the specimen. The plates, flanges, and webs were cut and machined from mild steel plate of varying thickness at the Civil Engineering Machine Ship at MIT. *Applied Energy Company* of Winchester, MA, performed all specimen joining work.

2.2 Experimental Apparatus Design

Design of the experimental apparatus was an iterative process governed largely by two factors: the use of existing test equipment and the desire for compatibility of components within two types of experiments. The second experiment was an investigation of the deformation of transversely stiffened plates without fracture described by Pippenger, Turgeon, and Yahiaoui (1995). For convenience and to conserve resources, the same style of force sensor was used in the two types of experiments. The number of transducers, however, was left particular to each experimental design.

2.2.1 Transducer Selection

As in previous plate cutting experiments at MIT, the forces in-plane of the longitudinal motion would be measured by the 20,000 lb capacity load cell that is installed in the Instron testing machine. Selection of an appropriate force transducer to measure the out-of-plane forces was the first step in the apparatus design. Due to the narrow space between test plates, the height of the load cell was strictly limited. The total width available between plates was approximately 1.5". This space had to include a portion of the wedge cutting surface (to ensure full contact on the plate) and any holding mechanism for the load cells. Preliminary calculations were completed based on similar tests on a longitudinally-stiffened single-hull model performed by Bracco (1994) to estimate the maximum forces developed at different wedge sloping angles. A coefficient of friction of 0.3 was assumed. These supporting calculations are included in Appendix A.

Based on the geometric limitations and force capacity requirements, a prospective load cell was identified early in the design process. The preliminary design included one load cell mounted between two wedges. After completing the initial design, the possibility of spot loading on the load cell due to rotation of the wedges was considered. The concern of wedge rotation and off-center loading on the load cell was the principal factor in designing the

apparatus with three cells in a tripod arrangement. A short height and high capacity load cell was selected for the final design. Major characteristics of the washer-type load cell chosen are provided in Table 2.4.

Table 2.4 Load Cell Principal Characteristics

Force Capacity	15,000 lbs
Outer Diameter	23.95 mm (0.943")
Inner Diameter	11.25 mm (0.443")
Height	10.67 mm (0.420")

2.2.2 Apparatus Design and Fabrication

Earlier plate cutting experiments at MIT were conducted with two hull plate models set vertically parallel in a test frame with a small gap between them. A drawing of the test frame is included as Figure 2.3. A wedge was then driven through the plates in a downward motion and the in-plane force was measured. The wedge was a single piece that spanned both plates, cutting them at the same time. The two symmetric tests were conducted to maintain equilibrium between the two cutting surfaces. It successfully reduced or eliminated large bending moments on the rods that connected the wedge to the test machine. This was an important feature to maintain in these new experiments since the new transversely mounted load cells are susceptible to spot loading. Any large moments created on the wedge would influence the value of the force measured by the transducers.

The Naval Surface Warfare Center (NSWC) has recently completed some large scale (1:5) grounding tests (Rodd and McCampbell (1994)) under the direction of James Rodd which measured vertical and horizontal forces. To examine the relationship between these forces, Rodd recommended splitting the existing test wedges used at MIT and locating load cells between the two halves to measure the transverse forces. In this design, the previous test

frame and testing procedure could be retained, saving considerable amounts of resources. The resulting design and construction was based on this concept suggested by Rodd.

Wedge Geometry Previous plate cutting experiments in grounding studies investigated a wide array of wedge shapes. The lack of knowledge of what the typical sea rock geometry might be in grounding accidents requires that certain assumptions be made. Without them, the possibility of many different geometries would make testing an impossible task. Figure 2.4 illustrates the various rock geometry parameters in a grounding scenario.

Bracco (1994) outlined the thought process behind choosing a broad wedge semi-angle, θ, and using a radius on the cutting edge. A narrow semi-angle is not thought to be representative of the "typical" rock geometry and produces a more mechanical cutting phenomenon through the hull plate which is not representative of the damage and energy dissipation mechanisms observed in actual grounding damage. Likewise, a sharp, knife-like edge is relatively uncharacteristic of sea rocks so a radius was added to each cutting edge to capture the dynamics of the hull plate and rock interaction in grounding accidents. Additionally, the shoulder width of the wedge, B, was selected as 3" which is wider than the stiffener separation of 2.1" to ensure deformation of the two inner stiffeners on the specimen.

Finally, the angle of attack or wedge sloping angle, α, of the rock required definition. As noted in Chapter 1, most previous studies have concentrated on a wedge either perpendicular to the plate or with a large wedge sloping angle ($\alpha = 80°$). For this initial research into the effect of the wedge sloping angles, three angles were chosen. First, the limiting case of a wedge at right angles to the plane of the plate ($\alpha = 90°$) was selected. Bracco (1994) had conducted such a test and the results were available, saving the cost and time of conducting experiments at this angle. Recognizing that Professor P. T. Pedersen of the Technical University of Denmark has conducted research on the so-called "soft grounding" (i.e. a shallow sloping bottom grounding with no hull fracture) problem, two other angles of attack were chosen so that they were outside of this work. The other two

angles selected include a relatively steep angle of 70° and a 45° sloping angle. Wedge construction drawings for these two latter angles are provided as Figures 2.5 and 2.6.

Design Supporting calculations for the apparatus design are included in Appendix A. To determine the initial design parameters, a simple two dimensional model was used to predict the expected vertical and horizontal forces. The coefficient of friction was assumed to be 0.3 and the force normal to the cutting edge was obtained from experiments conducted by Bracco (1994). The force used was the maximum force observed for a single-hull, longitudinally-stiffened model using a wedge with a semi-angle of 45°, a cutting edge with a radius tip, and a wedge sloping angle of 90°. This information was also used in the transducer selection process explained in Section 2.2.1.

There were two distinct steps in the design process. The first was to consider the buckling strength of the connecting rods and their associated bending rigidity. The connecting rods had to be strong enough to resist column buckling but flexible enough to allow end displacements when small forces were applied. These deflections were needed to compress the transversely mounted load cells during the plate cutting. A second concern was the possibility of side-to-side wedge rocking due to uneven forces applied to each cutting edge and the subsequent development of bending moments. Creation of bending moments might cause spot loading on the load cells but can be controlled by careful placement of the connecting rods and load cells.

To minimize the possibility of side-to-side wedge motion, a tripod arrangement of connecting rods was selected for the top of the wedge. One rod was arranged on the inner edge while two connecting rods were set on the extreme outer edges opposite one another to provide side-to-side stability. The outer rods were available from previous experiments and were unchanged. The inner connecting rods had tight spatial restrictions. To fit them (one for each wedge half) within the 1.5" gap between the plate holding frames required a creative approach. It was clear from initial design attempts that there was not enough space between

the test frames for separate connecting rods to each wedge. To meet the strict spatial and strength requirements, a split connecting piece was designed that was a single column for the upper part of its length and then split into two separate columns in its lower section. This piece of the apparatus was termed the *forked column*. This would allow both wedges, placed in mirror image to one another, to be centrally connected by one column at the top of the test machine while maintaining independent bending flexibility to allow compression on the load cells. The designed shape ensured that minimal force was required to close the two end of the fork so that the transducer reading would be as accurate as possible. Figure 2.7 illustrates the forked column arrangement in the testing apparatus. Each fork of the bar holds a transition piece that is fastened to it by two screws. In turn, each wedge half is connected to one of the transition pieces by three screws. These transition pieces are seen on top of the wedge in Figure 2.7.

Using the physical and geometric properties of the connecting rods, the buckling strength of each rod was computed. The boundary conditions were assumed to be clamped-clamped. The small deflections at the bottom of the rods caused by load cell compression were considered insignificant to alter the boundary condition. From these calculations, the column buckling strength of each connection rod was determined to be satisfactory.

The next step in the apparatus design was to determine the expected load cell deflections and the subsequent effect on the connecting rods. Deflections were calculated by assuming the washer-style load cell acted as a thick-walled cylinder in compression. The theoretical result compared favorably with the manufacturers calculated value and was quite small. This deflection was then applied to the ends of the connecting rods to determine the amount of force required to deflect the wedge inward. This shear force cannot be avoided but should be small in comparison to the forces measured by the load cells for accurate measurements to be obtained. The myosotis method was used by applying one half of the deflection to the center of each rod length where bending moments are zero. The shear is constant for the length of the rod and may be calculated given the deflection. Computations

indicate that the shear forces generated are orders of magnitude lower than the out-of-plane forces expected during the experiment and may be neglected.

A next task was to find a way of installing the load cells between the two wedge faces. To ensure that the initial wedge cutting edge would contact the plate and not slip between the wedges, the cutting edges were extended 0.25" inward past the plane of the plate. Using a pre-cut on each specimen, it is probable that the plate would then ride outward on the wedge surface prior to tearing. The possibility of a "concertina failure mode" was not expected in this experiment and was not addressed. By extending the cutting surface inside the plane of the plate, only a 1" gap remained in which to place the load cells and their holding devices.

The cells required some small allowance for radial expansion and also needed to be held in place so that when initially set up under no load, they would not fall out. To reduce machining work and ensure compatibility between the two different wedge sloping angle experiments, two plates were designed to face one another with the load cells recessed into each body. The plates were connected on the inner face of each wedge and faced each other symmetrically. This load cell holding plate is shown in Figure 2.8. A partial through-bolt system was chosen to hold the load cells in place. A short stud is set on each plate face and extends into the load cell center cavity. The studs are designed not to contact one another. It was important to keep the studs separate so that no force transmission could occur except across the body of the load cell. Because of the wedge's narrowing near its tip, a load cell could not be placed on the expected axis of transverse cutting forces without a high risk of spot loading. To prevent moments developed by a rocking motion, three load cells were arranged in a tripod pattern. One cell is set just below the wedge tip while the others are set side by side, high enough to ensure they are fully covered by the wedge body. An isometric view of a wedge half with the holding plate and load cells attached is provided in Figure 2.9.

Finally, the prospect of off-center loading had to be considered. Based on thick-walled cylinder analysis, the load cells could not tolerate significant shifting of the load to one side of the disc without exceeding the rated load cell capacity. The tripod arrangement of the connecting rods and load cells would prevent this type of loading once the experiment was underway but initial alignment imperfections might cause off center loading. To eliminate this concern, a set of spherical seated washers was used in conjunction with each load cell to eliminate any initial misalignment. Machined flat washers were also used to ensure even contact over the three transverse load cells prior to testing.

Fabrication All machining of the experimental apparatus was conducted at the MIT Civil Engineering Machine Shop by Mr. Arthur Rudolph and Mr. Steven Rudolph. Further iterations in the design process were required once the plans were presented to the machine shop. The machinists determined the arrangement of connecting pins for the various components. Mr. Stephen Rudolph also assisted in the design of the connecting collar to attach the forked column to the test machine frame. All components were made from mild steel. The wedges were surface hardened to avoid scoring of the wedge cutting edge which might cause preferential plate travel as noted by Yahiaoui et al (1994). They were hardened to a depth of 0.03" using a cyanide bath at 1650° F. *BoMak Corporation* of Woburn, MA, completed the hardening procedure.

2.3 Instrumentation

This section details the data acquisition details of the experiments. The principal goal of the data acquisition portion of the experiment was to obtain sound data at sampling rate that was adequate to capture all of the information while avoiding susceptibility to small voltage fluctuations that may erroneously influence the data.

With the addition of three new transducers to the previous plate cutting experimental set up, the data acquisition system became significantly more complex than with the Instron

test machine alone. Consideration of excitation voltage, temperature change, signal noise, amplification, Wheatstone bridge balance, and data sampling rates became necessary. To further complicate the experimental set up, the laboratory computer suffered a fatal hard drive failure early in the fall of 1994. A replacement computer was obtained and installed in the laboratory. The data acquisition program, however, did not survive and new software and a new computer board were ordered and installed.

The transducers provide a voltage signal that may be converted to a force measurement. The Instron test machine transducer signal passes through a filter installed in the test machine. The three smaller load cells, however, lack any of these provisions. The Instron transducer was integrated with the test machine. It has a self-contained power source and the output was filtered to prevent signal noise contamination related to ambient and power related noises of the machine operation. Gain cannot be applied to the output signal within the machine. The output signal ranges from 0 to 4 V (twice the set rated capacity). Tests were performed on the Instron transducer to ensure that it is calibrated properly and that the output signal was linear up to twice the rated output. Section B.1 of Appendix B contains the specific information on these tests and operation of the Instron test machine. The Instron output signal composes the in-plane (longitudinal) force measurements.

The three transversely mounted wedge transducers are linked by shielded cables to a conditioner/amplifier which also serves as a power source. The cable shielding is not connected to the transducers. The cables are led from the wedge seats where the transducers are located to the conditioner and amplifier unit where the cable shields were grounded. The voltage supplied to these three load cells was 8V DC. The return signal from the transducers was then filtered and amplified before being taken to the data acquisition board through another set of shielded cables. Amplification strength calculations are included in Appendix A. These cables were grounded at the conditioner, not at the computer ports. Appendix B contains calibration procedures and equipment settings for the data acquisition system.

All inputs to the data acquisition board were made in a differential mode. This prevents errors due to a varying zero value between the three transducers. The unipolar mode is also used so that all inputs were positive volts. A *Lab-PC+* data acquisition board was chosen as the analog to digital converter. The board is made by *National Instruments* under the brand name of *Ni-Daq* which was installed in a 433/L *Optiplex Dell* desk top computer. The associated *Daqware* software package was used for data recording and real-time viewing of the recorded values. See Appendix B for more details on data acquisition and the associated sampling rates and resolution.

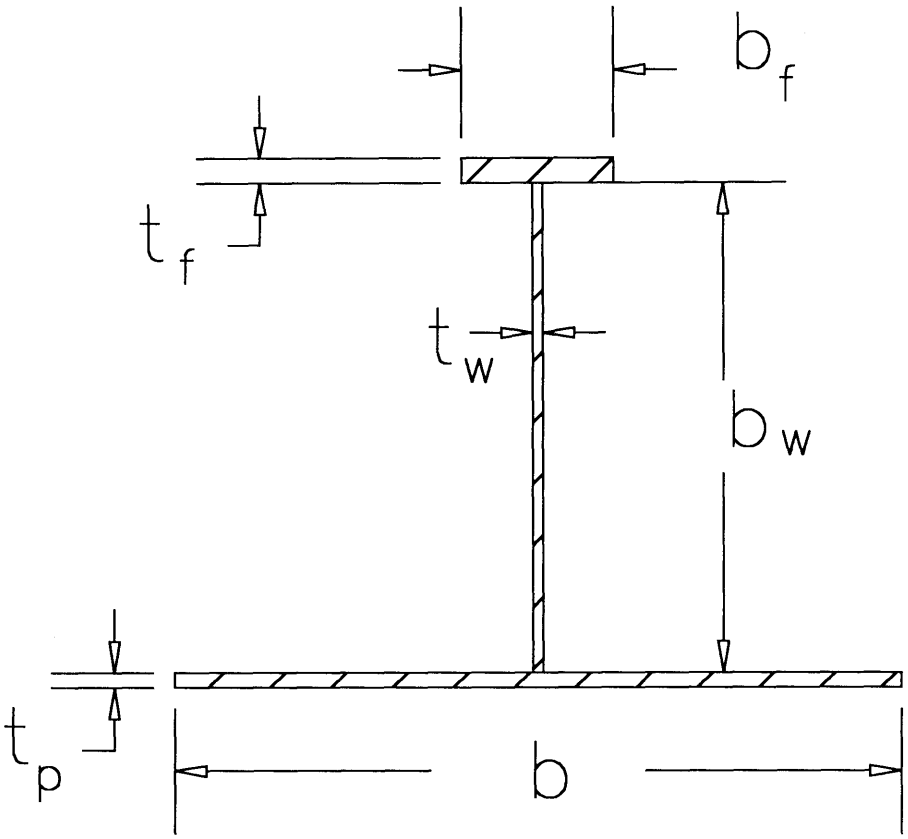

Figure 2.1 Plate Section and T-Stiffener Geometry

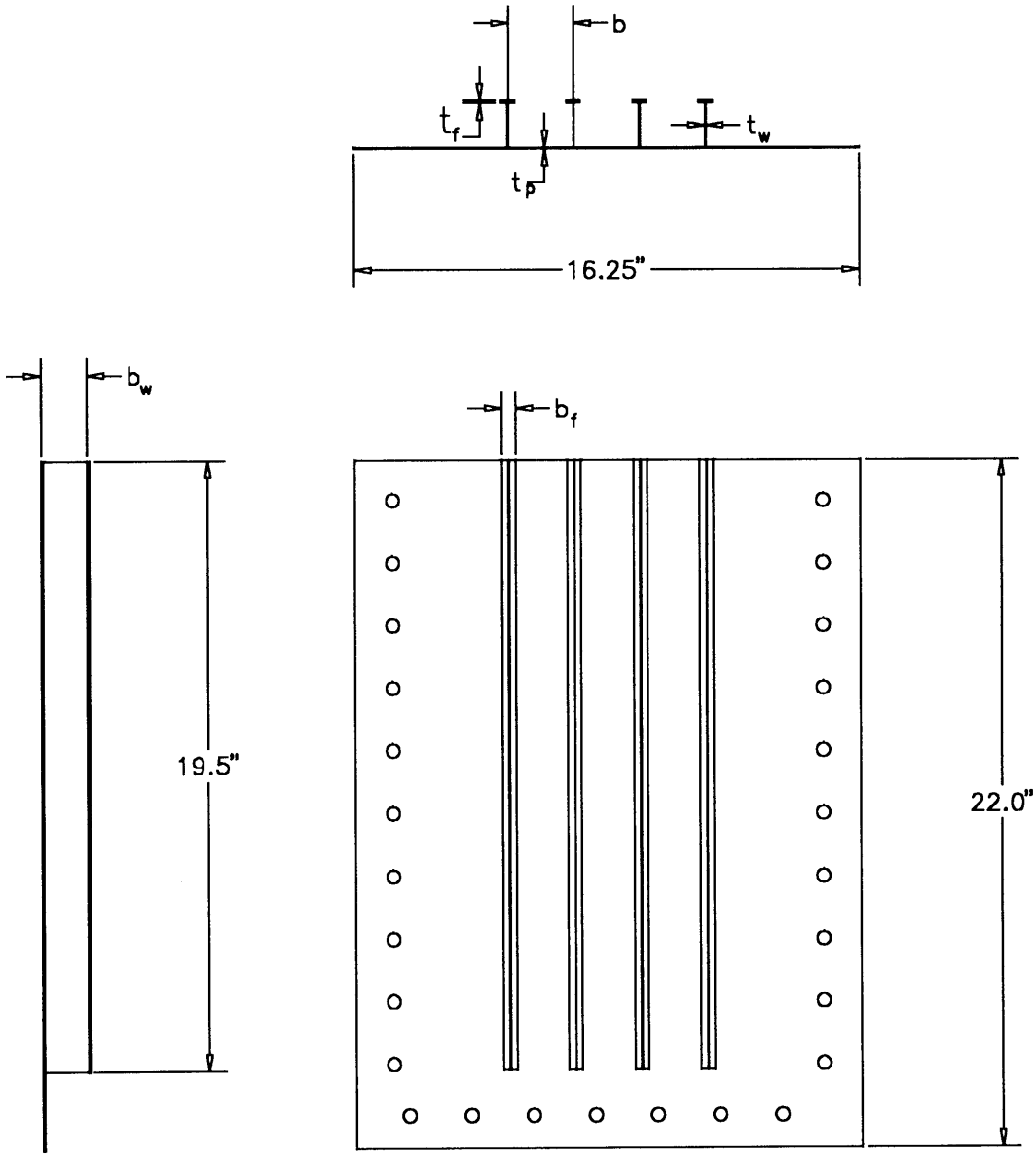

Figure 2.2 Longitudinally Stiffened Single Hull Model

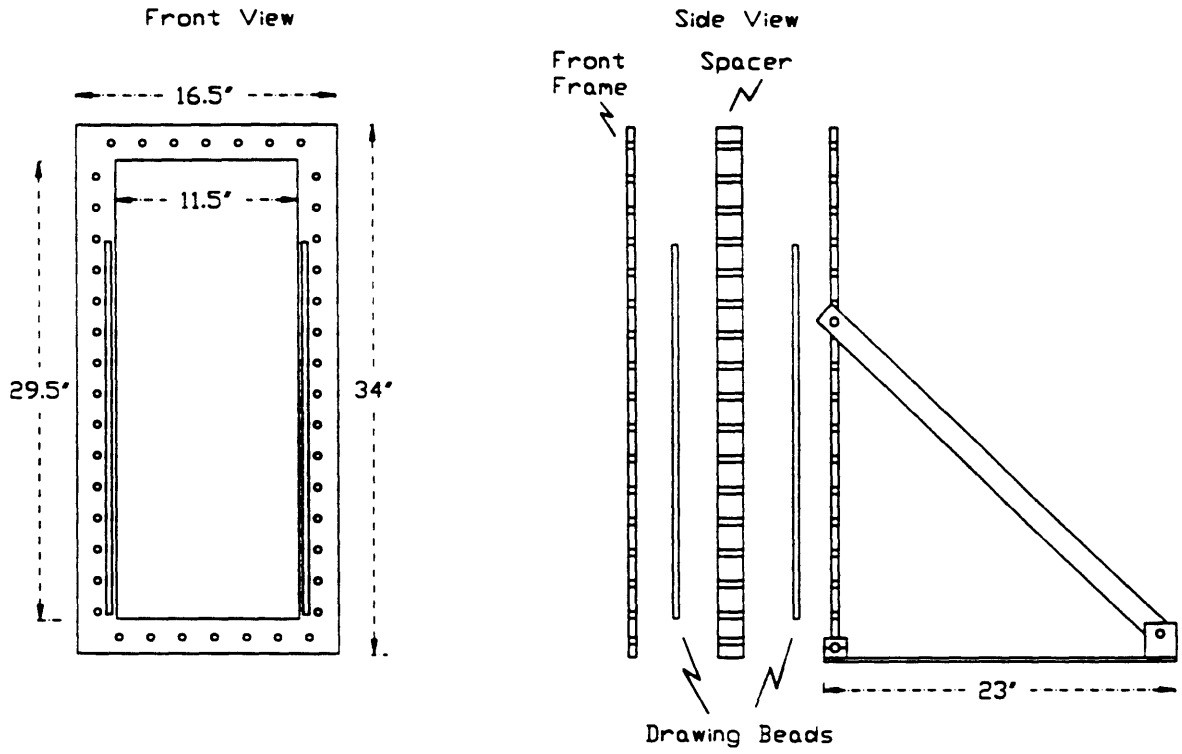

Figure 2.3 Specimen Test Frame (From Bracco (1994))

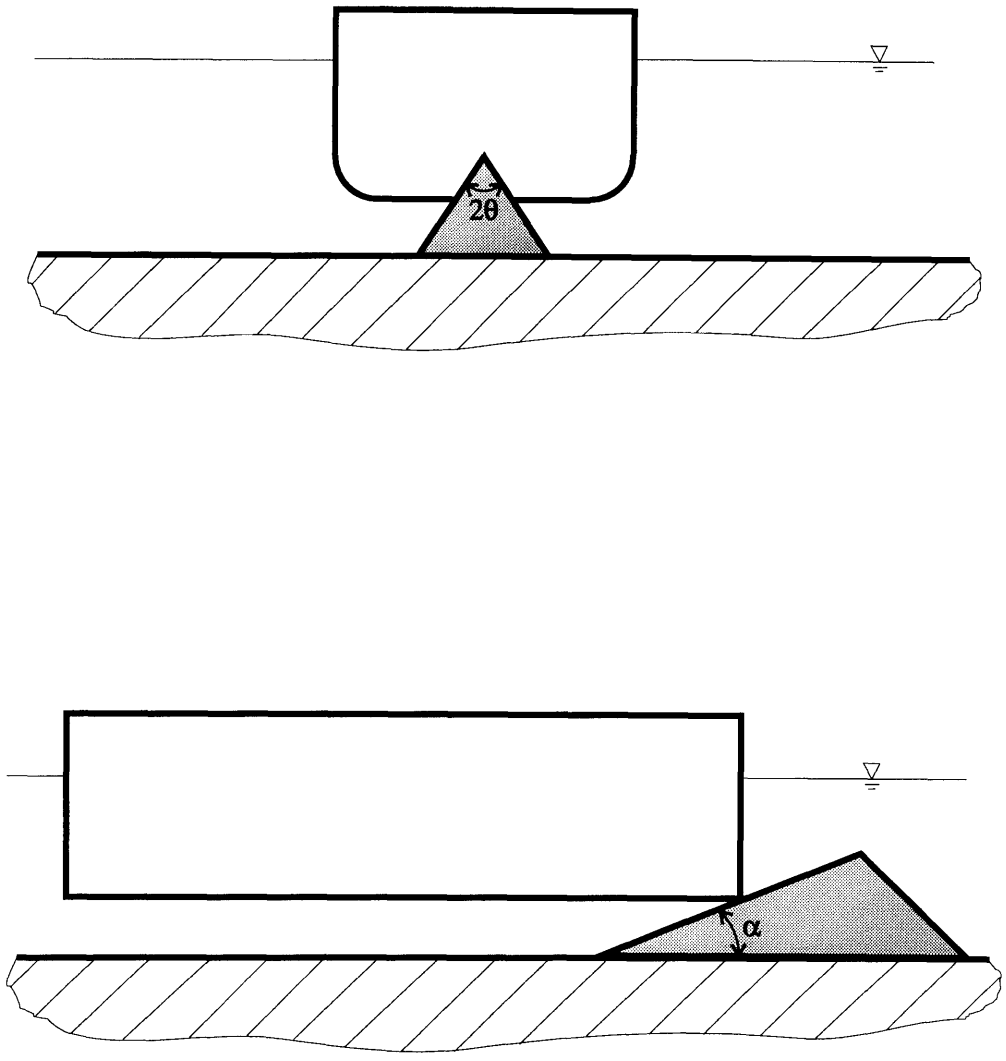

Figure 2.4 Wedge Geometry Parameters

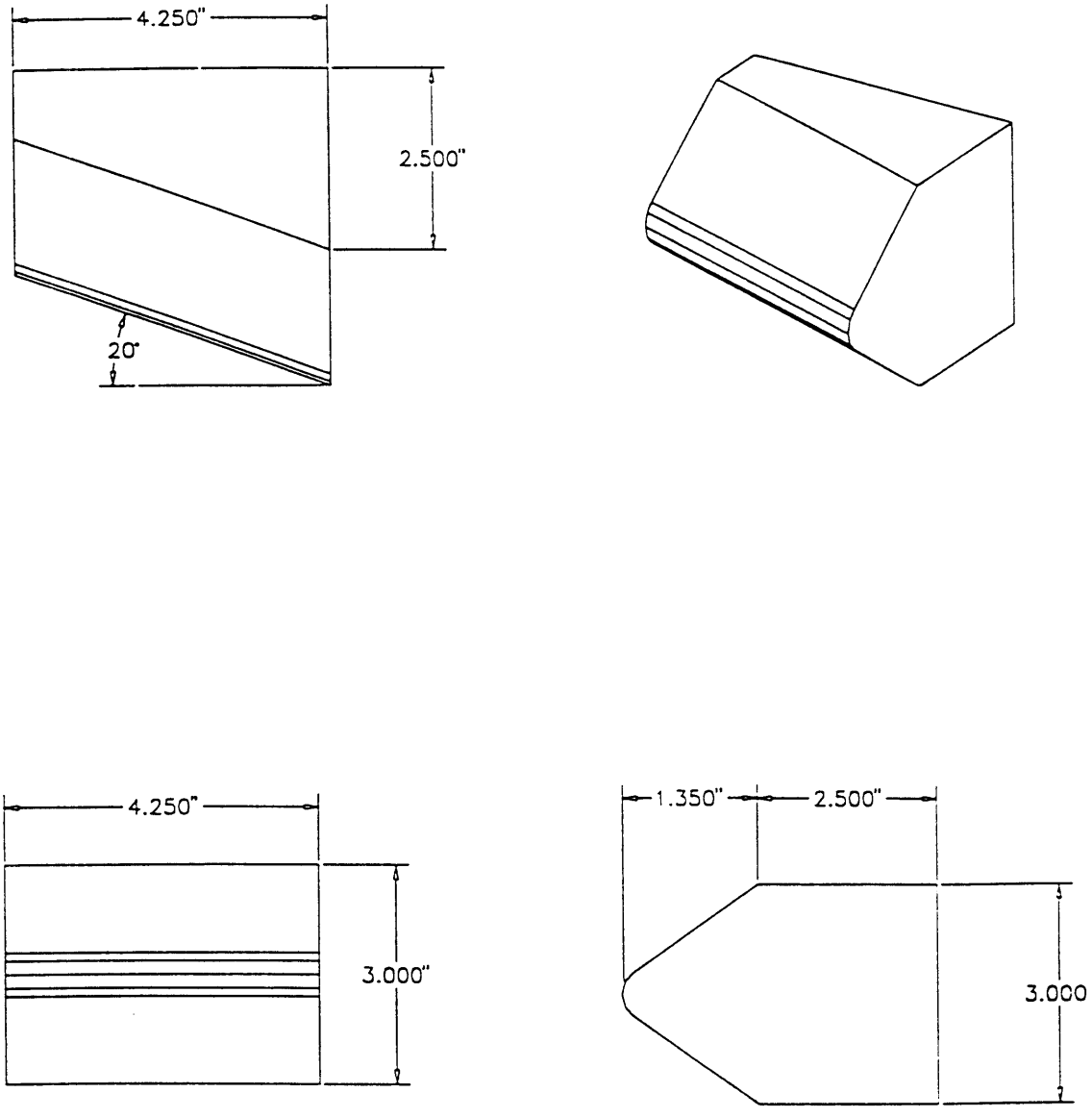

Figure 2.5 70° Wedge Geometry

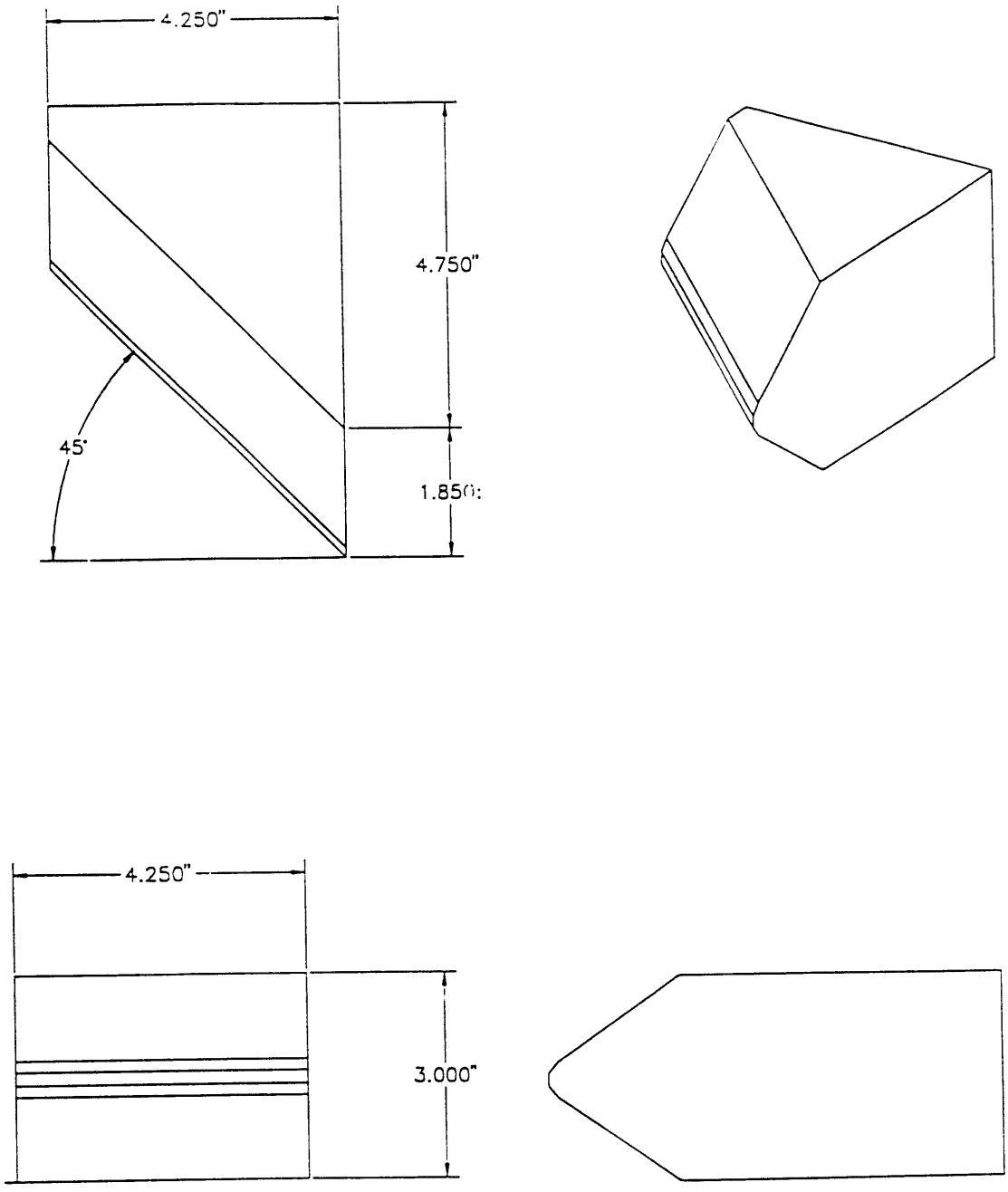

Figure 2.6 45° Wedge Geometry

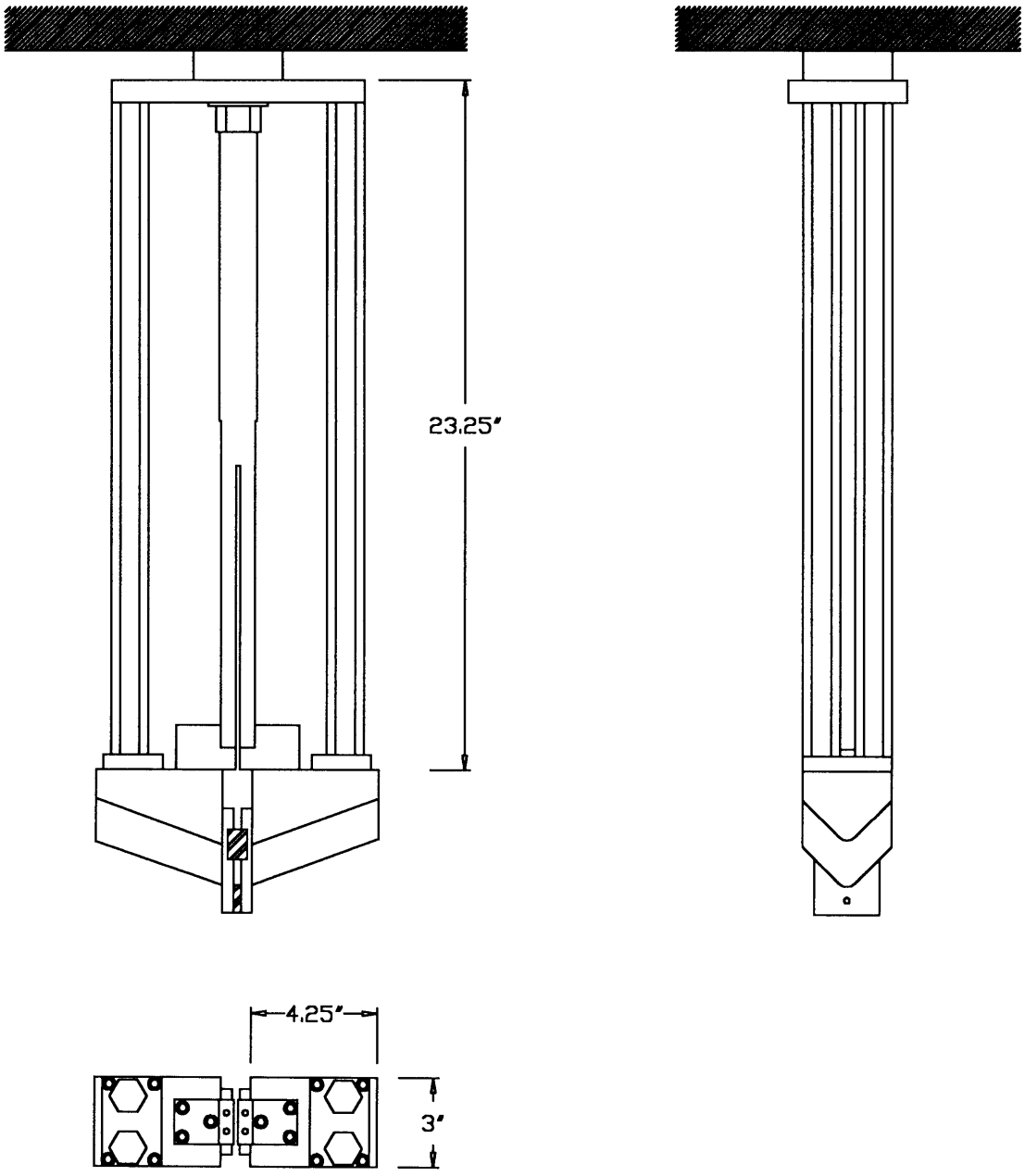

Figure 2.7 Split Angled Wedge Testing Apparatus

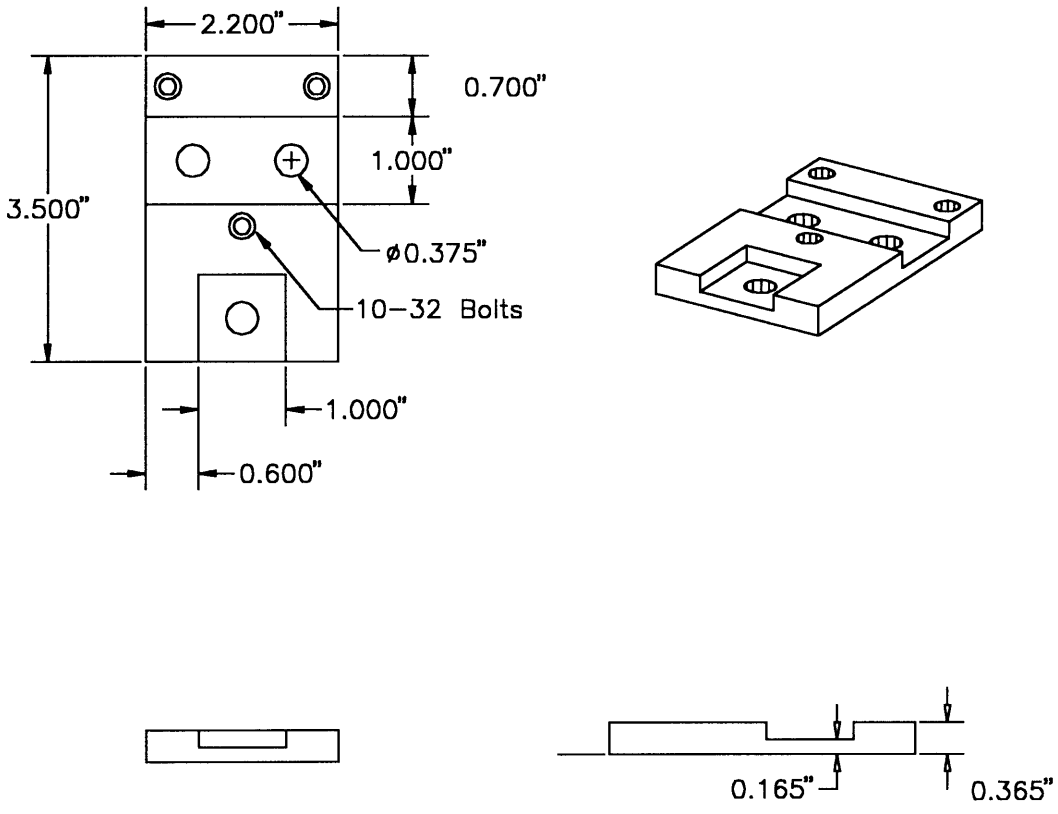

Figure 2.8 Load Cell Holding Plate Geometry

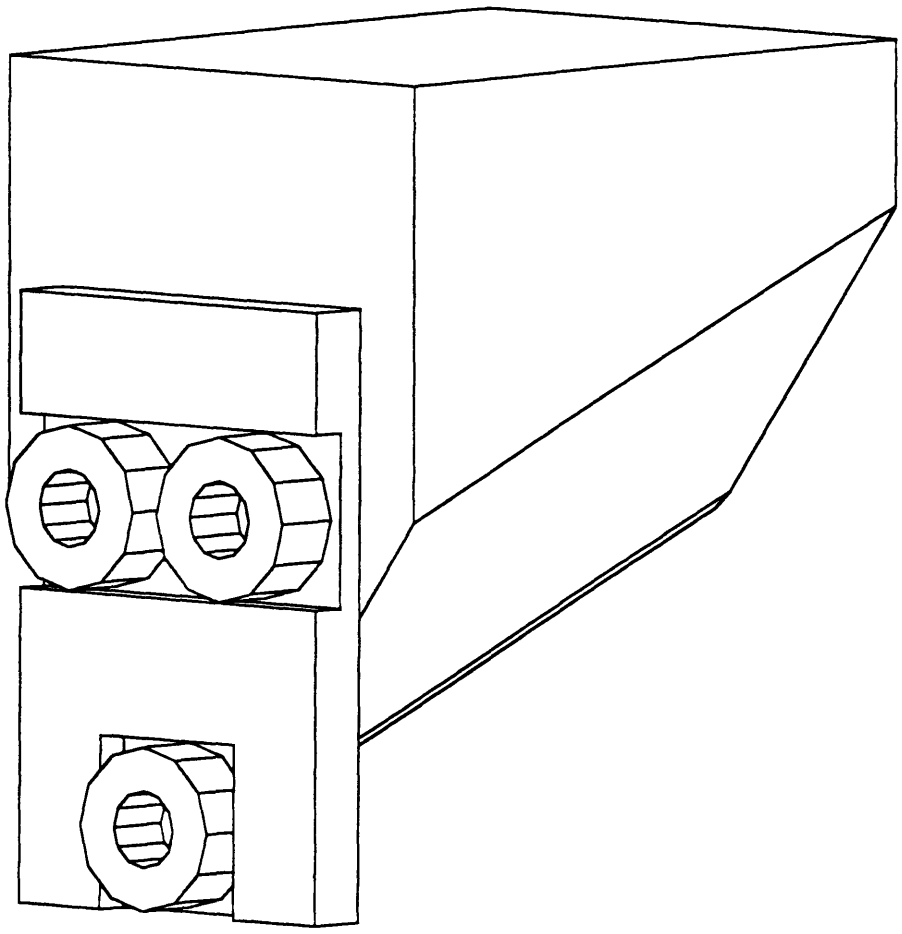

Figure 2.9 Isometric View of Wedge with Holding Plate and Load Cells

3. Experimental Results and Observations

This section describes the completion of a pilot test and experimental apparatus modifications as a result of that test. Observations and results of the subsequent experiments are then presented.

3.1 Pilot Test

A pilot test was conducted using the test apparatus as described in Chapter 2. This test was conducted with the 70° (measured from a horizontal axis) wedges and a set of longitudinally-stiffened single-hull models. Each plate had an initial pre-cut of approximately 4 cm centered transversely on the leading (top) edge of the plate. The plate to each side of the pre-cut was folded outward slightly to ensure that the plate would deform in a central cutting mode rather than a concertina tearing mode. The test was run on the Instron universal testing machine following the experimental procedures contained in Appendix B.

The pilot test exposed a problem not apparent in the initial experimental design. After a short period of plate cutting, the forces on the wedges became unbalanced. This was due to crack propagation ahead of the leading edge of the wedge. When this occurred on one specimen, the load was shifted to the opposite wedge/plate interface. This caused the test frame to rotate to one side. When the force imbalance shifted to the other side due to crack propagation, the frame rotated to the opposite side. Unfortunately, due to the narrow space between the forked column and the two specimen test frames, the forked column contacted the test frame. This caused concern for the structural integrity of the experiment and the accuracy of the measurements as further longitudinal displacement caused out-of-plane force transmission to the forked column through the test frame. Consequently, the test was started and stopped a number of times after the first 5 cm of travel in an effort to reset the frame and avoid damaging the center column. The data

taken was not useful although the load cell set-up appeared to respond well when the test frame was clear of the forked column.

To alleviate this situation, three design changes to the test apparatus were implemented. The first was a modification to the holding base of the test frames to the Instron test machine crosshead. Additional fasteners were installed with a lock-nut system to help inhibit frame motion due to unbalanced forces. Secondly, the thickness of the upper frame span where the contact occurred was reduced. This widened the gap between the frames and the forked column where the contact had occurred during the pilot test. To ensure that the strength of each frame was maintained, a doubler plate was fastened to the outer face of each of the frames across the upper span. Finally, the center column was modified to have uniform thickness on both the lower and upper sections of its length. This required the removal of some of the material in the upper length of the column. This removed the existing "lip" on the forked column that had caught on the edge of the specimen frame during the pilot test.

3.2 Experimental Results

Two experiments were conducted on the longitudinally stiffened single hull (LS-SH) models following the modifications to the test apparatus. They are summarized in Table 3.1. A third experiment, included in Table 3.1 as Test No. 1, was conducted by Bracco (1994). A photograph of Test No. 3 is shown as Figure 3.1 to illustrate the experimental arrangement. The force-cut length curves for each test are included with photographs of the specimens in Figures 3.2 - 3.4. The cut length distances are referenced from initial point of the plate and wedge contact. Since all of the plates were precut and pre-deformed (flaps folded to prevent concertina failure mode), initial contact of the wedge and plate did not occur at the top edge of the plate.

Table 3.1 Summary of Experiments

Test No.	Test Date	Wedge	Specimen	Force Curve
1	2/4/94	$\alpha = 90°$, $\theta = 45°$, r = 3/8"	LS - SH	Figure 3.2
2	1/25/95	$\alpha = 70°$, $\theta = 45°$, r = 3/8"	LS - SH	Figure 3.3
3	1/26/95	$\alpha = 45°$, $\theta = 45°$, r = 3/8"	LS - SH	Figure 3.4

Note that the force measured in-plane during the experiment was for two plates. One half of the total in-plane force is presented in Figures 3.2 - 3.4 and is assumed to be accurate for a single wedge and plate interaction. This provides an approximate measure of the magnitude of the in-plane force and its relationship to the out-of-plane force. All of the tests were conducted on the Instron test machine following the procedures and settings detailed in Appendix B. A detailed discussion of the observations of each test follows.

3.2.1 Test 1

This experiment was conducted by Bracco (1994) and is referred to in that reference as Test 8. This test used a similar wedge, supporting rod configuration, the same test frame, and types of specimens. The modifications to the test frame holding system discussed in Section 3.1 were not present. The wedge was a single unit that spanned both plate-stiffener specimens. The hardened wedge had the same semi-angle, shoulder width, and radius tip as those described in Section 2.2.2. The wedge sloping angle, α, was equal to 90° so that the wedge tip axis was orthogonal to the plane of the plate. There was no out-of-plane force measurement attempted. But because of the 90° sloping angle, the out-of-plane forces were believed to be small. The in-plane force was measured by the installed Instron load cell.

An examination of the specimen reveals minor rolling flap development as a result of plate cutting process. The longitudinal stiffeners deformed in buckling and bending modes. There is evidence of stiffener bending and re-bending as the wedge

traveled through the plate. Bracco noted some crack propagation ahead of the wedge as well as weld tearing and the folding of one plate flap in a sheared concertina mode. The outer longitudinal stiffeners are relatively undamaged with some minor twisting apparent at the upper end of the specimen. There was no global deformation of the plate and no noticeable lifting of the plate at the crack tip. In addition, the crack edges exhibited no thinning on the crack surface.

3.2.2 Test 2

This test was a repeat of the pilot test following the modifications to the test apparatus described in Section 3.1. Although the modifications to the testing apparatus minimized test frame movement, there were still three instances of contact between the forked column and the frame. They were brief in duration and did not appear to influence the output voltages from the transducers.

The initial rise of the in-plane force at approximately 3.5 cm was a result of the wedge pushing the pre-deformed flaps out of the way. Following this, the in-plane force continued to rise as the wedge shoulders made contact with the two inner longitudinal stiffeners on each plate. On the front plate, the longitudinal stiffeners bowed inward toward one another as the in-plane force continued to rise. This occurred at an average distance of 4 cm ahead of the wedge tip. This was not observed on the back plate where the stiffeners deflected outward ahead of the wedge tip. The stiffeners alongside and behind the wedge were rolled aside as the wedge progressed through the plate. The crack tip then started to propagate ahead of the leading edge of each wedge at a distance of 1 - 2 cm. The drop in force at 10 cm corresponds to the rapid advance of the crack tip on the front plate and the release of the inward buckling behavior of the inner longitudinal stiffeners observed up to that point. After this crack tip advance, the inner longitudinal stiffeners on the front plate straightened and were rolled aside as the wedge advanced, similar to the process observed on the back plate for the duration of the experiment. Crack propagation was not in a straight line on either plate. The crack wandered to one

side and then temporarily arrested. As the wedge caught up to the crack tip, the crack would again propagate ahead and to the opposite side before coming to rest. The second distinct rise in force occurred as a result of the wedge catching up to the crack tip and a repeat of the process described above. In addition, this force rise also corresponds to the impact of the inner stiffeners that had been rolled with the plate flap with the two outer stiffeners on the back plate and with the test frame on the front plate. The inner stiffeners on the front plate had rolled over the outer stiffeners to contact the plate and test frame. Once again, the unloading behavior was noted as the crack continued to run ahead of the leading edge of the wedge. This pattern was repeated again in the final force rise at the conclusion of the test.

Observation of the plate crack edges show no distinct thinning which is evidence of elastic fracture (uniaxial stress) growth. This is consistent with the observations of rapid crack propagation. The stiffeners appear twisted with some local bucking in evidence. The plate deformation area extends beyond the inner longitudinal stiffeners. The inner stiffeners, in addition to the plastic deformation noted above, rolled away from the wedge with the plate flaps developed by the wedge advance. This is in contrast to Test No. 1 where no rolling plate flaps were observed in the specimen. There was some global deformation of the plate transversely and ahead of the final wedge location. This deformation was a lifting effect on the entire plate. The angle of lift of the plate in line and ahead of the wedge tip was measured as approximately 6.4° from the plate at the bottom of the test frame.

The out-of-plane force showed a good correlation to the trend of the in-plane force throughout the test but a small comparative magnitude as shown in Figure 3.3. The rise and fall of the forces due to crack tip propagation, however, was less influential on the out-of-plane force. The out-of-plane force is approximately 20% of the in-plane force for the majority of the test. Because of the crack tip propagation, the majority of the wedge and plate contact occurred at the wedge shoulder although there also appeared to be some contact on the wedge face. Some machining due to the shoulder and plate interaction was

observed on the underside of the specimens after the test. Steady state cutting was not obtained in this test.

3.2.3 Test 3

In comparison to Test #2, this experiment was relatively unexciting in the deformation patterns and force trends observed. In this test, the plates were precut as before and then pre-deformed approximately 2 cm so the 45° wedges would fit into the limited space between the bottom of the forked column and the specimens. The central cutting failure mode was observed throughout this test. The crack tip remained less than 0.5 cm ahead of the leading edge of the wedge. Crack propagation was at the same speed of advance of the wedge and was parallel to the stiffeners, straight down the center of the specimens. There was considerably more out-of-plane deflection of the plate ahead of the wedge than the previous experiments. The force rise at about 5 cm of cut length is due to the contact of the rolled inner stiffeners with the outer stiffeners after the wedge tip has passed. At this point, the inner stiffeners had rolled with the plate flap to each side of the wedge and three of the four impacted the outer stiffeners (the fourth rolled over the outer stiffener and contacted the plate). The plate flap rolling and deformation was constrained to a narrower width compared to the 70° wedge test and did not contact the test frame. The inner stiffeners of the front plate folded plastically just ahead of the wedge at a cut length of about 15 cm. This was the only deviation from the lifting, cutting, and rolling pattern observed throughout the test.

As the wedge neared the end of the test, the inner longitudinal stiffeners exhibited rotation from the bottom of the test frame. Right at the boundary, the rotation was insignificant but it increased rapidly along the stiffener's length. It is apparent from this twisting that the cutting process was being influenced by the bottom boundary condition near the end of the test. Observation of the crack surfaces on the plate show a distinct thinning consistent with the necking (biaxial stress) phenomenon of plastic fracture. This suggests that crack growth in Test No. 3 took more force than the elastic fracture in Test

No. 2. The out-of-plane deflection of the plate was much more pronounced in this test. The angle of lift ahead of the wedge (in line with the axis of the wedge) was measured at about 13.3°. This is over twice the lift generated by the 70° wedge in Test No. 2. Transversely, the plate assumed a cambered appearance with the apex along the line of wedge travel.

Figure 3.4 shows that the out-of-plane force is of the same order of magnitude as the in-plane force. Loading and unloading trends are the same although the in-plane force rises more rapidly at the end of the test after the cut length is greater than 20 cm. Overall, the out-of-plane force is around 88% of the in-plane force for the majority of the test. Examination of the specimen did reveal some friction scoring patterns on the underside of the model but the machining by the wedge shoulder observed in Test No. 2 was not present. It is also interesting to note that the edges of the cut plate after the wedge passed have a wavy appearance. This was due to the extra length along the cut edge caused by stretching of the plate alongside the wedge. Once past the wedge, this extra length on the edge buckled into the wave pattern. Steady-state cutting was not achieved in this test either due to the limited stroke of the testing apparatus.

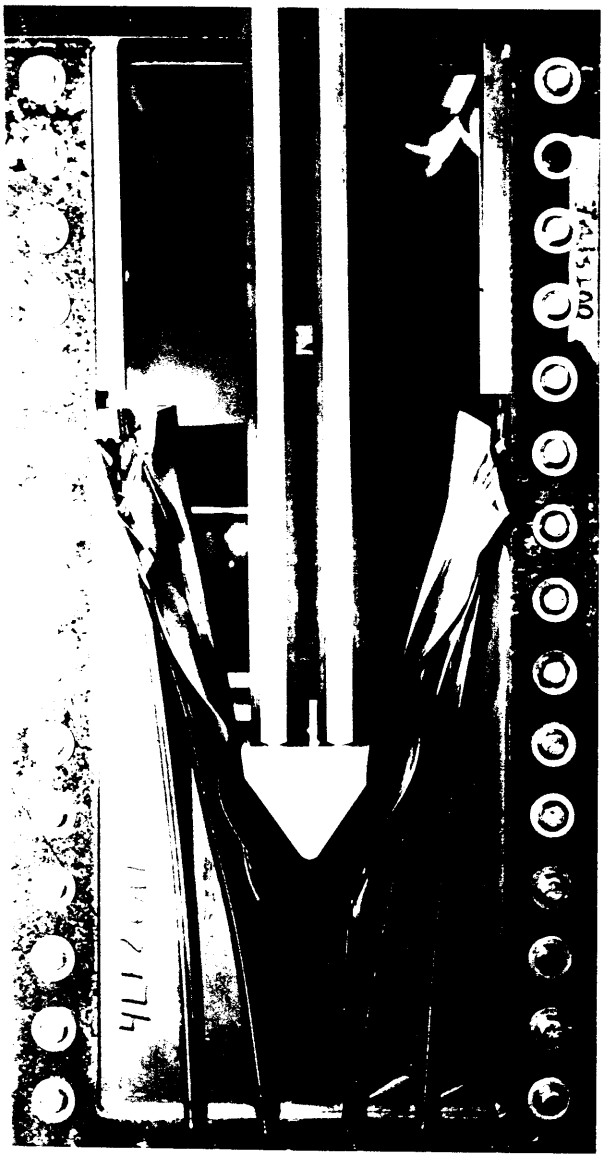

Figure 3.1 Test No. 3 in Progress ($\alpha = 45°$)

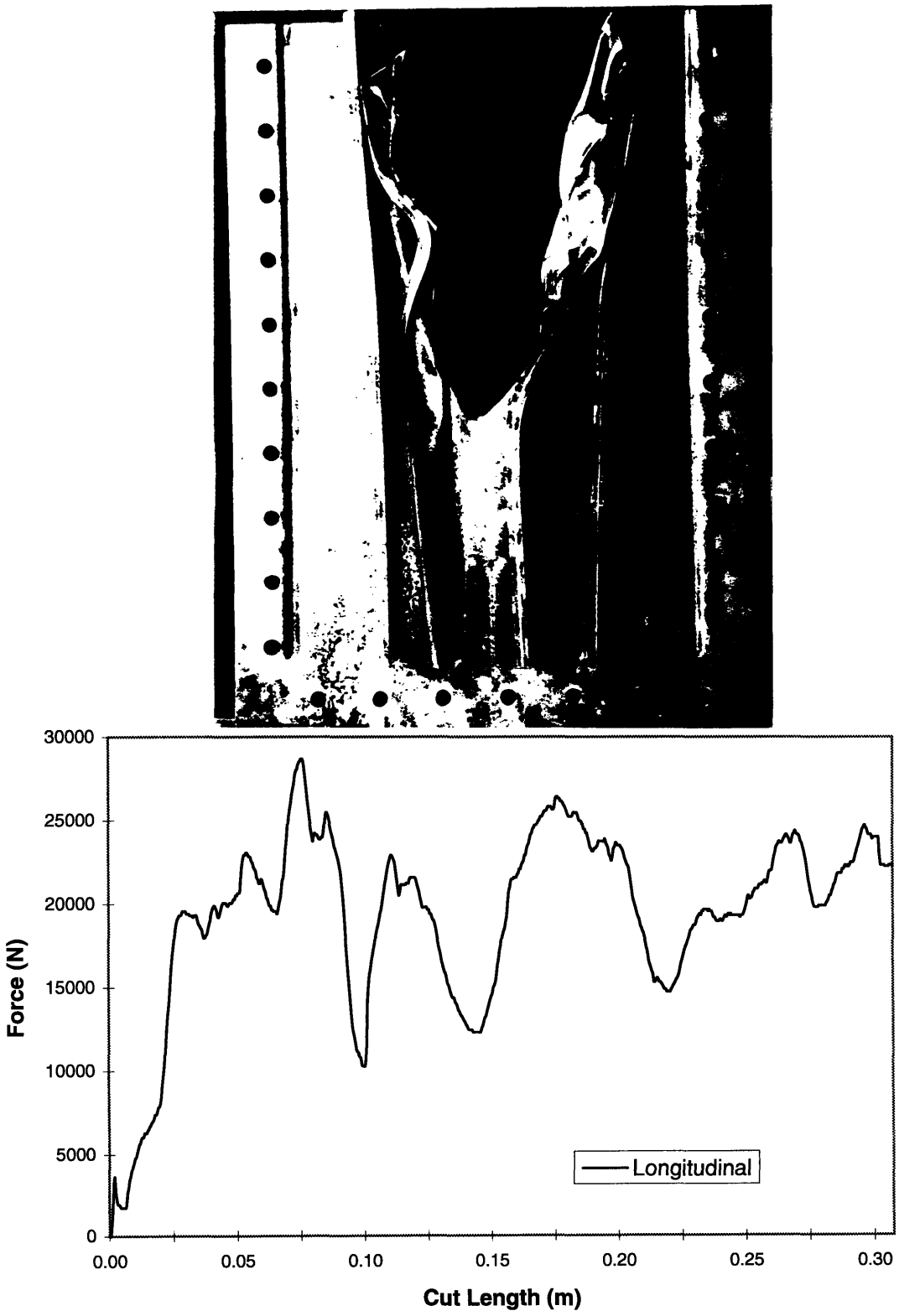

Figure 3.2 Test No. 1 (LS-SH, $\theta = 45°$, $\alpha = 90°$) - Photograph and Force-Cut Length Curve (From Bracco (1994))

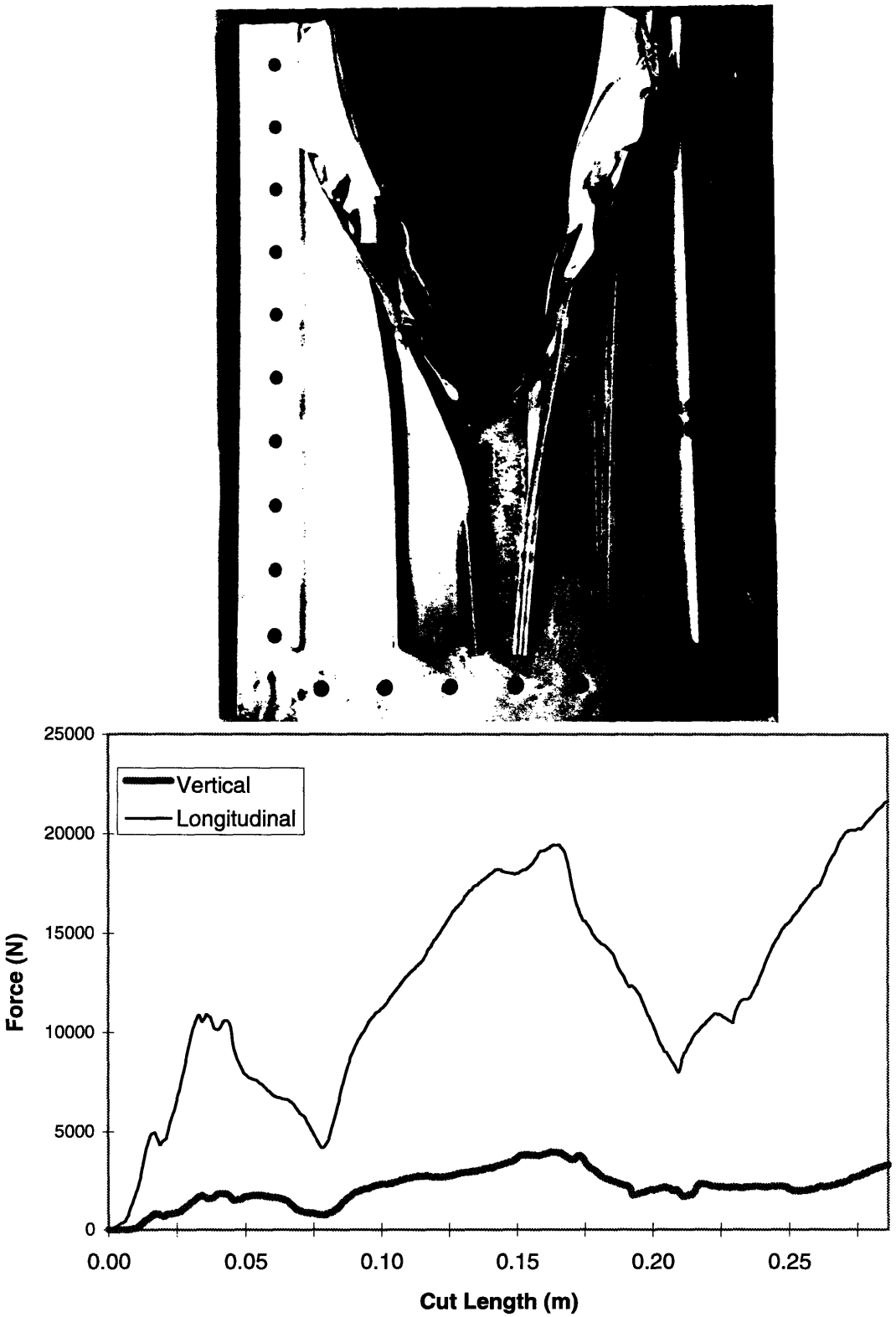

Figure 3.3 Test No. 2 (LS-SH, $\theta = 45°$, $\alpha = 70°$) - Photograph and Force-Cut Length Curve

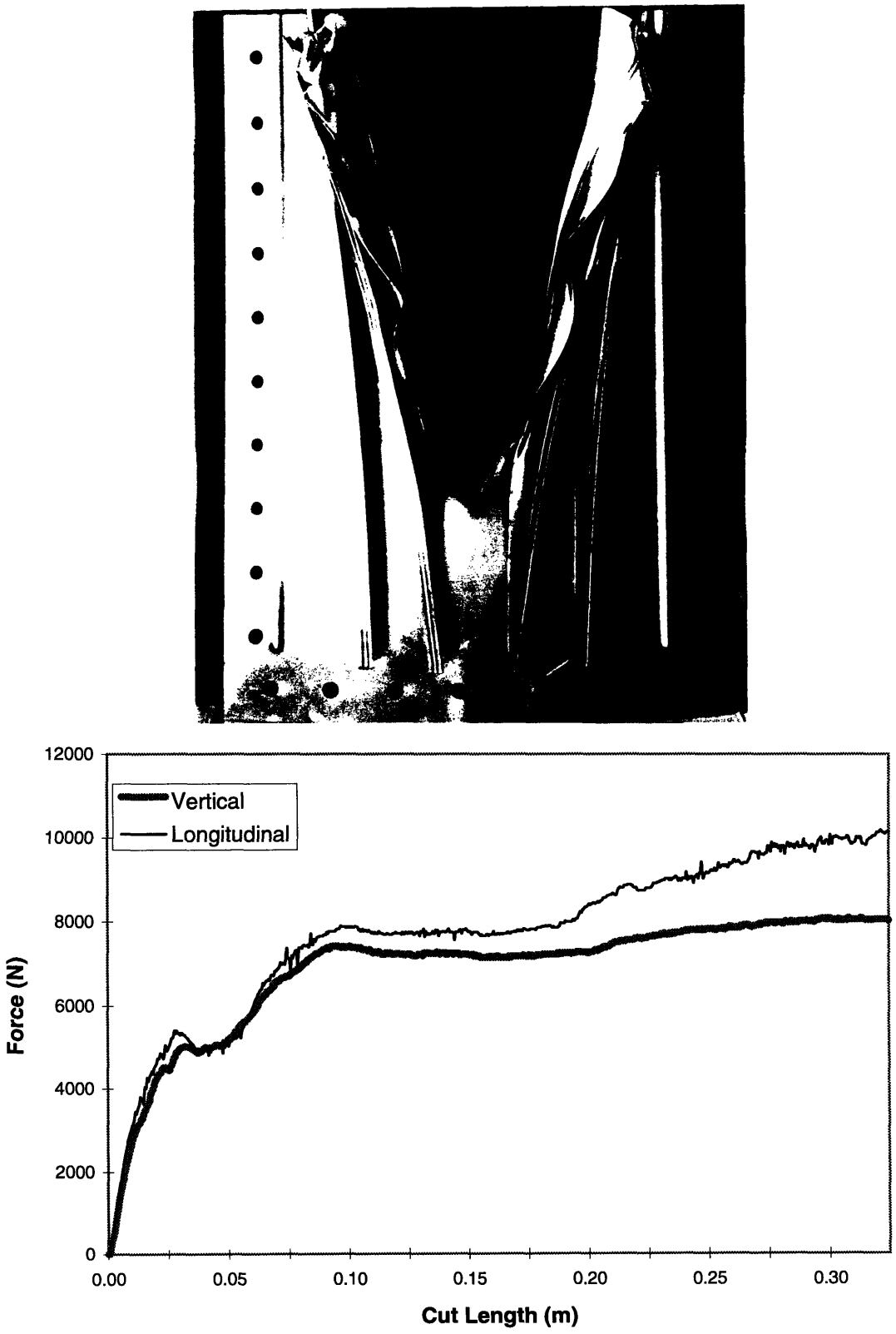

Figure 3.4 Test No. 3 (LS-SH, $\theta = 45°$, $\alpha = 45°$) - Photograph and Force-Cut Length Curve

4. Theoretical Models and Discussion

In this chapter, theoretical models are developed to determine the contribution of friction to the cutting force, the relationship between the vertical and longitudinal reaction forces, and to quantify the additional resistance to plate cutting provided by longitudinal stiffeners. At the conclusion of the theoretical development, experimental values are compared of theoretical calculations.

4.1 Contribution of Friction to Longitudinal Cutting Force

The contribution of friction has been reformulated in this study from earlier solutions by Wierzbicki and Thomas (1993) and Zheng and Wierzbicki (1995) based on consideration of the addition of a wedge sloping angle to the plate cutting problem. This is of particular interest in determining the frictional contribution to the longitudinal force by the plate bending flaps. As the wedge cuts through the plate, flaps are rolled in a cylindrical pattern along the side faces of the wedge and pushed out of the path of wedge travel. These flaps are in contact with the wedge face and cause frictional force components in the longitudinal and vertical directions.

A model of one-half of a wedge is illustrated in Figure 4.1. The sloping angle of the wedge, α, is measured from the plane of the plate which is located in the 1-3 plane. The angle, $\theta`$, is the projected wedge semi-angle, θ, due to the inclination of the wedge and is found by

$$\theta` = \tan^{-1}(\tan\theta \cos(90^0 - \alpha)) \qquad (4.1)$$

The angle β, which describes the angle between the face of the wedge and the plate on a plane perpendicular to the line of intersection of the wedge and the plate, is found by

$$\beta = \tan^{-1}\left(\frac{\tan\alpha}{\sin\theta`}\right) \tag{4.2}$$

Application of a normal and associated friction force due to plate cutting mechanics to the prism as shown in Figure 4.1 allows an examination of the forces on the wedge in a static condition. The plastic force, F_p, required to move the wedge through the plate was solved by Wierzbicki and Thomas (1993) and is composed of contributions of membrane and plate bending forces. The total force, F, in the longitudinal direction is a combination of the frictional force, F_f, and plastic force as

$$F = F_p + F_f \tag{4.3}$$

Assuming that the frictional force follows Coulomb's Law, the equation of the rate of energy balance in the longitudinal direction is

$$FV = F_p V + \mu F_n V_{REL} \tag{4.4}$$

where, V, is the velocity of wedge travel, V_{REL} is the relative velocity in the direction of the frictional force, the normal force is F_n, and μ is the coefficient of friction. (Note that the relative velocity is equal to the velocity times the cosine of the projected wedge semi-angle.) The vector decomposition of the normal and friction forces on the prism model are detailed in Appendix C. Summing the longitudinal forces after decomposition gives

$$F = F_n\left(\sin\beta\sin\theta'\right) + F_f\left(\cos\theta'\cos\zeta\right) + F_f\left(\sin\zeta\cos\beta\sin\theta'\right) \tag{4.5}$$

where ζ is the angle of relative friction contribution (see Figure C.1). Rearranging equation (4.5) to solve for the normal force and combining with equation (4.4) yields the ratio of the total longitudinal force to the plastic force as

$$\frac{F}{F_p} = \frac{1}{1 - \dfrac{\mu \cos\theta'}{\sin\beta \sin\theta' + \mu(\cos\theta' \cos\zeta + \sin\zeta \cos\beta \sin\theta')}} \qquad (4.6)$$

This ratio represents the relative contribution of the frictional force in terms of the longitudinal cutting and bending force and is different from that developed by Wierzbicki and Thomas (1993).

4.1.1 Application of the General Solution to the Initiation Phase

In the initiation phase, plate cutting occurs near the wedge tip and plate bending occurs along a moving hinge parallel to the line of intersection of the wedge face and plane of the plate. The bending flap hinge line moves with a velocity related to the relative friction velocity, V_{REL}, defined earlier. The vertical component of friction on the wedge face is due to the bending flaps contact on the side of the wedge. These flaps move up the face of the wedge at the same velocity of the hinge line travel. The speed of a material element on this hinge line in the plane of the plate and on the face of the wedge is equal to

$$V_{VER} = V \sin\theta' \qquad (4.7)$$

Whether a wedge sloping angle is present or not, the velocity of the material element is conserved and maintained in the rolling plate flap. This implies that the two components of friction are related by the projected wedge semi-angle during the initiation phase of plate cutting (regardless of a sloping angle) and that ζ is equal to the projected wedge semi-angle. Substitution of θ` for ζ in equation (4.6), yields the solution for the contribution of friction in the initiation phase of plate cutting as

$$\frac{F}{F_p} = \frac{1}{1 - \dfrac{\mu \cos\theta'}{\sin\beta \sin\theta' + \mu\left(\cos^2\theta' + \sin^2\theta' \cos\beta\right)}} \tag{4.8}$$

This general equation differs from earlier expressions for the frictional contribution to the total longitudinal force. When the sloping angle α is equal to 90°, the projected wedge semi-angle, θ', is the same as the wedge semi-angle, θ , and the angle β becomes equal to 90°. This is the case investigated by Wierzbicki and Thomas (1993) of a wedge with no sloping angle cutting through thin steel plate. The contribution of friction in this condition was derived as

$$\frac{F}{F_p} = 1 + \mu \cot\theta' \tag{4.9}$$

Substituting the condition of $\alpha = 90°$ into equation (4.6) yields

$$\frac{F}{F_p} = \frac{1}{1 - \dfrac{\mu \cos\theta'}{\sin\theta' + \mu \cos^2\theta'}} \tag{4.10}$$

Equations (4.9) and (4.10) are plotted in Figure 4.2 as a function of the wedge semi-angle. It is clear from the graph that there is not a significant difference between the two formulas in the limiting case of no sloping angle. The values are within 3% over the entire range of θ. The dependence of the relative contribution of friction to the total longitudinal force on the wedge sloping angle can be clearly seen in Figure 4.3 where equation (4.8) is plotted versus the wedge semi-angle with varying α. As the sloping angle decreases, the frictional component becomes the dominant contributor (compared to the plastic force) at small wedge semi-angles. It should be noted, however, that the plastic force derived by Wierzbicki and Thomas (1993) is also a function of the projected wedge semi-angle. Adding the newly developed contribution of friction, the total force becomes

(4.11)

$$F_p = 1.67\sigma_o \left(\bar{\delta}_t\right)^{0.2} t^{1.6} l^{0.4} \left(\sin\theta'\right)^{0.4} \left(\cos\theta'\right)^{-1.2} \left[\frac{1}{1 - \frac{\mu\cos\theta'}{\sin\beta\sin\theta' + \mu\left(\cos^2\theta' + \sin^2\theta'\cos\beta\right)}} \right]$$

where σ_o is the flow stress of the material, $\bar{\delta}_t$ is a dimensionless crack opening displacement parameter, t is the material thickness, and l is the cut length. Separating the terms that depend on the wedge semi-angle in the initiation cutting force equation (4.11) yields the dependence of the total force on the wedge geometry as

$$g(\theta') = \frac{\sin^{0.4}\theta'}{\cos^{1.2}\theta' - \frac{\mu\cos^{2.2}\theta'}{\sin\beta\sin\theta' + \mu\left(\cos^2\theta' + \sin^2\theta'\cos\beta\right)}} \qquad (4.12)$$

Figure 4.4 is a plot of equation (4.12) which shows the weak dependence of the cutting force on the wedge semi-angle. This is especially true at small to moderate wedge semi-angles where the difference between the value of $g(\theta`)$ with $\alpha = 30°$ and $\alpha = 90°$ at $\theta = 30°$ is only 4%. This difference grows with increasing θ to 18% at $\theta = 45°$ for the previous sloping angles. The weak dependence of the cutting force on the wedge semi-angle was shown by Wierzbicki and Thomas (1993) for the case of $\alpha = 90°$. From Figures 4.3 and 4.4 it is clear that although the relative contribution of the different components (bending, membrane, and friction) of force change with the sloping angle, the magnitude of the longitudinal force does not vary significantly for small to moderate wedge semi-angles.

Wierzbicki and Thomas (1993) were able to define an optimum value of the wedge semi-angle based on the plot of $g(\theta`)$ with a varying coefficients of friction. Because the function minimum is different for varying wedge sloping angles, it is not

possible in this case. An approximate solution based on the kinematically admissible model can be obtained, however. Based on Figure 4.4, *the approximate "frictional multiplier" of the plastic force is equal to 1.35 for wedge semi-angles between 15 and 35 degrees regardless of the sloping angle and assuming a coefficient of friction of 0.3.*

4.1.2 Application of the General Solution to the Steady-State Phase

Observations during plate cutting experiments at MIT indicate that when the steady-state condition is reached, the principal points of wedge and plate contact are near the shoulders of the wedge. Here, there is a transition region defined by Wierzbicki and Zheng (1995) where substantial membrane tension and compression occurs as the cut flaps move from a transient rolling to stable condition. As the flap moves from the face of the wedge to the side, it is subjected to a complicated deformation pattern that shifts the axis of the rolled flap from a line parallel to the face of the wedge to an alignment parallel to the direction of wedge advance. Additionally, there is no continuation of plate bending during and after this deformation. This requires that there is no vertical component of velocity in this principal area of contact. Based on this assumption, the frictional force operates only parallel to the plane of the plate during steady-state cutting and the angle of relative frictional contributions, ζ, is equal to zero. Substitution of this condition into equations (4.6) produces

$$\frac{F}{F_p} = \frac{1}{1 - \dfrac{\mu \cos\theta'}{\sin\beta \sin\theta' + \mu \cos\theta'}} \tag{4.13}$$

Note that equation (4.13) reduces to equation (4.9) when the $\alpha = 90°$ and is the same solution developed by Wierzbicki and Thomas (1993). Equation (4.9) is the friction contribution used by Zheng and Wierzbicki (1995) in the steady-state cutting process. Equation (4.13) corresponds almost identically to the values obtained by equation (4.8) over the entire range of the wedge semi-angles for the same given sloping angle. Values

are within 4% of those shown in Figure 4.3 which is the graph of the initiation phase solution. The solutions for the relative contribution of friction to the longitudinal cutting force are comparable.

The dimensionless steady-state cutting expression developed by Zheng and Wierzbicki (1995) is

$$\frac{F}{2Bt\sigma_o}=\frac{t}{4\sqrt{6}B}\left[2\frac{B+R}{R}+1.27\frac{R}{t}+1.28\theta'^2\left(\frac{\cos\frac{\theta'}{2}}{\cos\theta'}\right)\frac{(R+B)^2}{Rt}\right](1+\mu\cot\theta') \qquad (4.14)$$

where one half of the wedge shoulder width is represented by B. The analytical minimum of the force was found by taking the partial derivative of the force with respect to the rolling radius, R, and setting it equal to zero. This solution removes the unknown flap rolling radius from the equation by

$$\frac{R}{B}=\sqrt{\frac{2\frac{t}{B}+1.28\theta'^2\left(\cos\left(\frac{\theta'}{2}\right)/\cos\theta'\right)}{1.46\cos\theta'+1.28\theta'^2\left(\cos\left(\frac{\theta'}{2}\right)/\cos\theta'\right)}} \qquad (4.15)$$

Replacing the last term in equation (4.14) with the right hand side of equation (4.13) yields the steady-state equation with dependence on the wedge sloping angle as

(4.16)

$$\frac{F}{2Bt\sigma_o}=\frac{t}{4\sqrt{6}B}\left[2\frac{B+R}{R}+1.27\frac{R}{t}+1.28\theta'^2\left(\frac{\cos\frac{\theta'}{2}}{\cos\theta'}\right)\frac{(R+B)^2}{Rt}\right]\left(\frac{1}{1-\frac{\mu\cos\theta'}{\sin\beta\sin\theta'+\mu\cos\theta'}}\right)$$

Figure 4.5 shows the effect of varying the wedge sloping angle on the non-dimensional steady-state cutting force for a fixed wedge width and plate thickness. Contrasted with the behavior of $g(\theta')$ in the initiation phase, the non-dimensional steady-state cutting force exhibits a similar behavior but with a distinctly shifted period of constant value at small wedge semi-angles. The range of wedge semi-angles over which the force ratio is constant, regardless of wedge sloping angle, is approximately 7° to 20°. At $\theta = 45°$, the difference between the force ratio at $\alpha = 90°$ and $\alpha = 30°$ is a decrease of 45% (compared to a 17% drop in the initiation phase at these same data points). The steady-state cutting force is more sensitive to the effects of the wedge sloping angle and the subsequent variation in friction force than the longitudinal force developed in the initiation phase.

4.2 Relationship of Vertical and Horizontal Reaction Forces

Using the same prism model of the wedge (Figure 4.1), the relationship between the vertical and horizontal forces may be derived. The force ratio of vertical to longitudinal forces cannot be uniquely determined since the coefficient of friction and the actual points of contact of the plate on the surface of the wedge are unknown. The consideration of these unknown parameters requires that assumptions be made to solve the force relationship. In this study, the coefficient of friction is assumed to be equal to the textbook metal to metal, unlubricated, sliding friction value of 0.3. Furthermore the point of contact on the wedge is assumed differently for the initiation and steady-state cutting phases. The point of contact during initiation is between the tip and shoulder of the wedge. This allows the plate flaps to travel upwards on the face of the wedge with the velocity of equation (4.7). In the steady-state condition, the primary contact point is at the shoulders of the wedge and, as noted in section 4.1.2, the vertical velocity component is zero. These are the two limiting cases that define the complex deformation mechanism observed when a wedge cuts through a plate.

Based on the vector decomposition of the normal and friction force in Appendix C, the summation of the vertical force components yields the total vertical force, F_v, as

$$F_v = F_n\left(\cos\beta - \mu\sin\zeta\sin\beta\right) \tag{4.17}$$

Combining this with equation (4.5), the general solution of the vertical to longitudinal force ratio is obtained as

$$\frac{F_v}{F} = \frac{\cos\beta - \mu\sin\zeta\sin\beta}{\sin\beta\sin\theta' + \mu\left(\cos\theta'\cos\zeta + \sin\zeta\cos\beta\sin\theta'\right)} \tag{4.18}$$

4.2.1 Coupled Forces in the Initiation Phase

Keeping the same assumption that $\zeta = \theta'$ during the initiation phase and using equation (4.18), the force ratio is described by

$$\frac{F_v}{F} = \frac{\cos\beta - \mu\sin\theta'\sin\beta}{\sin\beta\sin\theta' + \mu\left(\cos^2\theta' + \sin^2\theta'\cos\beta\right)} \tag{4.19}$$

The effect of the sloping angle is apparent in Figure 4.6 where equation (4.19) is graphed with respect to the wedge semi-angle with varying sloping angles. When α = 90°, the leading edge of the wedge is perpendicular to the plane of the plate, the vertical force on the wedge is a lifting force due to friction (shown as a negative force). As the sloping angle is changed however, the normal component of the reaction force becomes dominant, shifting the direction of the force downward on the wedge. The normal component in the vertical direction completely counteracts the friction force by the time a 20° change in the sloping angle is applied.

4.2.2 Coupled Forces in the Steady State Cutting Phase

Maintaining that there is no vertical velocity of the plate flaps at the shoulders of the wedge during steady state cutting, $\zeta = 0°$. By equation (4.18), the relationship between the vertical and horizontal forces becomes

$$\frac{F_v}{F} = \frac{\cos\beta}{\sin\beta\sin\theta' + \mu\cos\theta'} \tag{4.20}$$

In contrast to the coupled forces in the initiation phase, the steady-state phase force relationship is characterized by the vertical component of the normal which is unopposed by any component of the friction reaction force. As illustrated in Figure 4.7, the vertical force can be greater than the longitudinal force at large wedge-semi angles when the sloping angle becomes acute. Thus, in steady-state cutting, the hull girder experiences a greater lifting reaction force than in the initiation phase.

4.3 Contribution of Longitudinal Stiffeners to Resistance

The previous developments for the contribution of friction and the coupling of the vertical and longitudinal reaction forces experienced by the hull girder were based on a model of a wedge cutting a plate. In reality, the structure of a ship hull is much more complex with longitudinal girders, stiffeners, transverse frames, and bulkheads. Figure 4.8 illustrates basic ship structural elements. In order to study a more representative ship geometry, longitudinal stiffeners were added to the experimental models. Although not the primary goal of this investigation, several theories and techniques were developed and compared to determine their suitability to account for the effect on longitudinal stiffeners in grounding accident damage extents predictions.

4.3.1 Equivalent Thickness Approach

One method of accounting for the increased resistance in cutting and bending of a section due to the longitudinal stiffeners is the equivalent thickness approach. Figure 4.9 demonstrates the transformation of a stiffened plate to a plate of uniform thickness by

$$t_{eq} = t + \frac{A_s}{b} \tag{4.21}$$

In equation (4.21), t_{eq} is the equivalent thickness of the uniform plate, b is the stiffener spacing, and A_s is the cross sectional area of the stiffener. The transformation of the stiffened panel to a uniform thickness plate is termed "smearing." The equivalent thickness is then applied to the initiation and steady-state cutting formulas (equations (4.11) and (4.16)). This method was used by Bracco (1994) in comparing experimental and theoretical values of grounding forces and similarly by Paik (1994) in studies of the initiation force of a wedge indentation on stiffened plates. In both studies the leading edge of wedge was perpendicular to the plane of the plate ($\alpha = 90°$).

4.3.2 Equivalent Fully Plastic Bending Resistance Method

The smearing technique, although apparently effective in obtaining experimental agreement with theoretical developments in previous studies, is a rough approximation of a stiffened panel's strength in tearing and bending. An alternative approach is to consider the equivalent thickness of a plate with the same strength as the plate-stiffener combination in fully plastic bending. In pure bending, the sum of the normal forces is equal to zero such that

$$\sum F_n = 0 \quad or \quad \int_A \sigma_n \, dA = 0 \tag{4.22}$$

and the sum of the internal bending moments is equal to the total moment, M_b, on the beam

$$\sum M = M_b \quad or \quad \int_A \sigma_n \, z \, dA = M_b \tag{4.23}$$

where z is the distance from the plastic neutral axis of the body. In fully plastic bending, the stress distribution is assumed to have the same magnitude throughout the cross section, but opposite signs above and below the neutral axis. Using the terms for the plate-stiffener combination in Figure 2.1, equation (4.22) is used to find the neutral axis for the model which is some height, h, above the baseline of the section as

$$h = \frac{1}{2}\left(\frac{t_f \, b_f + t_w \, b_w}{b} + t_p \right) \tag{4.24}$$

(Note that in this case the neutral axis will be in the lower flange. Use of equation (4.22) in fully plastic bending requires that the cross sectional area above and below the neutral axis is equal.) The total bending moment on the section is then obtained from equation (4.23) as

$$\frac{M_b}{\sigma_n} = \left[\begin{array}{l} \frac{b_f}{2}\left(\left(t_f + b_w + t_p - h\right)^2 - \left(b_w + t_p - h\right)^2 \right) + \frac{b_w}{2}\left(\left(b_w + t_p - h\right)^2 - \left(-h\right)^2 \right) \\ + \frac{b}{2}\left(\left(-h\right)^2 + \left(t_p - h\right)^2 \right) \end{array} \right] \tag{4.25}$$

For a uniform section of width b, the fully plastic bending moment is

$$\frac{M_b}{\sigma_n} = \frac{b t_{eq}^2}{4} \tag{4.26}$$

Setting equations (4.25) and (4.26) equal allows the equivalent thickness in fully plastic bending to be calculated. It is reasonable to expect this thickness to be greater than that obtained by smearing the cross sectional area. Like the smeared equivalent thickness, this fully plastic bending thickness is applied to the initiation and steady-state cutting expressions in place of the actual plate thickness.

4.3.3 Comparative Contribution of Thickness to Bending and Membrane Energy

A examination of the test specimens revealed that the stiffeners underwent different deformation patterns for different wedge sloping angles. This led to a hypothesis that the stiffeners do not always increase the longitudinal resistance of the plate-stiffener combination in the same manner at different wedge sloping angles. To separate the different components of bending and membrane energy in the initiation phase plate cutting equation (4.11), the derivation by Wierzbicki and Thomas (1993) is revisited at an earlier step when the two components have not been combined and the total plastic work is equal to the combination of the rates of bending, $\dot{E}_b$, and membrane work, $\dot{E}_m$, as

$$F_p V = \dot{E}_b + \dot{E}_m \tag{4.27}$$

Instead of combining the two components of energy with the same plate thickness, they are tracked separately through the derivation as the bending thickness, t_b, and the membrane thickness, t_m. The two thickness' are then observed to contribute an equal magnitude to the force as the plastic force becomes

$$F_p = 1.67\sigma_o \left(\bar{\delta}_t\right)^{0.2} t_b^{0.8} t_m^{0.8} l^{0.4} \left(\sin\theta'\right)^{0.4} \left(\cos\theta'\right)^{-1.2} \tag{4.28}$$

Assuming that the rolling action of the stiffener in conjunction with the plate flap does not contribute significantly to the bending portion of the plastic force, only the membrane energy contribution would be affected by the presence of the stiffeners in the

experiments. Using equation (4.21), the smeared equivalent thickness is substituted into equation (4.28) in place of the membrane thickness. The bending thickness value remains the same as the original plate thickness.

4.3.4 Comparison of Equivalent Thickness Techniques

Use of the different approaches to quantify the effect of the longitudinal stiffeners in the initiation phase is summarized in Table 4.1. Using the experiment specimen parameters from Table 2.3, the equivalent thickness has been computed for each technique and then raised to the appropriate power to demonstrate the techniques effect on the initiation phase cutting equation (4.11).

Table 4.1 Comparison of Equivalent Thickness Approaches for Longitudinal Stiffeners (Initiation Phase)

Approach to t_{eq}	**Formula**	**Value ($mm^{1.6}$)**	**Change from $(t_p)^{1.6}$**
Plate thickness	$(t_p)^{1.6}$	1.216	N/A
Smearing (by area)	$(t_{eq})^{1.6}$	3.048	150 %
Fully Plastic Bending	$(t_{eq\text{-}plastic})^{1.6}$	37.729	3002 %
Relative Contribution	$(t_{eq})^{0.8}\,(t_p)^{0.8}$	1.925	58 %

It is evident by an examination of Table 4.1 that the initiation phase force is highly variable depending on the method chosen to include the effect of longitudinal stiffeners. These different solutions will be compared to the experimental results in Section 4.5.1. Since only the initiation phase was attained during experiments, a similar steady-state analysis has not been developed.

4.4 Effect of Global Deformation on the Plate Cutting Mechanics

In Section 3.2, it was noted that there was a considerable amount of overall plate bending in some of the specimens ahead of the advancing wedge tip. This was especially evident in the sample where the wedge sloping angle was 45° and to a lesser extent on the specimen where $\alpha = 70°$. This out-of-plane deformation was not observed on the test specimen from Bracco's (1994) experiment where the wedge edge was perpendicular to the plane of the stiffened plate. This global deformation will change the projected wedge angle that is actually experienced by the plate. Figure 4.10 illustrates the effect of this local lift ahead of the wedge. The wedge sloping angle is effectively reduced by the magnitude of the global angle of lift which is defined as λ. This alters equation (4.2) and further reduces the projected wedge semi-angle as

$$\theta' = \tan^{-1}\left(\tan\theta \cos\left(90^{o} - (\alpha - \lambda)\right)\right) \tag{4.29}$$

To determine the significance of the global lift of the plate ahead of the wedge on the initiation phase cutting force, the variation of $g(\theta)$ (equation (4.15)) and the ratio of the vertical to horizontal force were graphed with a wedge sloping angle of 90° and 50° and then with a 10° global lift angle, λ, added to each. Figure 4.11 illustrates the effect of this lift on the solution for the initiation phase cutting force. The global lift angle has an insignificant decreasing effect on the force when the wedge sloping angle is close to the vertical. However, as the sloping angle rotates towards a more horizontal profile, the effect on the initiation force is more pronounced. This change is minor at small and moderate wedge semi-angles. For example at $\theta = 55°$, the decrease in force is approximately 8% when the global lift angle is added to the initial sloping angle of $\alpha =$ 50°. The effect on the vertical to horizontal force ratio is more significant as shown in Figure 4.12. Consideration of the global lift angle tends to increase the ratio throughout the entire range of wedge semi-angles. For the same condition of $\theta = 55°$ and $\alpha = 50°$, the addition of a 10° lift angle causes a 28% increase in the ratio from 0.4 to 0.6. It is clear

from this analysis that the total longitudinal force in the initiation phase is not very sensitive to the global lift angle at small and moderate wedge semi-angles but that the force ratio is quite susceptible to this phenomenon throughout the range of θ.

4.5 Comparison to Experimental Results to Theory

In this section, the experimental results are compared to the theory developed in this chapter. Both the longitudinal cutting force and the vertical to horizontal force ratios are compared.

4.5.1 Longitudinal Force Comparison

For the comparison of the total longitudinal force, the initiation phase cutting equation (4.11) is used since an examination of the specimens reveals that steady-state cutting was not attained. The experimental force is compared to three different curves representing three of the equivalent thickness approaches detailed in Section 4.3. The equivalent thickness of a uniform plate in fully plastic bending is not plotted since it represented a +3002% change in the force calculated using the plate thickness only. The following parameters were used in the calculation of the longitudinal force:

$$\sigma_o = 320 \text{ N/mm}$$

$$\bar{\delta}_t = 1$$

$$\theta = 45°$$

The flow stress was calculated for the material from tensile tests conducted by Bracco (1994). Strains were assumed to be in the 10 to 15% range during the plastic deformation associated with the cutting. The dimensionless crack opening displacement parameter value is taken from Wierzbicki and Thomas (1993) who showed that the solution has a weak dependence on its value. The wedges were all machined with a semi-angle of 45°

on a plane orthogonal to the leading edge of the wedge. The local angle of lift, λ, was measured from the specimens and is recorded in Table 4.2.

Table 4.2 Measured Local Angles of Lift Ahead of the Wedge

Experimental Sloping Angle (α)	**Lift Angle (λ)**	**Actual Sloping Angle (α)**
90°	0°	90°
70°	6.4°	63.6°
45°	13.3°	31.7°

This new sloping angle (90°, 64°, and 32° respectively) was used in the calculations along with the equivalent thickness' presented in Table 4.1. The force-cut length graph for each experiment is presented at the top of the page and the corresponding work-cut length graph is shown below it as Figures 4.13 through 4.15. The work was computed by integrating the force over the cut length using the trapezoidal rule. The work-cut length curve is used for the comparison of the theory and experiments since the experimental force levels fluctuate, making comparison difficult.

The results for Test No. 1, conducted by Bracco (1994), show that the technique for smearing the cross sectional area of the plate-stiffener section into a plate of uniform thickness successfully predicts the experimental work level. Over the range of 0.2 to 0.3 meters of the cut length, the work is $\pm$ 9% of the theoretical value. This is consistent with the results reported by Bracco (1994) and independently by Paik (1994). For test No. 2, however, the comparison reveals that this smearing technique is inadequate and over estimates the work by approximately 35% over the same range of cut length. Using the equivalent thickness for the membrane contribution and the plate thickness for the bending contribution of equation (4.11) brings the experimental values within $\pm$ 9% from 0.2 meters to the end of the test and $\pm$ 12% over the entire test. The plate thickness alone

in both of these cases underestimates the actual work performed. In the Test No. 3 (α = 45°), use of the plate thickness alone is the most accurate of the methods examined. Experimental values are 16% over those predicted at a cut length of 0.2 meters and this difference decreases to under 11% by the end of the test. The equivalent thickness in membrane energy and plate thickness in bending energy approach overestimates the work in this case by 35% at a cut length of 0.2 m.

An empirical solution relating the magnitude of the correlation thickness to the sloping angle in the initiation phase cutting solution can be developed from the experimental data. The thickness used for Test No. 1 is the full equivalent thickness while for Test No. 2 it is the combination of the relative contribution of membrane and bending thickness' as discussed above. To correlate Test No. 3, a 16% increase in the plate thickness to t = 1.31 mm was added. Based on these values, the relationship can be described as

$$\frac{t_{actual}}{t_{equivalent}} = 1 - 0.38\left(\frac{90° - \alpha}{45°}\right)^{0.52} \tag{4.30}$$

where the ratio of the thickness that correlates to experimental results to the smeared thickness is limited to a minimum value of 0.56 which defines the plate thickness. This relationship matches experimental results in the range of $90° \leq \alpha \leq 45°$ and is plotted in Figure 4.16.

Comparison of the behavior of equation (4.11) to other experiments is possible on a limited scope. Maxwell (1993) conducted wedge cutting experiments on non-stiffened plate with large wedge sloping angles. Figure 4.4 illustrated the behavior of the terms of the initiation phase cutting force, $g(\theta)$, with varying wedge sloping angles (equation (4.12)). At small to moderate wedge semi-angles, the magnitude of the cutting force is roughly constant for all wedge sloping angles. Maxwell tests on plate thickness' of 0.749, 1.143, and 1.829 mm support this theory. Comparing the force-cut length graphs when

plate thickness was 0.749 mm for wedge semi-angles of 20° and 30° and with a wedge sloping angles of 60° and 70°, respectively show a nearly identical force level over the first 0.2 meters of cut length. The forces then diverge, possibly as a result of the transformation from initiation to steady-sate cutting although it is difficult to discern from the photographs of the specimens. The force-cut length graphs for the other two thickness' follow a similar pattern but the sloping angle was the same for both wedge semi-angles ($\alpha = 70°$). Figure 4.4 predicts a 17% rise in the force if the wedge semi-angle is increased from these same test conditions to 45°. Using a cylinder to achieve a $\theta = 45°$, Maxwell measured an increase in magnitude of the longitudinal force on the order of 100%. Photographs of the specimens show a wrapping characteristic of the plate flaps around the cylinder which is in contrast to the rolling plate flap deformation patterns consistent with the wedge cutting model.

Lu and Calladine (1990) also conducted some plate cutting experiments with narrow wedge semi-angles and varying wedge sloping angles. These tests were conducted on a universal testing machine at a speed of 10 mm/min which is analogues to the quasi-static conditions used in the MIT experiments. The investigators conducted tests at a wedge sloping angle (using the nomenclature of this study) of 90°, 80°, and 70°. The wedges had a very narrow wedge semi-angle of 10° and 20° and most of the wedges did not have shoulders like those in this report. They noted that the energy absorbed decreased as α decreased. For $\alpha = 80°$, there was a decrease of energy absorbed of around 17% from the limiting case of $\alpha = 90°$. For $\alpha = 70°$, however, the reduction from the limiting case was 40%. This trend was seen in between Test No. 1 and Test No. 2 ($\alpha =$ 90° to $\alpha = 70°$) where the decrease in longitudinal cutting energy at a cut length of 0.2 m was approximately 39%. However, this is for a plate with longitudinal stiffeners. The cutting force variation on a plate is given by Figures 4.4 and 4.5 for the initiation and steady state phases respectively. At small wedge semi-angles, the wedge model solution for initiation and steady-state cutting predicts a fairly constant force as the increase in friction force balances the decrease in cutting force.

4.5.2 Comparison of the Vertical to Longitudinal Force Ratio

The force ratio measured in Test No. 2 and Test No. 3 is plotted against the initiation phase solution (equation (4.19)) and the steady-state solution (equation 4.20) in Figures 4.17 and 4.18. Results are summarized below in Table 4.3.

Table 4.3 Summary of Comparison of Experimental and Theoretical Values of the Vertical to Longitudinal Force Ratio

Test	Experiment	Initiation	Error	Steady-State	Error
2 ($\alpha = 70°$)	0.2	0.14	- 13 %	0.36	+ 44 %
3 ($\alpha = 45°$)	0.88	0.75	- 12 %	0.93	+ 6 %

The error percentage for the initiation phase values are referenced to the limiting case value of $\alpha = 90°$ ($\theta = 45°$) of -0.25. The experimental value of the force ratio for Test No. 2 is 0.2. This value is slightly underestimated by the initiation solution and overestimated by the steady-state solution by a large amount. The error associated with Test No. 3 is smaller for both solutions.

The two theoretical solutions bracket the experimental values. The initiation solution assumes $\zeta = \theta'$ and the steady-state solution assumes $\zeta = 0°$. To determine the actual angle of relative friction contribution, the surfaces of the two wedges were examined. The scoring pattern on the wedge face was approximated by a straight line and the angle of relative motion was measured with respect to the initial plane of the plate. For the 70° wedge, this angle measured 22.5° and was 17.9° for the 45° wedge. Substitution of these values into the initiation phase force ratio equation (4.19) yielded two additional theoretical values of 0.23 and 0.84 for $\alpha = 70°$ and 45° respectively. This agrees much more closely with the experimental values with errors of +7% and -4%. Prior exact knowledge of ζ is not available with the existing theory.

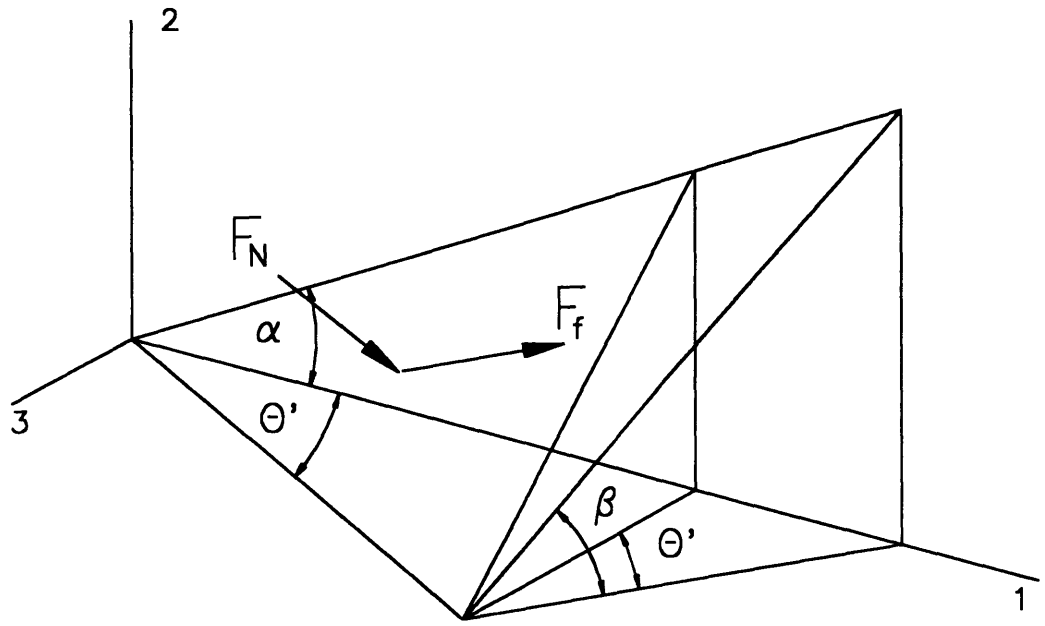

Figure 4.1 Diagram of Prism Model of a Wedge

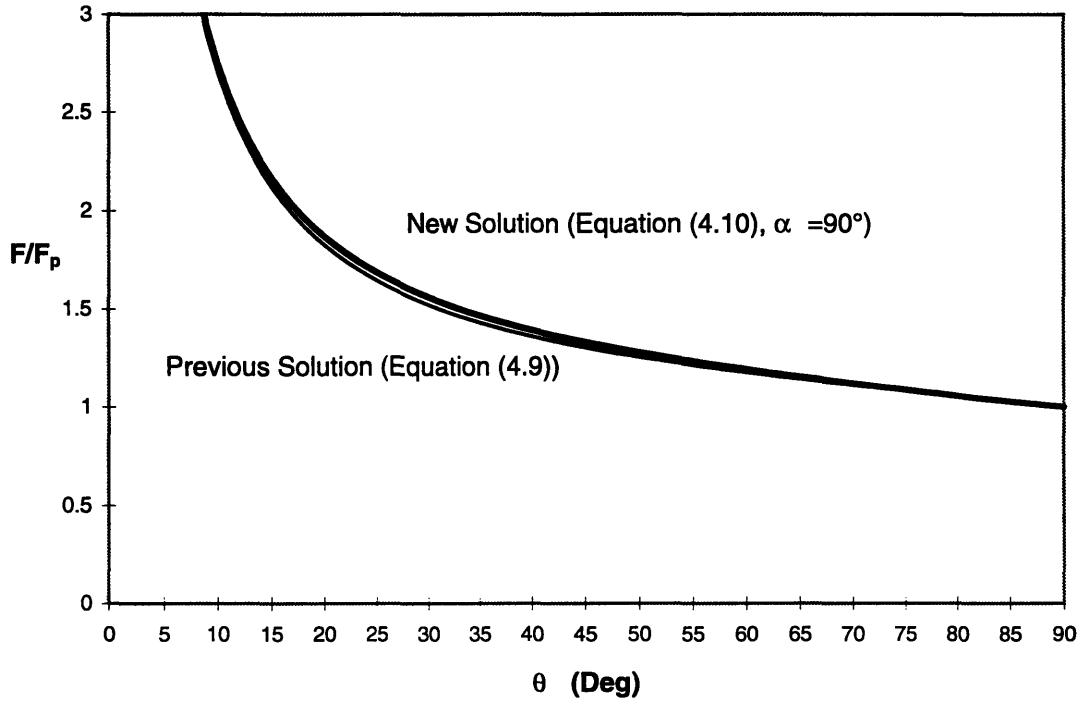

Figure 4.2 Comparison of the Contribution of Friction During the Initiation Phase Solutions (Equations 4.9 and 4.10)

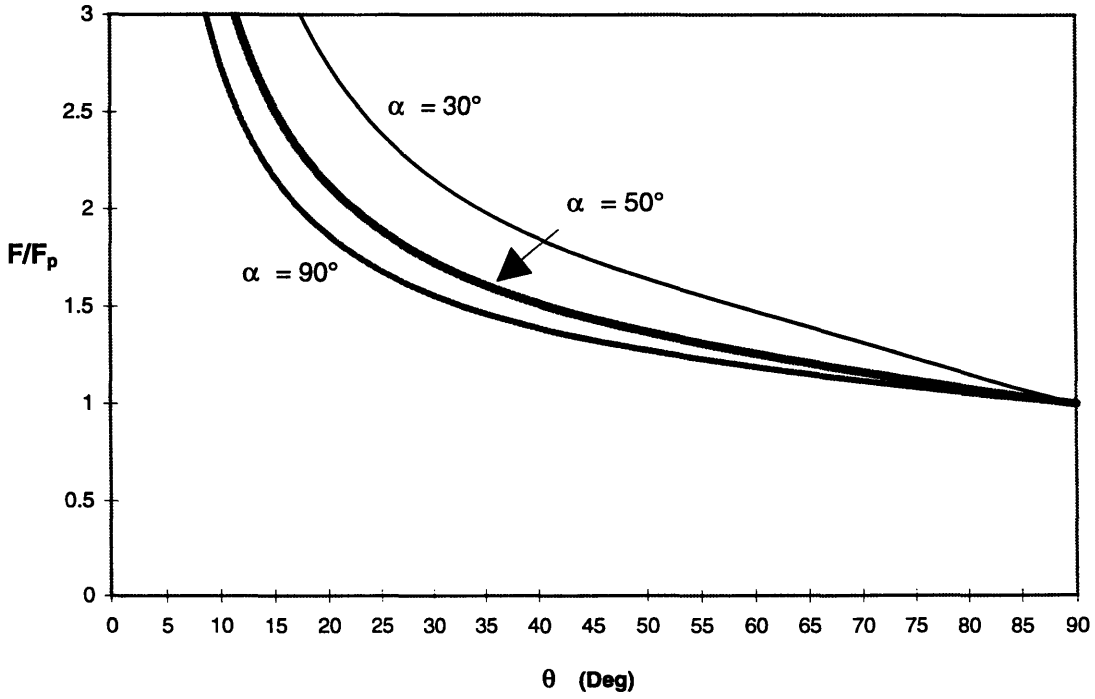

Figure 4.3 Effect of Wedge Sloping Angle on Contribution of Friction During Initiation (Equation 4.10)

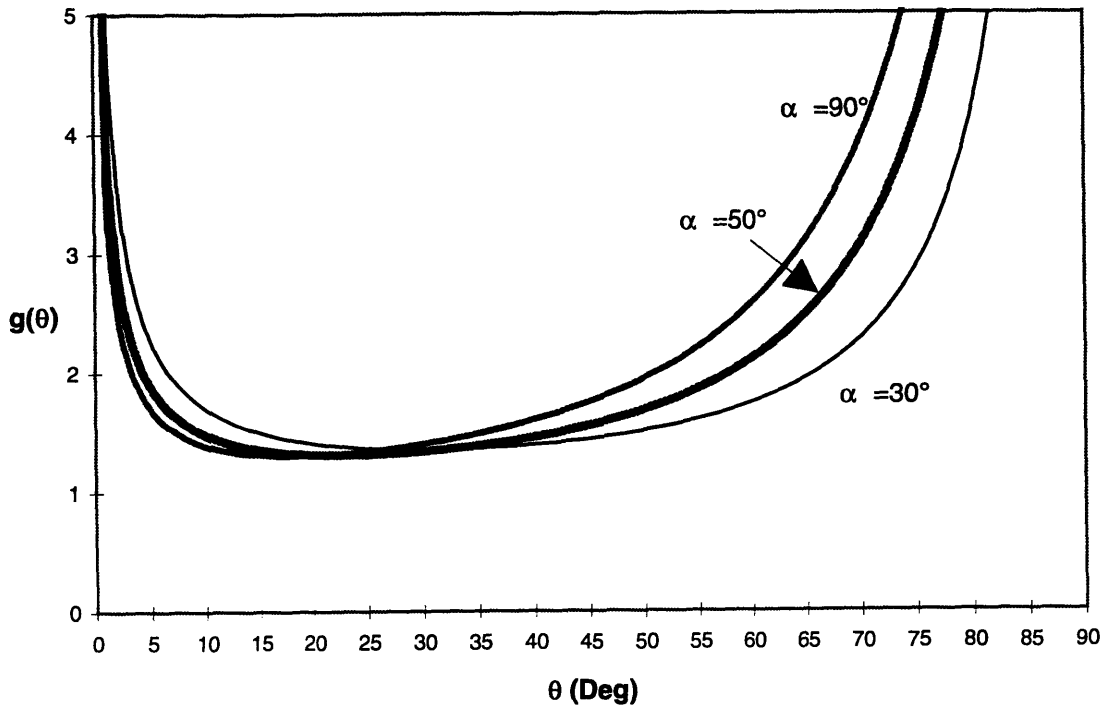

Figure 4.4 Variation of the Function g(θ) with Changing Sloping Angle (Equation 4.15)

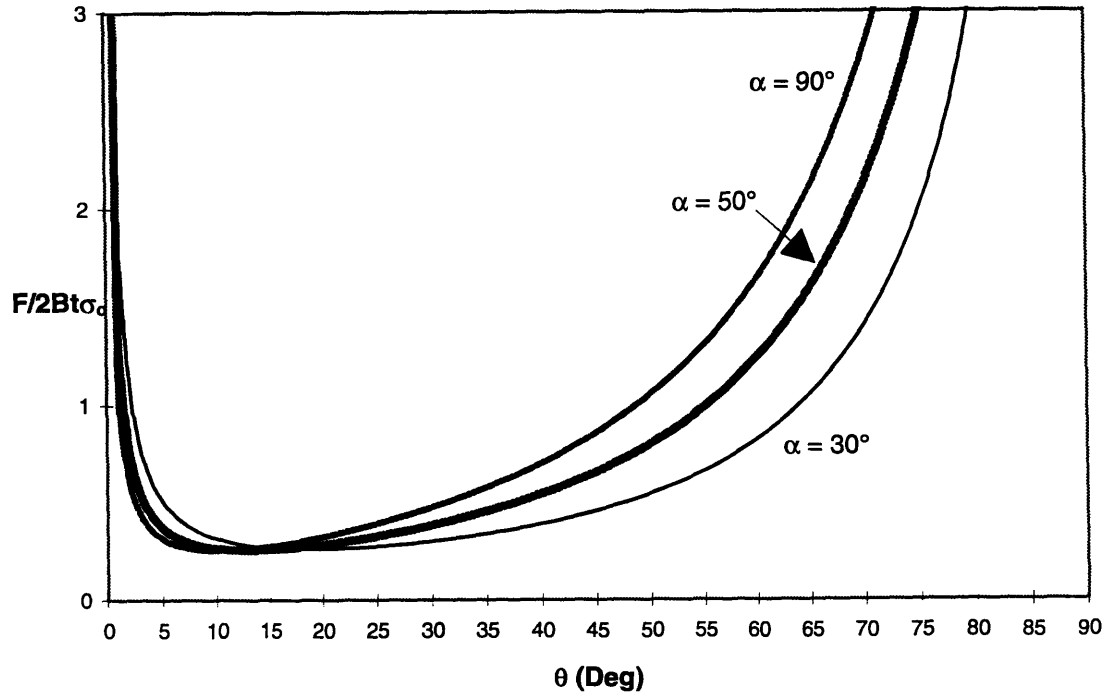

Figure 4.5 Effect of Wedge Sloping Angle on the Non-Dimensional Steady-State Cutting Force (Equation 4.16)

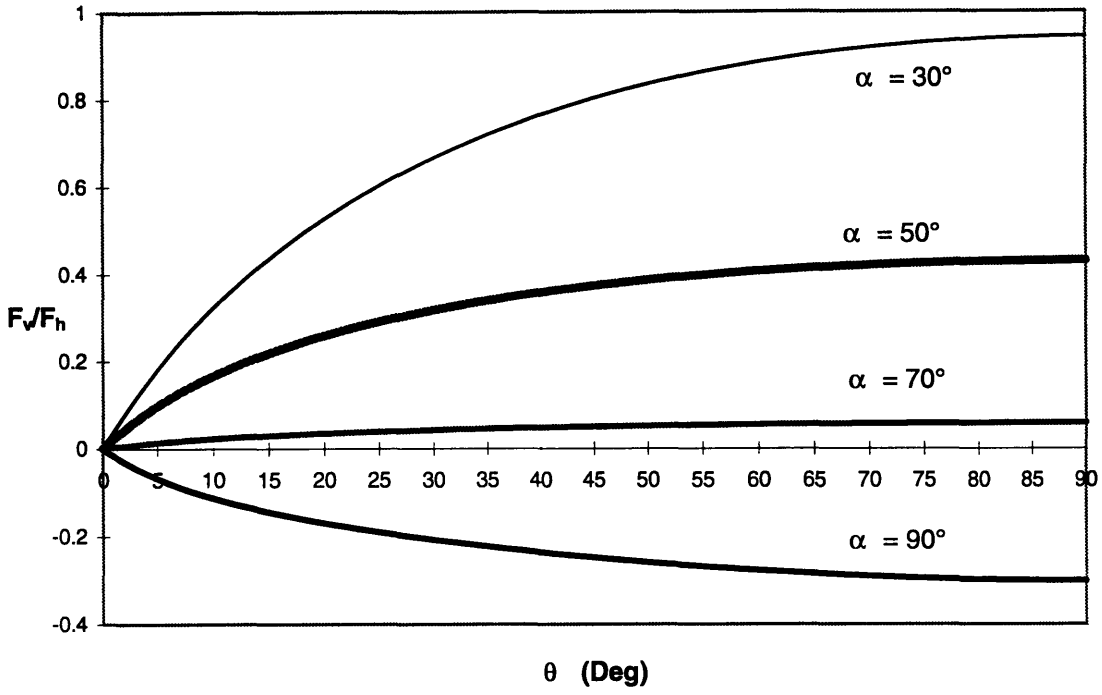

Figure 4.6 Coupled Vertical and Longitudinal Forces During Initiation Phase (Equation 4.19)

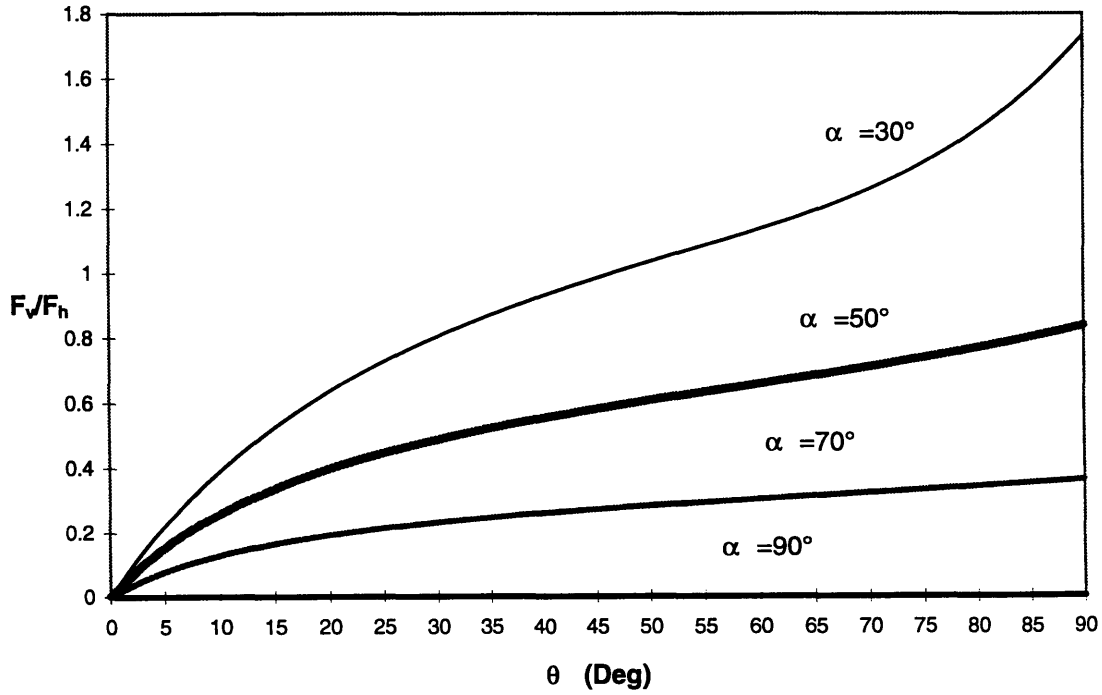

Figure 4.7 Coupled Vertical and Longitudinal Forces During Steady State Phase (Equation 4.20)

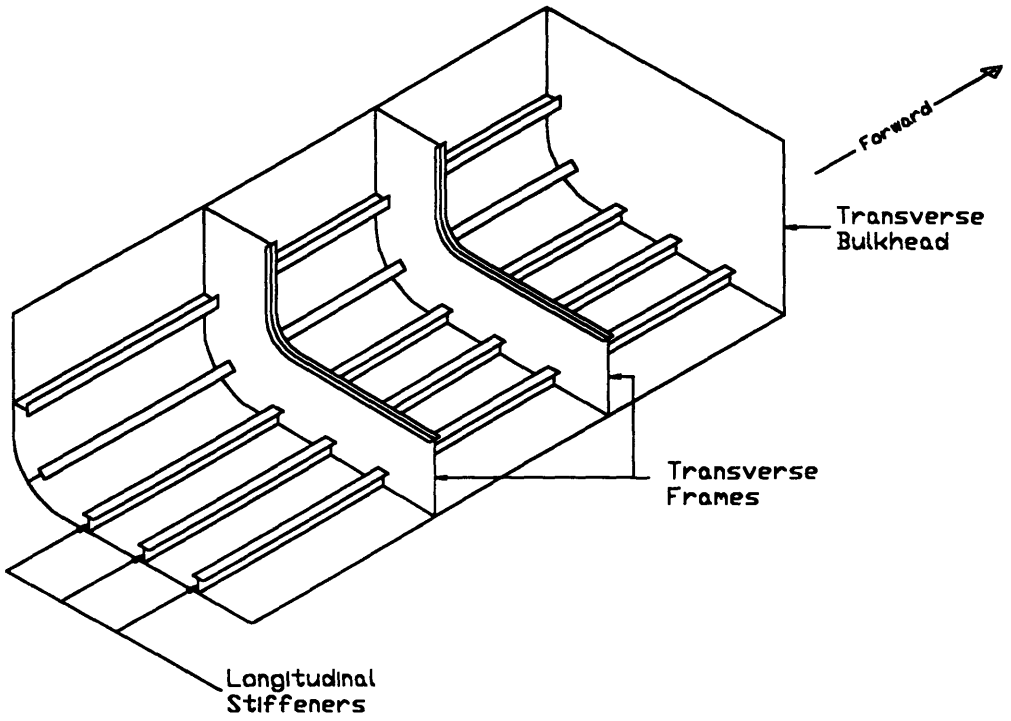

Figure 4.8 Typical Ship Structure (From Little (1994))

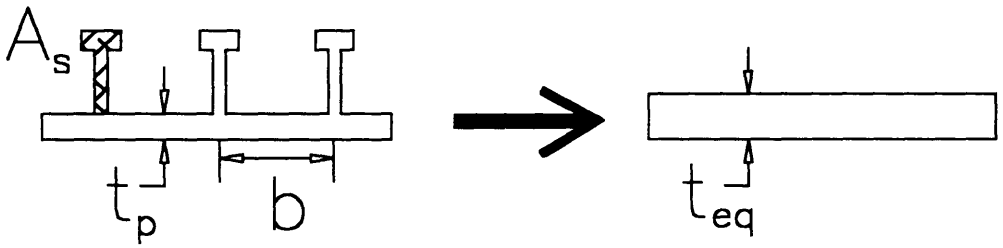

Figure 4.9 Stiffener Smearing Technique

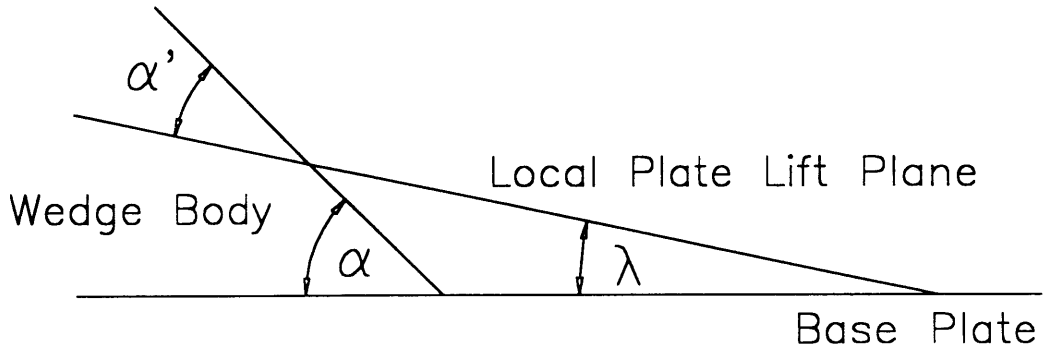

Figure 4.10 Effect of Lift Ahead of the Wedge

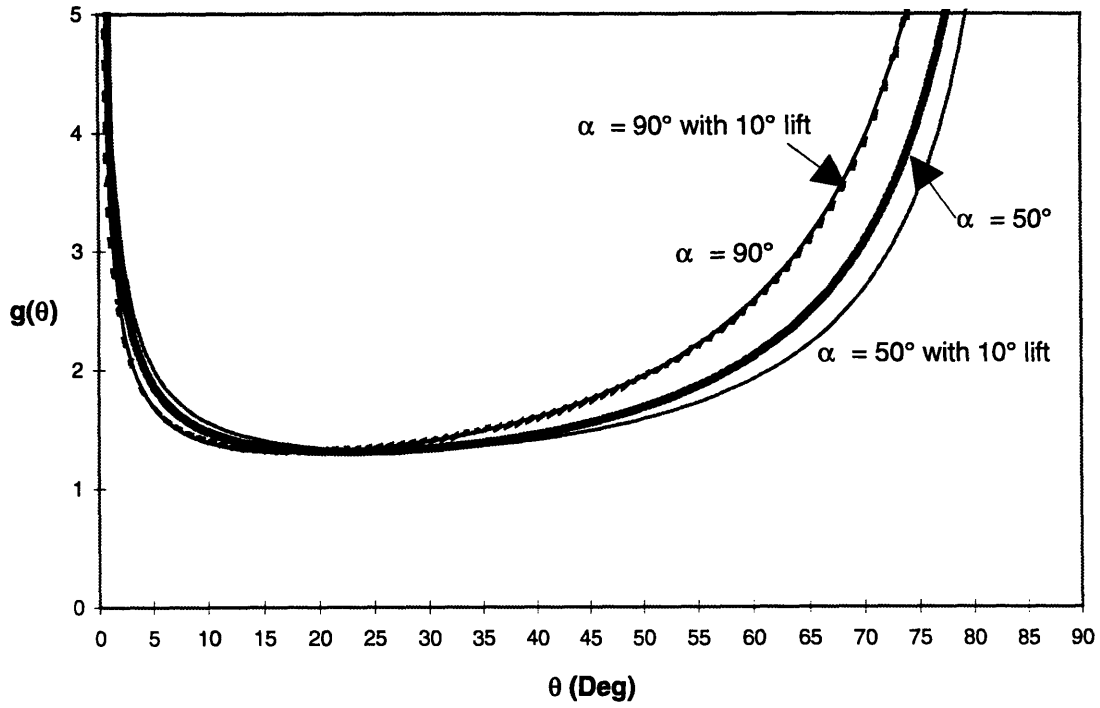

Figure 4.11 Effect of Local Plate Lift on Variation of $g(\theta)$ (Equations 4.15 and 4.29)

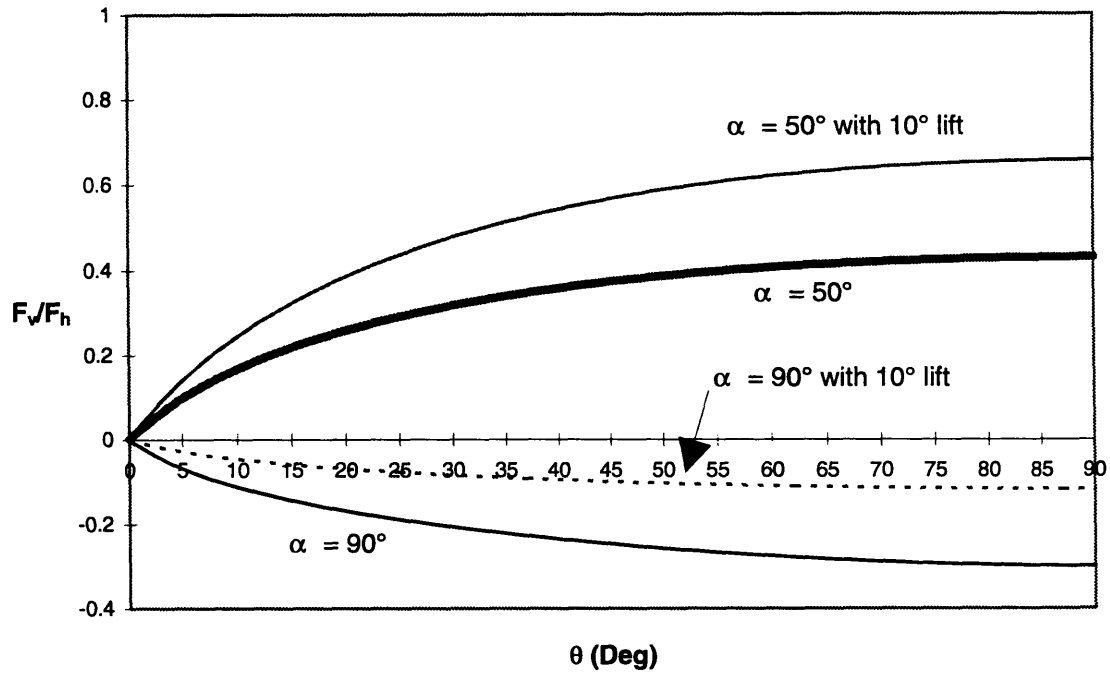

Figure 4.12 Effect of Local Plate Lift on Coupled Vertical and Longitudinal Forces During Initiation Phase (Equations 4.19 and 4.29)

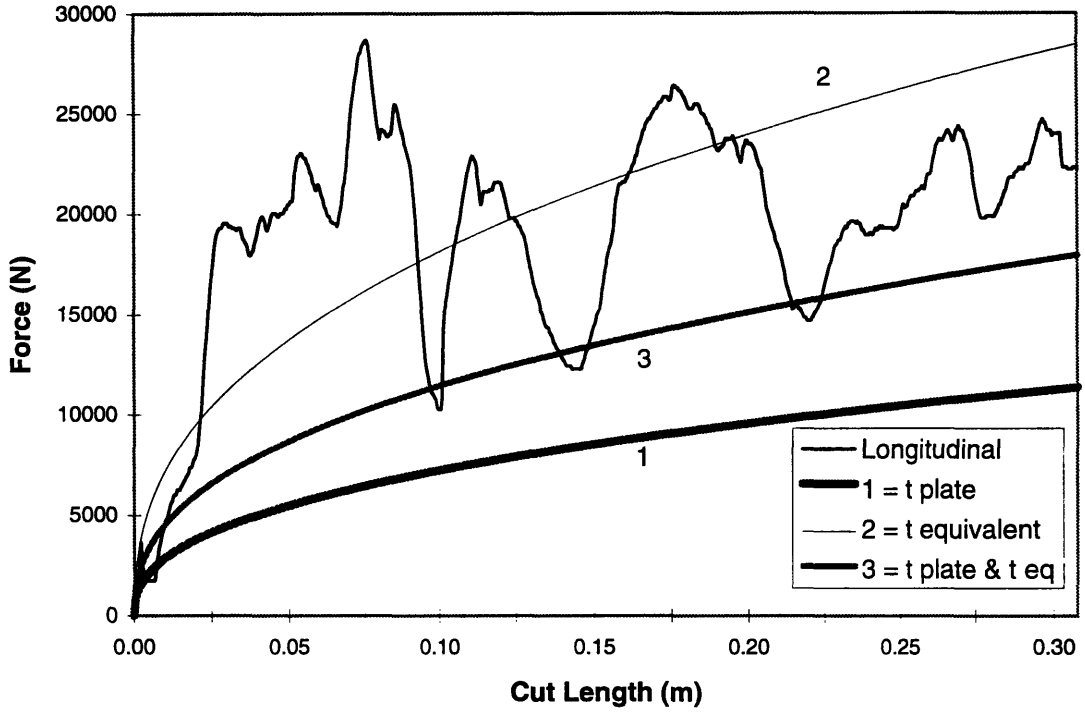

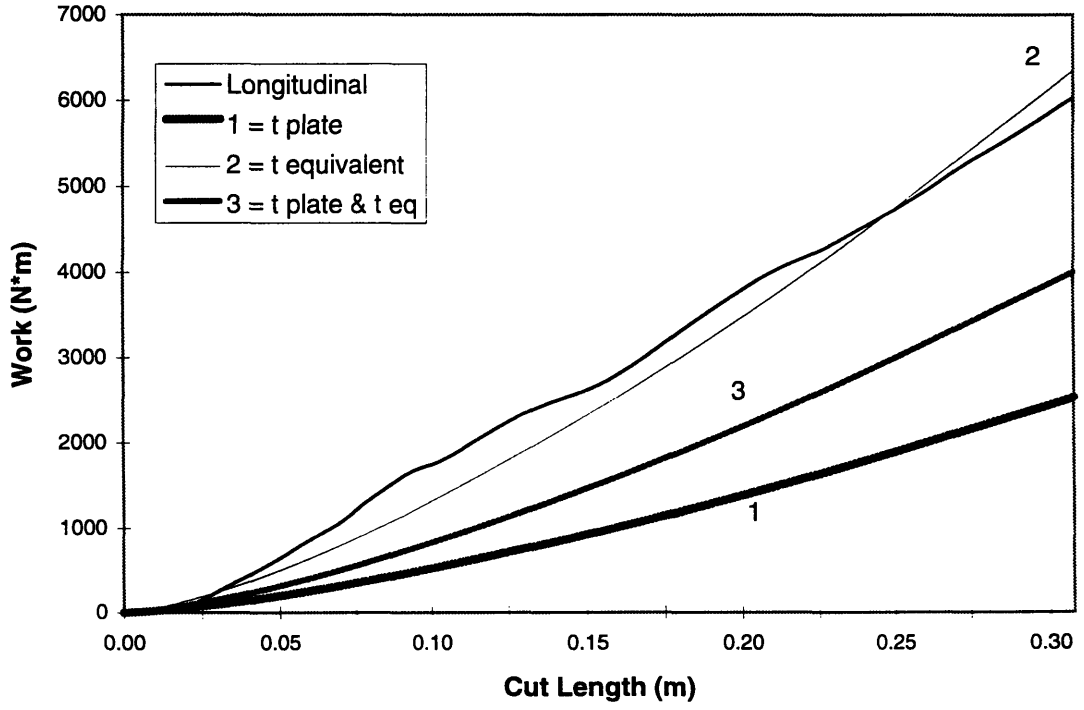

Figure 4.13 Force-Cut Length and Work-Cut Length Curves for Test No. 1 (LS-SH, θ = 45°, α = 90°) Comparison of Experiment to Theory

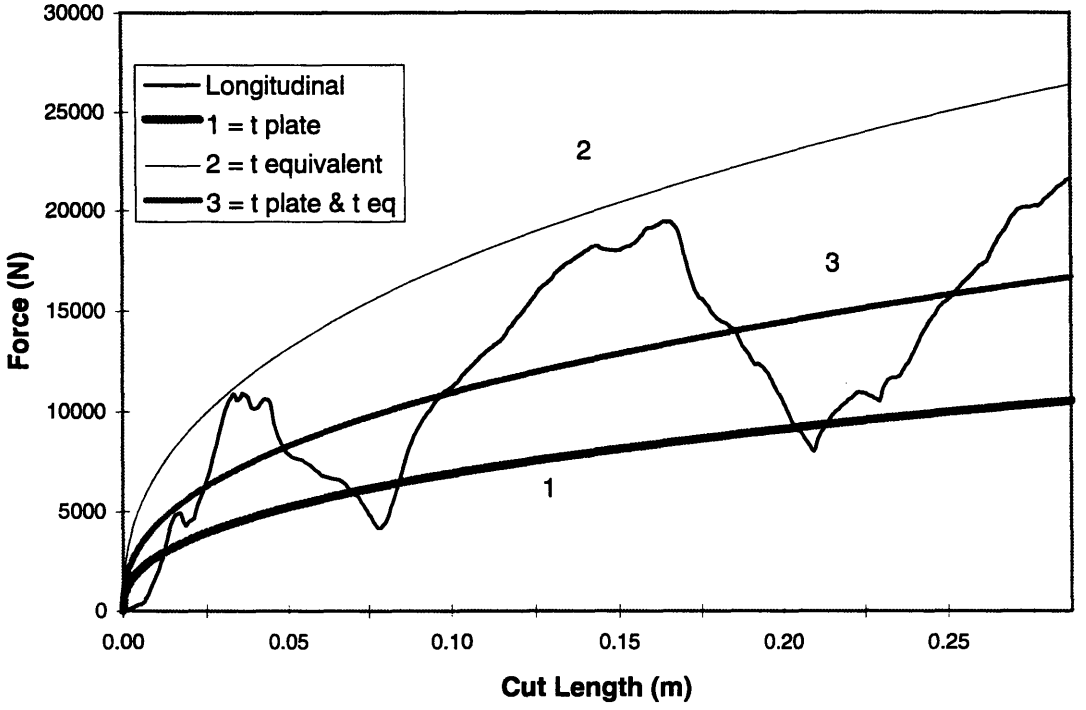

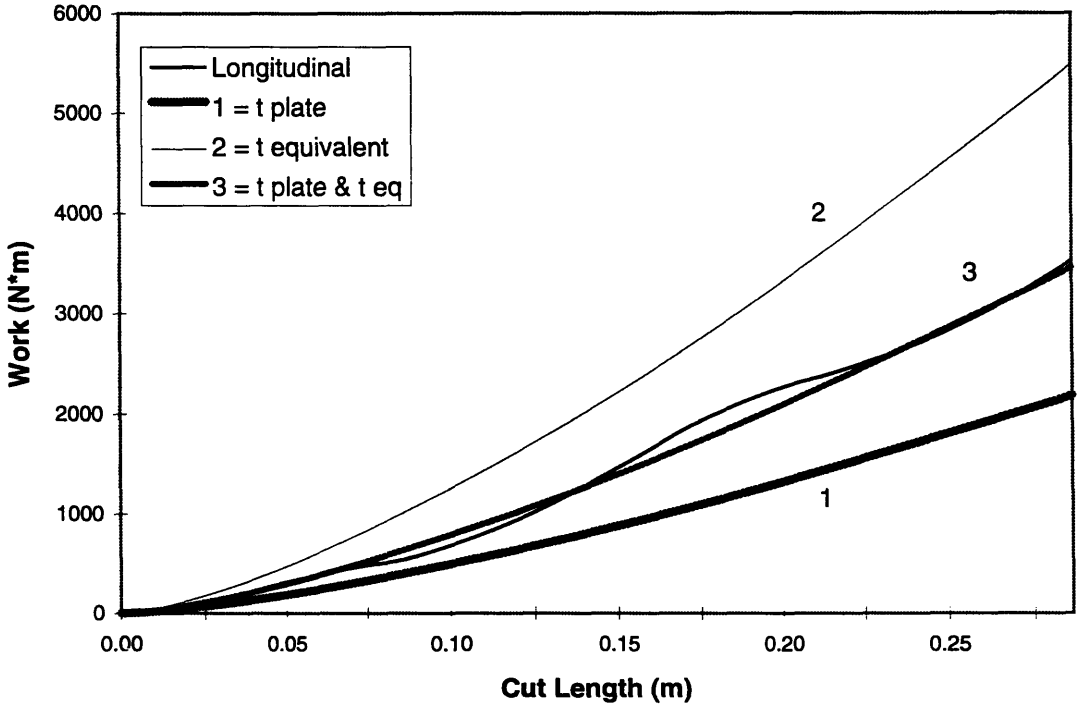

Figure 4.14 Force-Cut Length and Work-Cut Length Curves for Test No. 2 (LS-SH, θ = 45°, α = 70°) Comparison of Experiment to Theory

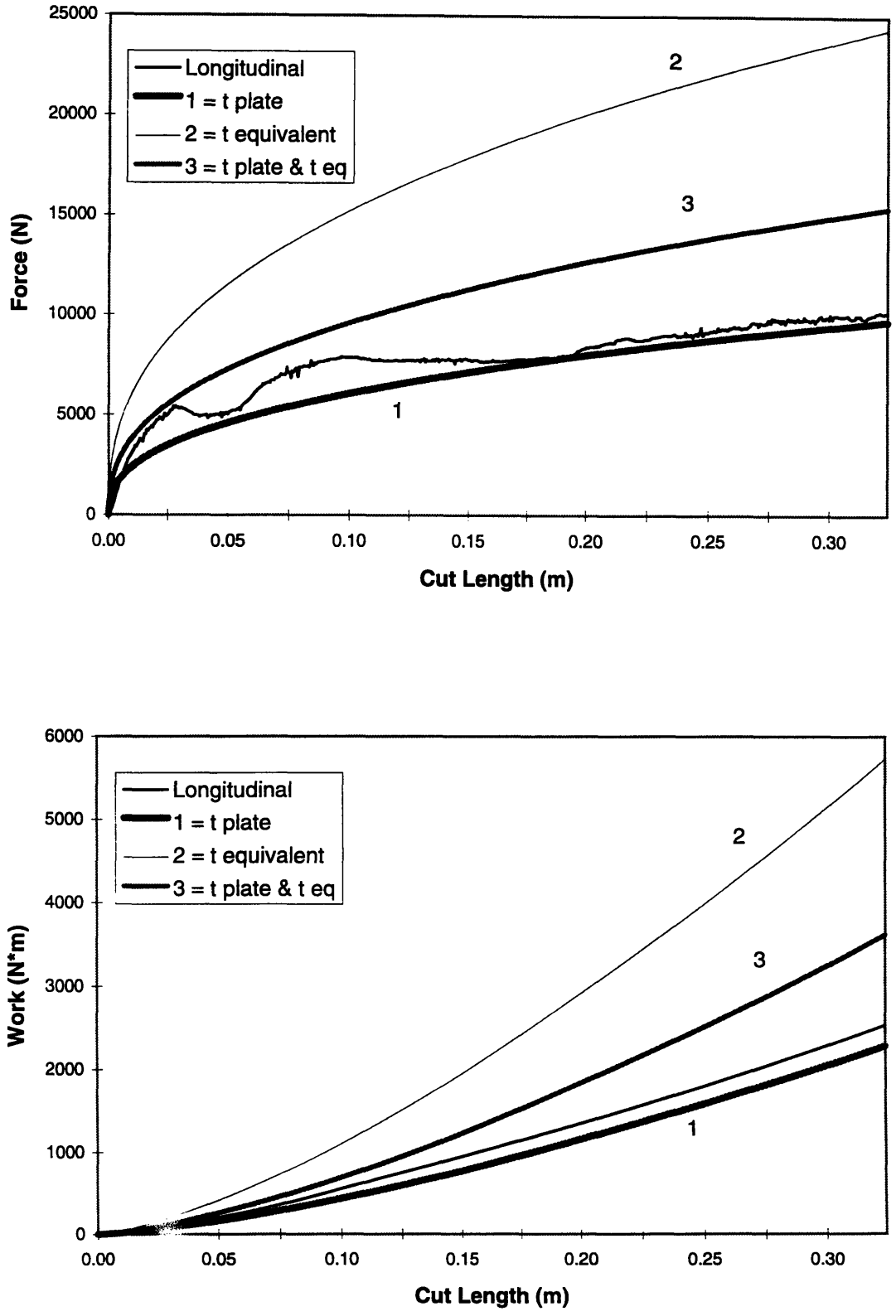

Figure 4.15 Force-Cut Length and Work-Cut Length Curves for Test No. 3 (LS-SH, θ = 45°, α = 45°) Comparison of Experiment to Theory

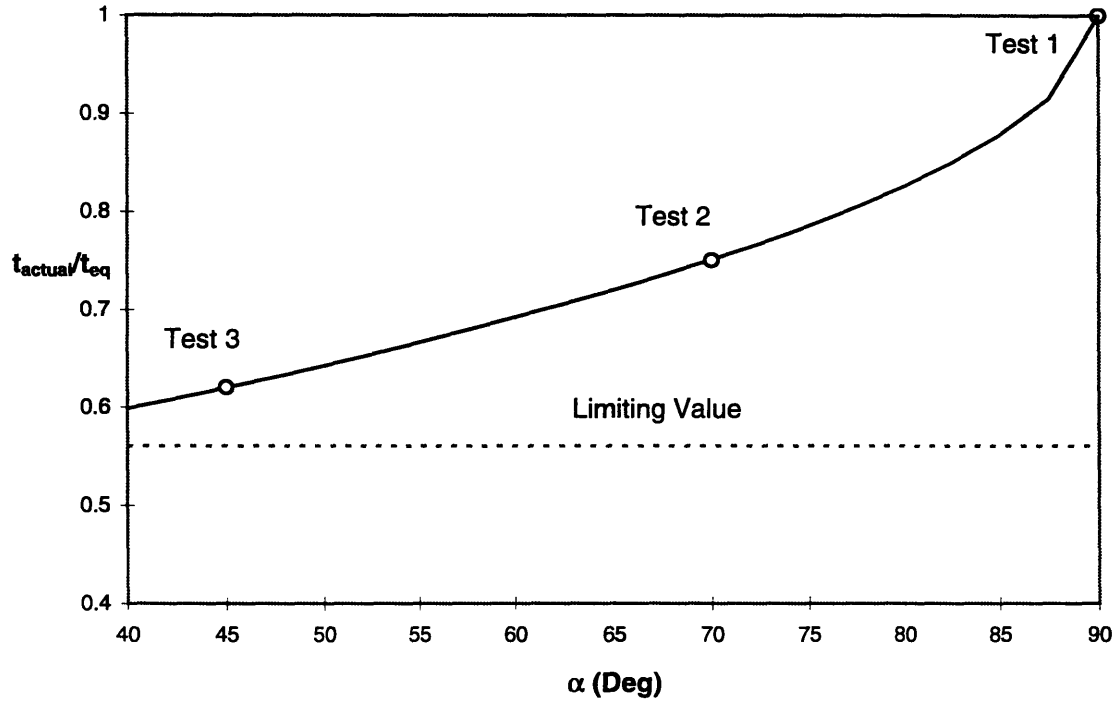

Figure 4.16 Empirical Relationship of the Actual Thickness to the Wedge Sloping Angle (Initiation Phase) (Equation 4.30)

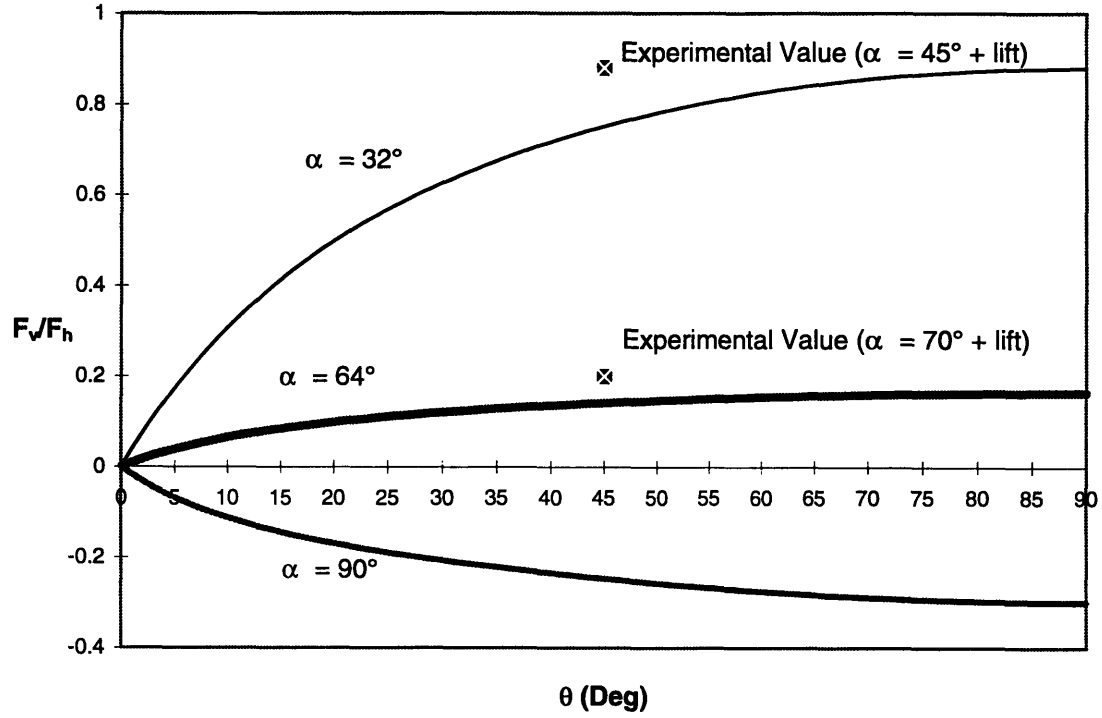

Figure 4.17 Coupled Vertical and Longitudinal Forces During Initiation Phase (Equation 4.19) - Comparison of Experiments to Theory

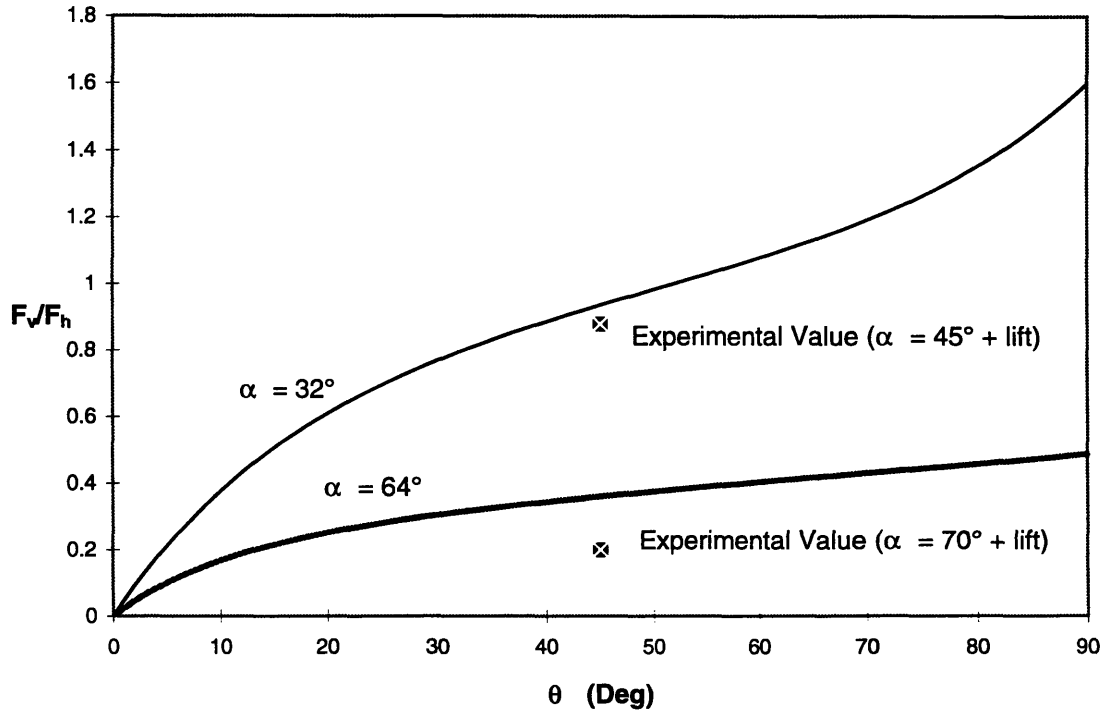

Figure 4.18 Coupled Vertical to Longitudinal Forces During Steady-State Phase (Equation 4.20) - Comparison of Experiments to Theory

5. Conclusions and Recommendations

This study is part of the *Joint MIT-Industry Program on Tanker Safety*. The ultimate goal of the project is to provide more accurate damage prediction methods for tank vessels in grounding accidents. These will assist in allowing more crashworthy designs of hull structures. Application of this type of analytical approach by regulatory agencies to develop design performance criteria would free designers and shipbuilders from static structural requirements and allow innovative design while maintaining a desired level of environmental protection.

This study contributes the development of the effect of friction on the plate-cutting process in the presence of a wedge sloping angle and the coupling of the longitudinal and vertical reaction forces on the hull girder. The coupled forces can be applied to the global ship motion problem to more accurately predict the extent of damage and overall ship response to grounding accidents. The effect of global lift of the damaged section on energy dissipation mechanisms is investigated. In addition, a comparative study of different techniques to account for the additional resistance provided by longitudinal stiffeners is undertaken. An empirical relationship between the initiation phase cutting force solution experimental thickness and the wedge sloping angle is developed.

5.1 Conclusions

Developing a new formulation of the contribution of friction in initiation and steady-state phases of plate-cutting allows incorporation of the wedge sloping angle into previously developed analytical solutions. Consideration of the vertical velocity of the plate flaps on the face of the wedge in the initiation phase provides a more complete solution. The relative contribution of friction to the longitudinal force in the initiation and steady-state cutting processes increases as the wedge sloping angle decreases. This increase is offset at small to moderate wedge-semi angles by the decrease in cutting force

as a result of the narrower projected wedge profile in the plane of the plate. The initiation phase equation exhibits this characteristic over a wedge semi-angle range of approximately $10° \leq \theta \leq 35°$ while the steady-state minimum occurs in the range of $7° \leq \theta \leq 20°$. Regardless of an application of a wedge sloping angle, the contribution of friction in the initiation phase solution over the noted range can be approximated by a "frictional multiplier" of 1.35. This theory, however, remains to be tested. The longitudinal stiffeners included in the experiments, which influence the plate-cutting mechanics and are not incorporated into the existing plate-cutting solutions.

The new friction contribution formulation was needed to couple the longitudinal and vertical reaction forces in grounding accidents. Use of the kinematic models and the condition of static equilibrium allowed the development of the force-coupling solutions as equations (4.18) and (4.19). The experimental values fall between the theoretical initiation and steady-state solutions. Steady-state cutting was not achieved in the experiments. Measurement of the angle of scoring on the wedges and substitution of this value into the initiation solution yields theoretical results that produce a 7% and 4% error in relation to the experimental values from Test No. 2 and 3 respectively. The effect of the longitudinal stiffeners on this solution has not been investigated. These results are based on two tests and should be validated by further experiments that measure the vertical and longitudinal forces with varying wedge sloping angles.

An examination of the models after testing revealed overall global lift on the stiffened plate sections. The effect of this lift is to decrease the longitudinal cutting force by means of a narrower projected wedge semi-angle and to increase the ratio of the vertical to longitudinal reaction forces. At $\alpha = 50°$ and $\theta = 55°$, the kinematic model predicts an 8% drop in the cutting force and a 28% increase in the vertical to longitudinal force ratio when a 10° global lift angle is considered in the initiation solutions. Model tests produced a 13.3° lift angle in Test No. 3, which has wedge geometry parameters similar to those noted above. Thus, at decreasing wedge sloping angles, global lift is an important consideration in the damage extent prediction.

It is clear from the examination of the test specimens that the stiffeners do not undergo the same deformation mechanisms at different wedge sloping angles. The various theoretical approaches to account for the additional resistance of the plate-stiffener section provide a wide range of solutions, none of which adequately provide accurate force values for all of the different wedge sloping angles investigated. The equivalent thickness approach suggested by Paik (1994) and Bracco (1994) appears to be suitable only when the cutting edge of the wedge is orthogonal to the plane of the plate. Likewise, in the case of Test No. 3, when $\alpha = 45°$, the stiffeners slightly increase the experimental cutting force over the plate prediction and the use of the plate thickness value alone in the initiation force solution provides an approximate solution.

Coupling the observations of the different stiffener deformation patterns observed during the experiments with this changing contribution to resistance demonstrates the complex mechanisms involved. The stiffeners inhibit plate-flap rolling postulated in the kinematic models for initiation and steady-state cutting. This will influence the moving bending hinge line velocity and, therefore, the vertical velocity component on the wedge face. This in turn, will probably reduce the angle of relative frictional contribution, ζ, in the initiation phase. It will increase the vertical to horizontal force ratio (as noted in the comparison of experimental results to theoretical models in Section 4.5.2 when the angle of scoring on the wedge face was used as ζ). An empirical relationship of the correlating thickness value for the experimental solution was developed that accurately fits the experimental data within the range of sloping angles tested. This relationship is based on three data points and only one stiffened plate section geometry. Further tests are required to validate this relationship and develop a general solution.

It is interesting to note the two different types of fracture observed in the experiments. As noted in Section 3.2, there was evidence of elastic fracture in Test No. 2 while plastic fracture was observed in Test No. 3. The material properties of the models used in each experiment were the same and temperature conditions were approximately

constant. The test speeds were identical. This duality in behavior, which is the ability of the model to fracture in both modes, will further complicate solution formulations. No explanation for the different behavior is offered in this report.

5.2 Recommendations for Future Study

To validate the new friction contribution formulas, plate-cutting experiments should be conducted with varying wedge sloping angles. The plates should be unstiffened to allow examination of the plate mechanics without influence by longitudinal stiffeners. Large wedge semi-angles should be included in the testing process to validate the theory over a broader range of wedge geometries than those examined in this study.

Likewise, the vertical and longitudinal force coupling equations should be tested on unstiffened plates. It is unclear what effect the stiffeners have on the coupling of the forces. Based on the experimental comparison to the theory, it appears that the increase in cutting force is matched by a rise in the vertical force so that the ratio of forces is maintained in the presence of stiffeners.

Analytical solutions to the twisting and crushing of web girders (longitudinal stiffeners) should be developed to allow a more accurate prediction of the contribution of longitudinal stiffeners to the overall resistance of the ship bottom structure in grounding accidents. These solutions should be coupled with the kinematic plate-cutting models developed by Wierzbicki and Thomas (1993) and Zheng and Wierzbicki (1995) to predict the changes to flap rolling radius, due to the additional resistance that the stiffener provides. This will allow more accurate prediction of the vertical velocity component and provide the angle of relative friction contribution, ζ.

The vertical to horizontal force relationship should be incorporated into the global motion and mechanics of the grounding problem. After hull rupture, there continues to be a vertical force on the damaged hull. This will cause one of two results: either the ship

will lift or additional plastic deformation will occur locally. If the ship lifts, the wedge sloping angle profile and the longitudinal cutting force will change, possibly reducing the amount of energy absorbed in friction, membrane, and bending mechanisms. Ship lifting constitutes a transfer of the kinetic to potential energy. If the vertical force is not of sufficient magnitude to lift the ship, the force will participate in further global section plastic deformation. This effect on overall damage extent is not as clear though it may result in deeper penetration and a wider region of distortion.

Elastic energy is not considered in the analytical solutions presented. In the experiments, however, some energy is stored through elastic mechanisms. Although this is assumed to be a small percentage of the total energy involved, this should be quantified. Jones and Jouri (1987) presented such a examination of their test apparatus and found up to a 10% loss of energy through the test apparatus. Such a study on the testing devices used in this investigation has not been conducted.

References

Akita, Y., Ando, N., and Kitamura, K., 1972, "Studies on Collision-Protective Structures in Nuclear Powered Ships," *Nuclear Engineering and Design*, pp. 365-401.

Bracco, M., 1994, "Grounding Resistance of Longitudinally Stiffened Single and Double Hulls," Naval Engineer's Thesis, Department of Ocean Engineering Massachusetts Institute of Technology.

Jones, N., and Jouri, W., 1987, "A Study of Plate Tearing for Ship Collision and Grounding Damage," *Journal of Ship Research*, Vol. 31, No. 4, pp. 253-268.

Kuroiwa, A., Kawamoto, Y., Yuhara, T., 1992, "Study on Damage of Ship Bottom Structures Due to Grounding," *First Joint Conference on Marine Safety and Environment Ship Production*, Delft University of Technology, pp. 731-742

Little, P., 1994, "Failure of Transverse Frames and Bulkheads in Grounding," M. Sc. Thesis, Department of Ocean Engineering Massachusetts Institute of Technology.

Lu, G., and Calladine, C., 1990, "On the Cutting of a Plate by a Wedge," *International Journal of Mechanical Science*, Vol. 32, No. 4, pp. 293-313.

Maxwell, L., 1993, "Effect of Rock Geometry on the Failure Mode of Plates and the Forces in Grounding Experiments," M. Sc. Thesis, Department of Ocean Engineering Massachusetts Institute of Technology.

Minorsky, V. U., 1959, "An Analysis of Ship Collisions With Reference to Protection of Nuclear Power Plants," *Journal of Ship Research*, Vol. 3, No. 1, pp. 1-4.

Paik, J. K., 1994, "Cutting of a Longitudinally Stiffened Plate by a Wedge," *Journal of Ship Research*, Vol. 38, No. 4, pp. 340-348.

Pippenger, D., Turgeon, J., Yahiaoui, M., 1995, "Split Wedge Deformation Experiments on Stiffened Plates," Joint MIT-Industry Program on Tanker Safety, Report No. 40, Department of Ocean Engineering, Massachusetts Institute of Technology.

Rodd, J., McCampbell, S., 1994, "Double Hull Tanker Grounding experiments," *The Advanced Double-Hull Technical Symposium*, National Institute of Standards and Testing, Gaithersburg, MD.

Vaughan, H., 1978, "Bending and Tearing of Plate with Application to Ship-bottom Damage," *The Naval Architect*, Vol. 97, May, pp. 97-99.

Vaughan, H., 1980, "The Tearing Strength of Mild Steel Plate," *Journal of Ship Research*, Vol. 24, No. 2, pp. 96-100.

Wierzbicki, T., Peer, D., Rady, E., 1991, "The Anatomy of Tanker Grounding," Joint MIT-Industry Program on Tanker Safety, Report No. 2, Department of Ocean Engineering, Massachusetts Institute of Technology.

Wierzbicki, T., and Thomas, P., 1993, "Closed-From Solution for Wedge Cutting Force Through Thin Metal Sheets," *International Journal of Mechanical Science*, Vol 35, No. 3/4, pp. 209-229

Woisin, G., 1982, "Comments on Vaughan: "The Tearing Strength of Mild Steel Plate," *Journal of Ship Research*, Vol. 26, No. 1, pp. 50-52.

Yahiaoui, M., Bracco, M., Little, P., Trauth, K., 1994, "Experimental Studies on Scale Models for Grounding," Joint MIT-Industry Program on Tanker Safety, Report No. 18, Department of Ocean Engineering, Massachusetts Institute of Technology.

Zheng, Z., Wierzbicki, T., 1995, "Steady-State Wedge Indentation, Improved Theory and Validation," Joint MIT-Industry Program on Tanker Safety, Report No. 42, Department of Ocean Engineering, Massachusetts Institute of Technology.

Appendix A

Supporting Calculations

A.1 Test Apparatus Design Calculations

Coordinate axes: x is horizontal, y is vertical

Set initial design parameters :

Wedge angles of attack: $\alpha p_i :=$

70·deg
45·deg

$\alpha_i := 90 \cdot deg - \alpha p_i$

Calculation of Expected Maximum Forces

Maximum vertical forces measured by Bracco (1994) for one longitudinally stiffened single hull:

$F_y := 29000 \cdot newton \qquad F_y = 6519.5 \cdot lbf$

Assume coefficient of friction: $\mu := 0.3$

For Bracco's experiment (1994), $\alpha = 0$ degrees, therefore, $F_y = N$ (the normal force):

$N := F_y$

and the tangential force is related by: $T := \mu \cdot N$

From simple 2 dimensional geometric relationships, solve for the maximum vertical and horizontal forces expected per wedge (one hull):

$$F_{xmax_i} := N \cdot \sin(\alpha_i) + T \cdot \cos(\alpha_i)$$

$$F_{ymax_i} := T \cdot \sin(\alpha_i) + N \cdot \cos(\alpha_i)$$

Table of maximum expected forces per wedge:

α_i / deg
20
45

$F_{xmax} = \begin{pmatrix} 4067.7 \\ 5992.9 \end{pmatrix} \cdot lbf$

α_i / deg
20
45

$F_{ymax} = \begin{pmatrix} 6795.2 \\ 5992.9 \end{pmatrix} \cdot lbf$

Calculation of Maximum Load Cell Deflection

Load Cell Specifications :

Manufacturer: GSE, Inc., Farmington Hills, MI
Model Number: FT-437
Type: Washer, full whetstone bridge
Make: Steel flexure with aluminum cover

Dimensions and characteristics:

Inner diameter: $d_i := 0.438 \cdot in$

Outer diameter: $d_o := 0.875 \cdot in$

Height: $h := 0.42 \cdot in$

Young's modulus: $E := 30 \cdot 10^6 \cdot psi$

Set Poisson ratio for elastic response: $\nu := 0.3$

Model as a thick-walled cylinder .

Coordinate system : z axis in line with height, θ for change in angle, r in the radial direction.

Boundary conditions : Assume compression along z axis only with no restrictions radially.

Assume worst case load: $P_{max} := -15000 \cdot lbf$ (compression)

Cross sectional area of cell: $A := \frac{\pi}{4} \cdot \left(d_o^2 - d_i^2\right)$ $A = 0.451 \cdot in^2$

Maximum stress allowable: $\sigma_z := \frac{P_{max}}{A}$ $\sigma_z = -33285.5 \cdot psi$

Other values due to boundary conditions: $\sigma_r := 0 \cdot psi$ $\sigma_{\theta\theta} := 0 \cdot psi$

Solve for deflection along the z axis and in the radial direction:

$$\varepsilon_z := \frac{1}{E} \cdot \left[\sigma_z - \nu \cdot \left(\sigma_r + \sigma_{\theta\theta}\right)\right] \qquad \varepsilon_r := \frac{1}{E} \cdot \left[\sigma_r - \nu \cdot \left(\sigma_z + \sigma_{\theta\theta}\right)\right]$$

$\varepsilon_z = -0.001$ $\delta_z := \varepsilon_z \cdot h$ $\varepsilon_r = 3.329 \cdot 10^{-4}$ $\delta_r := \varepsilon_r \cdot \frac{d_o}{2}$

$\delta_z = -4.66 \cdot 10^{-4} \cdot in$ $\delta_r = 1.456 \cdot 10^{-4} \cdot in$

Deflections are not significant even at maximum load. As a check on calculations, use the manufacturer's computed spring constant for the model FT-375 (one model below the FT-437) for displacement along the axis of compression. Where:

$K_{375} := 15.68 \cdot 10^6 \cdot \frac{lbf}{in}$ $\quad P_{max} = -15000 \cdot lbf$

$\delta_{z375} := \frac{P_{max}}{K_{375}}$ $\quad \delta_{z375} = -9.566 \cdot 10^{-4} \cdot in$

This agrees with the magnitude of previously computed maximum deflections. Load cell placement should allow some slight allowance for radial expansion. The maximum decrease in height will be applied to connecting rod deflection calculations to determine shear forces developed at the connecting rod/wedge interface. These shear forces developed should be small in comparison to those expected transverse forces for the measurements to be accurate.

Column Buckling

All rods are steel.

A. Outer support rods :

Radius: $r_{or} := 0.64 \cdot in$

Length: $L_{or} := 22.0 \cdot in$

Cross sectional area: $A_{or} := \pi \cdot r_{or}^2$ $\quad A_{or} = 1.287 \cdot in^2$

Moment of inertia: $I_{or} := \frac{\pi}{4} \cdot r_{or}^4$ $\quad I_{or} = 0.132 \cdot in^4$

B. Inner support rod : Made of two sections - Upper (u) and Lower (l)

Dimensions:	Lower	Upper
Width:	$b_l := 1.0 \cdot in$	$b_u := 1.25 \cdot in$
Height:	$h_l := 0.5 \cdot in$	$h_u := 1.25 \cdot in$
Length:	$L_l := 9.3 \cdot in$	$L_u := 11.75 \cdot in$
Cross sectional area:	$A_l := b_l \cdot h_l$	$A_u := b_u \cdot h_u$
	$A_l = 0.5 \cdot in^2$	$A_u = 1.563 \cdot in^2$
Moment of inertia:	$I_l := \frac{1}{12} \cdot b_l \cdot h_l^3$	$I_u := \frac{1}{12} \cdot b_u \cdot h_u^3$

Set boundary conditions : For all rods, assume a clamped-clamped condition since the upper crosshead is fixed and wedge deflection due to axial compression of the load cells is on the order of one-half thousandth of an inch. Therefore, the constant C in the Euler buckling equation is set equal to:

$$C := 4 \cdot \pi^2$$

For the outer rods (or) :

$$P_{orcritical} := \frac{C \cdot E \cdot I_{or}}{L_{or}^2} \qquad P_{orcritical} = 322437.4 \cdot lbf$$

For the inner rod (ir) :

To examine the entire length, use: $L_{or} := L_l + L_u$ $L_{or} = 21.05 \cdot in$

In the worst case, use the lower section moment of inertia although this will result in a very conservative estimate of the critical buckling strength.

$$P_{ircritical} := \frac{C \cdot E \cdot I_l}{L_{or}^2} \qquad P_{ircritical} = 27842.3 \cdot lbf$$

Both of the critical buckling load values are significantly below the maximum expected forces of approximately 14,000 lbs (total) vertical force (2 wedges).

Shear Calculation

As noted in the load cell deflection calculations, the shear generated at the connecting rod and wedge interface should be small compared to the overall forces measured transversely by the load cells.

From previous calculations, deflection along the axis of the load cell in compression is expected to be: $\delta_z = -4.66 \cdot 10^{-4} \cdot in$

Assume the wedge to be rigid. This implies that at each of the three rod/wedge interfaces on each wedge, the rod end will see this lateral deflection under the maximum load conditions. Again assuming a clamped-clamped condition, the bending moments at the center of the rods will be zero and the shear will be constant throughout the length of the rod. Using one-half the displacement at the center of the rod, compute the shear force developed by the lateral movement:

$$\delta_{zmiddle} := \frac{\delta_z}{2}$$

where for the outer rods: $L_{or} = 21.05 \cdot in$ $L_{ormiddle} := \frac{L_{or}}{2}$

and: $E = 3 \cdot 10^7 \cdot psi$

$I_{or} = 0.132 \cdot in^4$

solving for the force to produce this displacement (the shear) per rod:

$$P_{or} := \frac{|\delta_{zmiddle}| \cdot 3 \cdot E \cdot I_{or}}{L_{ormiddle}^3} \qquad P_{or} = 2.4 \cdot lbf$$

for the outer rods, only the lower parts will deflect since the upper section is on the centerline of the displacements and will cancel out:

$L_l = 9.3 \cdot in$ $\qquad L_{lmiddle} := \frac{L_l}{2}$

$E = 3 \cdot 10^7 \cdot psi$

$I_l = 0.01 \cdot in^4$

solving for the force to produce this displacement (the shear) per rod:

$$P_l := \frac{|\delta_{zmiddle}| \cdot 3 \cdot E \cdot I_l}{L_{lmiddle}^3} \qquad P_l = 2.2 \cdot lbf$$

The total shear developed on each wedge by the connecting rod interfaces will be:

$$P_{shear} := 2 \cdot P_{or} + P_l \qquad P_{shear} = 6.9 \cdot lbf$$

Comparison to expected values indicates this is an insignificant error in the measured forces for the purpose of this experiment.

$$\varepsilon_i := \frac{P_{shear}}{F_{xmax_i}}$$

α_i / deg	F_{xmax}	ε
20	4067.7 lbf	0.17 %
45	5992.9 lbf	0.115 %

A.2 Instrumentation Calculations

Once the instrumentation system has been set up, the capacity of the system must be examined to determine the voltages and gain used in the data acquisition process. For

this experiment limiting factors were the load cell excitation voltage capacity (12V DC), the excitation source voltage capacity (10V DC), and the computer data acquisition maximum voltage capacity (10V DC). The amplifier had a possible gain of x2000 and was not a limiting factor.

The larger the excitation voltage, the stronger the output signal from the load cell. The excitation voltage was set at 8V DC which is two-thirds of the load cell capacity. This margin was set so that in the unlikely event of spot loading which could produce a force greater than the load cell capacity of 15,000 lbs (resulting in higher than planned output voltages) the increased voltages would not burn the data acquisition board. Given these considerations, the appropriate gain was calculated to maximize the available voltage range in the data acquisition system.

For the following calculations, all volts are DC.

Set load cell excitation voltage to: $V_{excit} := 8 \cdot V$

Maximum expected output per load cell at approximately 9000 lbs (from calibration data sheets) :

$$V_{maxout} := V_{excit} \cdot 1.97 \cdot \frac{mV}{V} \qquad V_{maxout} = 15.76 \cdot mV$$

Maximum output at full load of 15000 lbs:

$$V_{maxout} := V_{maxout} \cdot \frac{15000}{9000} \qquad V_{maxout} = 26.267 \cdot mV$$

Limit of input voltage to data acquisition board: $V_{abslimit} := 10 \cdot V$

Target max input to the data acquisition board : $V_{target} := 6.0 \cdot V$

Maximum expected load is approximately 5000 lbs per load cell. Compute the expected maximum output volts per load cell.

$$V_{Aout} := V_{maxout} \cdot \frac{5000}{15000} \qquad V_{Aout} = 0.009 \cdot V$$

Compute gain at conditioner necessary to achieve this target at max load:

$$Gain := \frac{V_{target}}{V_{Aout}} \qquad Gain = 685.3$$

Set $Gain_A := 400$ to ensure adequate safety against spot loading.

In the event of spot loading to the maximum rated load of 15000 lbs, voltage to the board would be:

$$V_{maxout} \cdot Gain_A = 10.507 \cdot V$$

This is slightly higher than the data acquisition board capacity but unlikely to occur with constant monitoring during the experiment. Compute the maximum permissible load per cell at these settings:

$$L_{Amax} := \frac{V_{abslimit}}{V_{maxout} \cdot Gain_A} \cdot 15000 \cdot lbf \qquad L_{Amax} = 14276.6 \cdot lbf$$

Calculate board voltage at 5000 lb load:

$$V_{Aboard} := V_{Aout} \cdot Gain_A \qquad V_{Aboard} = 3.502 \cdot V$$

Percent of board capacity used:

$$Usage := \frac{V_{Aboard}}{V_{abslimit}} \qquad Usage = 35 \cdot \%$$

Appendix B

Operation of the Test Equipment

B.1 Instron Test Machine

All experiments were performed on a 20,000 lb capacity Instron, screw-driven, universal test machine. The test machine lacks documentation and operating guides so verification of data accuracy and calibration procedures was required prior to conducting any experiments. Due to unfamiliarity with the Instron test machine, assistance was received from Dr. J. Germaine of the Civil and Environmental Engineering Department. Dr. Germaine was indispensable to the experimental efforts. His contribution to understanding the machines operation and the subsequent testing and calibration of the Instron machine was enormous.

A major concern was the validity of the different test ranges offered by the Instron machine. Test ranges available were: 500, 1,000, 2,000, 5,000, 10,000, and 20,000 lbs. Connecting a voltmeter to the output jack, the various calibration and offset values at each of the different load scales was observed. The 20,000 lb scale however, drifted at both a zero load setting and at the calibration setting. Internal wiring and sensing problems are possible difficulties at this load scale. Because expected forces would be as high as 13,000 lbs per Bracco (1994), the system had to be tested to assure linearity of output data at twice the value of a load compared the set load scale. If this could be shown, the 10,000 lb scale could be used for higher forces and provide confidence that the output voltages were accurate up to 20,000 lbs.

Another issue of concern was the calibration procedures used to set the zero and full load voltages at each load scale. In the past, the Instron has been calibrated using a chart recorder and eye judgment. The chart recorder, however, has been previously damaged and repaired. Since the machine is no longer supported by the manufacturer, the

chart recorders accuracy is suspect. To avoid using the chart recorder as the calibration method, the Instron output required validation against a known load cell. This would allow validation of a calibration procedure using output voltages and the ZERO and CALIBRATION features of the machine.

As in any data acquisition system, the condition of the output data was also examined. Because the maximum output voltage setting on the Instron is 2V DC at any selected load scale and tests are generally performed below maximum load setting, signal noise is a serious concern. Dr. Germaine had previously installed a 1 Hz filter on the voltage output circuit. Observing different load outputs using the data acquisition system described later, large variations in the output voltage were evident on the order of approximately one half of the output value without use of the filter. With the filter, this noise was suppressed and voltage fluctuations were not significant. For all subsequent tests and machine operations, only the 1 Hz filter output line was used to record the output voltage.

The accuracy of the crosshead speed was also important. The Instron machine does not monitor displacement with time. Maxwell (1993) performed a check on the crosshead displacement with a dial indicator and found the accuracy within ± 4%. A repeat test was performed by Yahiaoui (unpublished) that correlated well. This is considered adequate for this set of experiments. Finally, the speed of the test was also an issue. Past tests have been performed at the speed of 1 inch per minute which allows for a fairly rapid experiment while maintaining the quasi-static nature of the test. The machine is labeled with a warning against this speed (due to fuse burn outs) but the option of a lower speed is 0.01 inches per minute which would require approximately 18 hours to travel the 11 inch test distance. This is unacceptably slow in terms of observation and the enormity of the data acquisition files generated. All test were conducted at the 1 in/min speed.

B.1.1 Linearity and Calibration Test

To test the linearity of the load cell output and the accuracy of the test machine and calibration technique, a test was conducted on 1 December, 1994. A 1,000 lb load cell was secured to the crosshead and Instron load cell (fixed). The calibration of the 1,000 lb load cell was known from previous calibration tests and this test was performed in tension. The Instron was configured per Table B.1 and the load scale selected was 500 lbs. Using the ZERO button, the no load output voltage of the Instron was set at 0.0V. By depressing the CALIBRATION button and adjusting the adjoining knob, the full load (500 lb) voltage was set at 2.0V. The load cells were connected to separate voltmeters and data was taken manually. Testing consisted of applying a small crosshead displacement and recording the Instron and attached load cell output voltages. No gain or signal conditioning was conducted on either output with the exception of the 1 Hz filter on the Instron output. The test range was 0 to 1,000 lbs (or 0 to 4 V) on the Instron to allow verification of linear output at twice the set load scale. Values were recorded in both the ascending (increasing tension) and descending operations. The results of the linearity test follow:

Test Load Cell:
Data Instruments 1,000 lb
Input Voltage: 5.495V DC
Calibration: 33.94 mV/V at full load

Instron Load Cell:
Instron 20000 lb
Range Setting: 500 lb range
Calibration Setting: 2.0V at 500 lb

Data and Linear Regression Results:

LA = Lower range, ascending tension
UA = Upper range, ascending tension
UD = Upper range, descending tension
LD = Lower range, descending tension

y values are in mV
x values are in V

Ascending Operation

$LAy_i :=$ $LAx_i :=$

-2.18	0
36.0	0.81
61.7	1.36
93.5	2.04

LAm := slope(LAx, LAy)

LAm = 46.894

$UAy_i :=$ $UAx_i :=$

93.5	2.04
120.5	2.61
152.0	3.28
182.5	3.93

UAm := slope(UAx, UAy)

UAm = 47.079

$$\text{Percent error} = \varepsilon_A := \left|\frac{LAm - UAm}{LAm}\right| \qquad \varepsilon_A = 0.394 \cdot \%$$

Descending Operation

$UDy_i :=$ $UDx_i :=$

182.5	3.93
153.3	3.31
120.5	2.61
93.6	2.04

UDm := slope (UDx, UDy)

UDm = 47.015

$LDy_i =$ $LDx_i :=$

93.6	2.04
61.6	1.36
35.5	0.80
2.09	0.01

LDm := slope (LDx, LDy)

LDm = 47.105

$$\text{Percent error} = \varepsilon_D := \left|\frac{LDm - UDm}{LDm}\right| \qquad \varepsilon_D = 0.192 \cdot \%$$

As shown by the data analysis, linearity is well established with errors in both the ascending and descending operations of less than 0.5%. Use of the 10,000 lb scale for expected forces up to twice this value is not a significant source of error and can be used with confidence.

To assess the validity of the calibration procedure, a test comparing the known calibration value of the 1,000 lb load cell and the Instron output was conducted. The data used is from the linearity test described above. The calibration test is detailed below.

Test Load Cell (Data Instruments - 1000 lb)

Calibration constant: $C := 33.94 \frac{mV}{V}$

Input Voltage: $Input := 5.495\,V$

Full load of test cell: $Load = 1000\,lb$

Calculate voltage at full load of test cell:

$$V_{lb} := \frac{C \cdot Input}{Load} \qquad V_{lb} = 0.187 \cdot \frac{mV}{lb}$$

Maximum voltage obtained on test load cell: $V_{testmax} := 184.68\,mV$

Comparison to Instron values

Compute Instron conversion factor: $V_{Instronmax} := 3.93 \cdot V$

$$Load_{Applied} := \frac{V_{testmax}}{V_{lb}} \qquad Load_{Applied} = 990.24 \cdot lb$$

$$V_{Instronlb} := \frac{V_{Instronmax}}{Load_{Applied}} \qquad V_{Instronlb} = 0.004 \cdot \frac{V}{lb}$$

Recall Instron Setting: 2V DC = 500 lb $V_{set} := 2.0 \cdot V$

$$V_{meas} := V_{Instronlb} \cdot 500 \cdot lb \qquad V_{meas} = 1.984 \cdot V$$

Compute error from measured to calibrated values for Instron test mac]

$$\varepsilon_{Cal} := \left| \frac{V_{meas} - V_{set}}{V_{meas}} \right| \qquad \varepsilon_{Cal} = 0.788 \cdot \%$$

The error between the expected value of 2.0V at 500 lbs on the Instron and that actually measured is less than 1%. This is acceptable for the experiment and the Instron was calibrated based on this test in all subsequent experiments. specific calibration procedures are detailed below in the Operation section.

B.1.2 Operation

The Instron machine requires at least a 30 minute warm-up period. Both the AMPLIDYNE and MAIN POWER switches must be energized to begin this period. Using Bracco (1994) and Yahiaoui et al. (1994) as guidelines, the machine settings were arranged as outlined in Table B.1. It is recommended that the test machine be set up in the proper configuration before energizing the machine.

Table B.1 Instron Test Machine Settings

Switch	Setting
FULL SCALE LOAD	Variable depending on experiment
LOAD CELL	CT-G
MARKER CONTROL	Manual
PRESET CYCLE COUNTER	Off
PACING CONTROL	Normal
ZERO SUPPRESSION CONTROL	Out
CHART DRIVE AMPLIFIER	Off
STRAIN GAUGE PRE-AMPLIFIER RANGE	10
LIMIT CYCLE	Off
AUTOMATIC	Stop
CYCLE CONTROL	Manual
CYCLE-LO	Stop
CYCLE-HI	Stop
SPEED CONTROL	-1-0.01
TRAVERSE	1
GEAR LEVER	High

To initially calibrate the universal testing machine, connect the 1 Hz output line to a voltmeter set to receive at least 2V DC. Set the load scale to 500 lbs and adjust the ZERO control knob until the output is 0V. Depress the CALIBRATION button to see what the output voltage value is for 500 lbs. Holding the CALIBRATION button depressed, adjust the CALIBRATION control knob until the voltmeter reads 2.0V. Recheck the zero setting and repeat the above steps until there is no change in the two settings. Increase the load scale to 1,000 lbs and re-zero the machine as above. Depressing the CALIBRATION button should now read 1.0V. Therefore, 1V is equal to a 500 lb force. Repeat this technique until the appropriate load scale is reached. For example, at the 10,000 lb scale, the calibration with a zero offset should read 0.1V indicating 0.1V equals 500 lbs and 2V equals a 10,000 lb load. This is generally the same procedure used by Little (1994) without using the chart as a calibration tool.

B.2 Transverse Load Cell Instrumentation Calibration and Settings

The data acquisition system must be properly tuned and calibrated before load cell calibration and testing may begin. (This section applies to the three load cells that are not a part of the Instron test machine.) The primary components that must be adjusted include the excitation voltage, the amplifier, the wheatstone bridge balance, and the gain on the conditioner/amplifier system. Note that the CAL switches on all channels of the 2120A Strain Gage Conditioner units are kept in the off position throughout all testing procedures. In addition, the outputs should be connected to the computer ribbon strip port only after these steps are completed to prevent any accidental inputs of large voltage to the data acquisition board. These steps are outlined in detail in the *2100 System Strain Gauge Conditioner and Amplifier System Instruction Manual* provided with the conditioner/amplifier. The equipment was manufactured by the Instruments Division of Measurements Group, Inc., of Raleigh, NC.

The following steps were followed prior to each test:

1) Excitation: The load cells are restricted to 12V DC input. The excitation voltage was calculated in Appendix A.3 for each type of experiment. Ensure that all EXCIT switches on the 2120A units are in the off position. For best precision, connect a digital voltmeter via banana jacks located on the front of the 2110A Power Supply. Set the scale to 20V DC. Turn the CHANNEL selector on the 2110A to the appropriate channel. Adjust the DC excitation voltage as required for that channel by turning the BRIDGE EXCIT with a small screwdriver. Follow this procedure for all channels.

2) Amplifier Calibration: To ensure no initial bias by the amplifier, the amplifier output voltage must be initially calibrated to zero. Keeping the EXCIT switches in the off position, adjust the AMP ZERO with a small screwdriver for each channel until both the (+) and (-) lights are extinguished. (If the (+) light is on, turn counter-clockwise.) Inability to extinguish both lights is an indication of excessive noise in the system.

3) Bridge Balance: Adjusting the balance compensates for any initial unbalance in the load cell wheatstone bridge. For each channel, turn the EXCIT switch to the on position and turn the BALANCE knob to extinguish both output lamps(similar to the amplifier calibration steps above). Once accomplished, turn the locking ring on the outside of the knob to lock the calibrated position into place. Turn the EXCIT switch to the off position when done.

4) Gain: The considerations for setting the gain are the expected load cell output voltage and the capacity of the data acquisition system including the computer itself. See Appendix A.3 for calculation details. The gain used in the two experiments is different. Set the GAIN knob to the appropriate scale and use the MULTIPLIER set screw set at x200. Note that the total gain is equal to the GAIN times the MULTIPLIER. Lock the GAIN knob in the appropriate position with the locking lever on the right side of the knob.

B.3 Load Cell Calibration

Prior to each test, the three transverse load cells must be calibrated. When purchased, each load cell was provided with a calibration certificate and a resistor. Each resistor is unique to a load cell and is tagged with a specified force. The resistor is placed in parallel with the load cell, the circuit is excited, and the resulting constant output voltage is recorded. This value is then used in the data reduction procedures after each test. It is possible to have the resistance characteristics of the wheatstone bridge change due to temperature differentials during the experiment. To ensure no or minimal change of the calibration constant over the course of the experiment, the calibration test is followed before and after the test. The following steps were performed prior to each test for each of the three (non-Instron) load cells and after system calibration and set-up and with all settings locked in place.

1) Installation: Install the resistor across the positive (+) excitation lead (red) and positive (+) signal lead (white). Ensure the resistor leads are firmly attached with good contact area.

2) Pre-test Calibration: Begin sampling with the data acquisition system. Provide the excitation voltage to the load cell. Once a steady signal is obtained over a reasonable length of time, quit sampling and secure the excitation voltage. Store the data. Disconnect the resistors.

3) Post-test Calibration: Soon after the testing is complete, reattach the resistor across the appropriate leads and repeat step #2.

4) Conversion Factor Calculation: The voltage corresponding to the given load (marked clearly on each resistor) may be obtained from the stored file. The conversion factor is then determined by dividing the appropriate load by the constant voltage obtained. This is done for both the pre and post-test measurements. The conversion factors are then compared. If there is a discrepancy, assume a linear change over the entire test and determine a conversion factor by fitting a line through the two data points.

B.4 Data Acquisition System

The Data Acquisition System used for both experiments is composed of a multifunction input/output (I/O) board and a software package. A *Lab-PC+* board was used. Principal characteristics of the board may be found in Table B.2. To complement the data acquisition and storage, the *Ni-Daq* for DOS software provided with the board was used. Set in the differential mode, the board has four input channels. These correspond to the Instron transducer and the three wedge transducers. A multiplexer is therefore not required between signal conditioning and the hardware.

Table B.2 *Ni-Daq* Computer Board Principal Characteristics

Resolution	12 bits
Channels	8 single ended or 4 differential
Maximum Sampling Rate	83.3 k sample/sec
Gain Available	1,2,5,10,20,50,100
Input Range	0 to 10V or ±5V
Over-Voltage Protection	±45V

B.4.1 *LAB-PC+* Hardware

The board was mounted inside a 433/L *Optiplex Dell.* Some of the original board settings were modified to accommodate the type of measurements to be taken. The maximum setting of an eight channel input is reduced by one half due to selection of the differential measurement mode for each of transducers. The change of voltage measurement mode from single ended to differential is one for which some board switches required resetting. The signal sources are grounded to the conditioner/amplifier to avoid allowing return paths to ground for bias currents. This was more convenient to physically construct and reduced the opportunity for signal error.

B.4.2 *Ni-Daq* for DOS Software

The software provided with the data acquisition board is adequate to conduct the experiment without any configuration changes. The main features of the software are described below.

Upon entering the *Ni-Daq* main menu, the configure menu should be opened. Set the input voltage to the differential and unipolar modes. This is necessary to measure the

voltages in the experiment configuration. Once done, the Strip Chart and Data Logger function should be opened. The main menu is described below.

Chan Setup is used to provide the correct number of channels on the board. Additionally, any gain applied at the board is set in this menu.. This gain setting is applied uniformly to all channels by *Ni-Daq.* In both of these experiments., no gain was applied at the board. This sub-menu is also used to individually tag the transducer signals.

Sample Rate is the rate of sampling between all channels. If only one channel is active, this represent the rate of data logging in measurement per second. When this is used with more than one channel, the sampling rate is divided by the number of channels to provide individual sampling rate for each channel. Since the experiment can be assumed to be quasi-static, the sample rate is chosen was 10/sec for each channel, or 40/sec overall.

Scan Rate is the rate to repeat scanning through the channels. A value of zero means that the scanning process is continuous and that each channel is sampling at the sample rate divided by the number of channels. This feature was set to zero for both experiments.

Average is an option that allows a reduction in the number of actual data point recorded and displayed to the screen. A green square is displayed on the menu option when activated. The entry given by the user represent the number of data point that will be averaged into one data entry. In these experiments, a sample rate of 10/sec per channel averaged every 10 produced one data entry per second.

Save is activated when a green lamp is lit on the appropriate key. It is vital to toggle it on *before* any data is recorded. Once the experiment is started, there is no way to save the data already observed on the viewer without stopping the data acquisition, selecting the Save key to the ON position, and restarting the operation. Once data

recording is completed, a menu appears when the save option is chosen. We recommended leaving the Append option ON in this sub-menu since this prevents the loss of data by mistake. A path and title are requested before the file is saved.

Pause is only useful in stopping the viewer, it does not stop data recording. Each channel has a small square representing it in the main menu. Each of those square should contain a black dot to indicate that they are active. They can be used to pause data recording on specific channels.

Range is only useful to change the scale of the viewer. It has no impact on the recording of data. If data falls beyond the viewer range limit, it will still be recorded to the data file as long as it is below the board voltage limit of 10V.

Plot On/Off activates the data recording. Note that a minimum of 200 points of data should be recorded after the switch is toggled on and before data can be saved once toggled back to OFF. This is especially important during calibration and for short recording, since data could be easily lost. It is recommended to leave the recorder on after completion and then delete any unnecessary data.

Plot Error and DAQ Error are codes that can be used in conjunction with the *Ni-Daq* manual to pinpoint a problem. A list of all the error codes may be found in annex to the second volume.

B.4.3 *Ni-Daq* Resolution

As transducer signals are led into an analog to digital converter, some error will occur. This error is due to the bit representation of the voltage measured and is termed resolution. Ni-Daq resolution is 12 bits for the entire range of 10V, which translates into a precision of 10V divided by 2^{12}. Hence, the smallest voltage that can be captured by the software is 0.0024 V. With the Instron load cell set at 2V for 10,000 lbs force, this

represents a maximum representation error of 12.2 lbs force, or a fraction of one percent. For the three other load cells the calibration for the load cells is approximately 2,400 lbs/V. This corresponds to an error of 5.85 lbs force .

The *Ni-Daq* resolution cannot be improved unless the gain is changed since this is a characteristic of the data acquisition board. Data viewing while the experiment is running is improved by setting the expected input voltages as close as possible to each other, and changing the viewer range accordingly.

B.5 Test Procedure

In this section are described the procedure for setting up the experiment. All the steps required are summarized in Figure B.1 which is reproduced and used as a check sheet during each experiment.

As specified in Appendix B.1, the Instron Test Machine requires a half hour to warm up. During this time the frame and test plates may be assembled. Some time is also required by the amplifier/conditioner to warm-up. The lab computer is set up such that upon being turned on, the *Ni-Daq* for DOS software appears on the screen and is ready for use. In the event that this does not occur, the user should leave *Windows* and change directory to *c:\Nidaqdos\Daqware* and type *Daqware*.

EXPERIMENTAL TEST PROCEDURE SHEET

Test Name:_____ **Date/Time:**

Wedge: **Samples:**

Operator:

Pre-Experiment Procedures:

- ☐ Energize Instron Test Machine (requires a 30 minute warm up)
- ☐ Check all wiring for proper connections and condition
- ☐ Energize computer, signal conditioner, and voltmeter
- ☐ Once in Daqware main menu,
  Choose Config menu; select Differential and Unipolar current, return
- ☐ Choose Chart Recorder and Data Logger
- ☐ Once in Ni-Daq for Dos,
  Set Save on,
- ☐ Select Chan Setup to 4 channels and identify the channels (0 gain)
- ☐ Complete load cell calibration procedures
- ☐ Calibrate the wedge transducers, saving the data file as:

  Load Cell Calibration (#1) Data File Name: C:\TEST_____ . CL1

- ☐ Complete physical set up of equipment, record transducer locations

  Load Cell #1:_____ **#2:**_____ **#3:**_____

- ☐ Set Instron controls, record setting and calibration with separate voltmeter

  Setting:_____ **Zero:**_____ **Calibration:**_____

Figure B.1 Experiment Test Procedure Checklist

☐ Check data acquisition sampling rate settings and record

Sampling Rate:____ (recom. 40) **Scan Rate:**____ (recom. 0)

Average Every:_____(recom. 10) **Average On:** **Y** N (recom. Y)

☐ Ensure that the green square indicate that Save is on, if not activate it

☐ Begin sampling (Plot On/Off switch)

☐ Initiate Instron movement

Note 1: The pause function on Ni-Daq for Dos does not stop data recording. If on the other hand the On/Off switch is used, ensure that the data is save under the same name and appended to the previously saved data.

Note 2: File should be identified as follows **ZBB_XXCY.DDD**

Z number representing the number of stiffeners
BB TF for transversely, LF for longitudinally
XX dated of the experiment (day)
C experiment number (a for 1, ...)
Y run number (1, 2,...)
DDD file extension; DAT for data, CL1 for initial calibration, CL2 for final calibration, and RDG for readings

Post-Experiment Procedures:

☐ Save the data file and record file name:

Data File Name: C:\TEST_____. DAT

☐ Check and record the Instron zero and calibration from the voltmeter

Zero:_____ **Calibration:**_____

☐ Recalibrate the transverse load cells, saving the data file as:

Load Cell Calibration (#2) Data File Name: C:\TEST_____. CL2

Figure B.1 Experiment Test Procedure Checklist

☐ Return the Instron to initial position and remove the test apparatus

☐ Make a back up copy of the data file onto floppy disk with the same name

☐ Secure all electronic equipment

☐ Complete test log

Figure B.1 Experiment Test Procedure Checklist

Appendix C

Vectorial Decomposition of Forces on Prism Model

C.1 Discussion

To determine the components of force that are a result of friction and the relationship between vertical and horzontal components, the plate cutting wedge is modeled as a prism. For simplicity, only one half of the wedge is modeled and the total force for one half of the wedge is (F/2). This will be neglected in the derivation and requires that the solution not be multiplied by a factor of two at the conclusion.

C.2 Vector Decomposition

A normal and friction force is applied to the prism as shown in Figure 4.1. Beginning with the normal force, decomposition yields two components as a function of β. These two components are in the same plane as the angle, β.

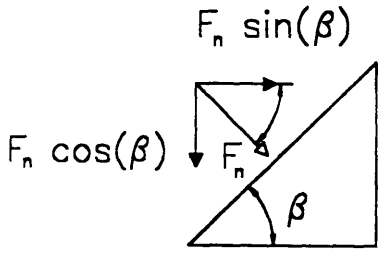

The horizontal component requires further decomposition, one vector in the longitudinal direction, another in the transverse direction. The force in the transverse direction is opposed by an equal and opposite force from the other half of the wedge and is neglected.

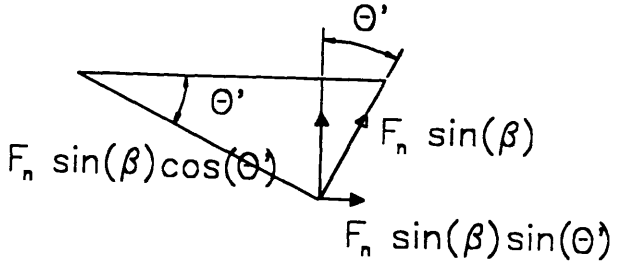

The frictional force is now decomposed into longitudinal and vertical components. This requires introduction an the angle, ζ, which describes the relative contribution of friction in a direction parallel to the base plane and one perpendicular to the edge of the wedge in the base plane. This angle is clearly defined in Figure C.1. Both of these force vectors are in the plane of the sloping face of the wedge. Projection of the force parallel to the base plane yields a longitudinal and transverse force component. Again, the transverse component may be neglected.

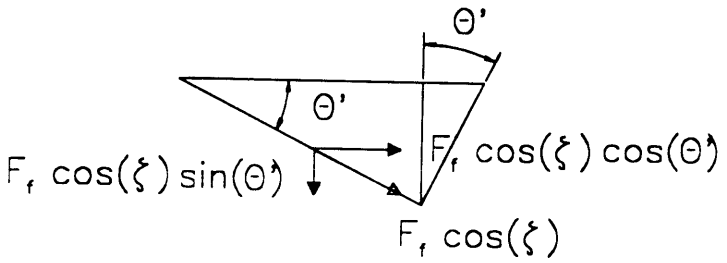

The other component of the frictional force is projected into a vertical vector and a component parallel to the base plane by use of the angle (β).

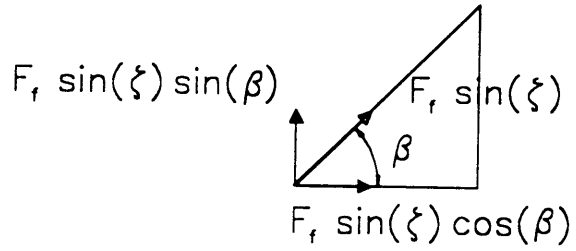

The force parallel to the base plane is decomposed into transverse and longitudinal components.

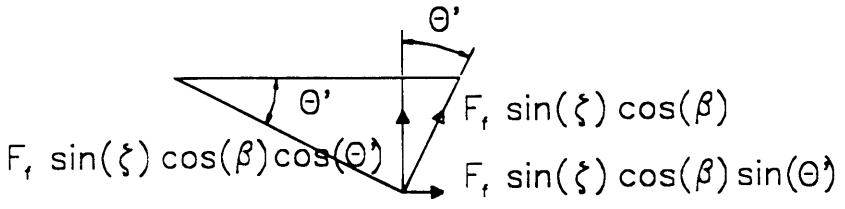

This leaves three longitudinal and two vertical components of force from the decomposition as summarized in equations (4.5) and (4.17).

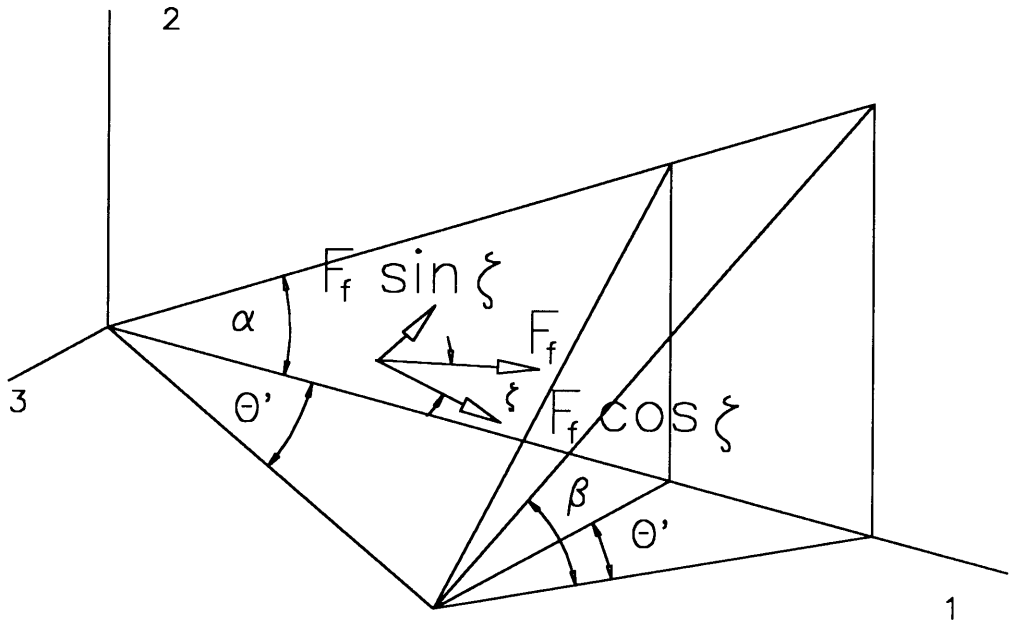

Figure C.1 Diagram of Prism Model Showing the Angle of Relative Frictional Contribution (ζ)